



**CORROSION FATIGUE CRACK GROWTH BEHAVIOR AT NOTCHED HOLE
IN 7075-T6 UNDER BIAXIAL AND UNIAXIAL FATIGUE WITH DIFFERENT
PHASES**

THESIS

Khawagi, Ali

Captain, Royal Saudi Air Force, RSAF

August 2015

**DEPARTMENT OF THE AIR FORCE
AIR UNIVERSITY**

AIR FORCE INSTITUTE OF TECHNOLOGY

Wright-Patterson Air Force Base, Ohio

DISTRIBUTION STATEMENT A

APPROVED FOR PUBLIC RELEASE; DISTRIBUTION IS UNLIMITED

AFIT-ENY-MS-15-S-065

**CORROSION FATIGUE CRACK GROWTH BEHAVIOR AT NOTCHED HOLE
IN 7075-T6 UNDER BIAXIAL AND UNIAXIAL FATIGUE WITH DIFFERENT
PHASES**

THESIS

Presented to the Faculty

Department of Aeronautics and Astronautics

Graduate School of Engineering and Management

Air Force Institute of Technology

Air University

Air Education and Training Command

In Partial Fulfillment of the Requirements for the

Degree of Master of Science in Materials Science

Khawagi, Ali
Captain, Royal Saudi Air Force, RSAF

Aug 2015

DISTRIBUTION STATEMENT A

APPROVED FOR PUBLIC RELEASE; DISTRIBUTION UNLIMITED

AFIT-ENY-MS-15-S-065

**CORROSION FATIGUE CRACK GROWTH BEHAVIOR AT NOTCHED HOLE
IN 7075-T6 UNDER BIAXIAL AND UNIAXIAL FATIGUE WITH DIFFERENT
PHASES**

Khawagi, Ali
Captain, Royal Saudi Air Force, RSAF

Approved:

Dr. Shankar Mall, PhD (Chair)

Date

Dr. Victor Perel, PhD (Member)

Date

Dr. Heath Misak, PhD (Member)

Date

Abstract

This research investigates fatigue crack propagation behavior in both air and saltwater (3.5% NaCl) environments from pre-cracked notched circular hole in a 7075-T6 cruciform specimen. With stress ratio of 0.5, biaxility stress ratio of unity, and frequency of applied load of 10 Hz, the crack growth behavior was investigated under in-plane biaxial tension-tension fatigue with 45°, 90° and 180° phase difference conditions and then compared to previous fatigue tests with no phase difference to study the effect of changing the phase differences between the applied loads on the crack growth rate. Finite Element Analysis (FEA) was used to calculate cyclic variation of stress intensity factors (ΔK) at the crack tips. The crack growth rate was observed using optical microscopy. This study shows that in the biaxial fatigue tests with phase difference of 45°, 90° and 180°, two fatigue cracks were shaped, symmetrical in case of 90° and 180°, while it's unsymmetrical for 45° phase difference case. For each phase difference and at a given average crack growth rate, the strain energy release rate of the non-split crack is equivalent to the sum of strain energy release rates of the two split cracks. In the saltwater environment, the corrosion accelerates the crack growth rate.

Acknowledgments

First, I would like to thank my advisor, Dr. Shankar Mall, for giving me the opportunity to work on this project. I appreciate his technical insights, guidance, and dedication to his students.

Also, I would like to thank Dr. Victor Perel for taking the time to show me how to properly prepare specimens and execute corrosion fatigue experiments, and his help in developing the finite element models by using Abaqus program.

I would like to thank my parents for their love and prayers for me, and most importantly, I would like to thank my wife Fawzyah for her support, encouragement, quiet patience. Her unwavering love that was undeniably the foundation upon which the past ten years of my life has been built. Her tolerance of my occasional bad moods is a testament in itself of her unbending loyalty and loves.

Khawagi, Ali

Table of Contents

	Page
Abstract	iv
Acknowledgments	v
List of Tables	xix
List of Symbols	xx
I. Introduction	1
1.1 Corrosion	1
1.2 Corrosion Fatigue	3
1.3 Biaxial Corrosion Fatigue	4
1.4 Problem Statement	5
II. Background	8
2.1 Fatigue	8
2.2 Corrosion Fatigue	9
2.3 Effect of Corrosion on Fatigue Life	11
2.4 Fracture Mechanics	13
2.4.1 Stress Intensity Factors for a Crack Originating From a Circular Hole in Thin Plate under Biaxial Loading	15
2.4.2 Stress Transformation Formulas In Case Of Plane Stress	17
2.4.3 Global and Local Coordinate Systems	19
2.4.4 Direction of Crack Propagation	23
2.5 Previous Research	26
2.6 Why This Thesis?	31
III. Methodology	32
3.1 Material	32

3.2 Test Specimens	34
3.3 Test Procedures	36
3.4 Finite Element Modeling.....	37
IV. Results and Discussion	40
4.1 Overview	40
4.2 Crack Path	41
4.2.1 Crack Path of Uniaxial and Biaxial Specimens without Phase Difference in Air and Saltwater Environments.....	41
4.2.2 Crack Path of Biaxial Specimens with Phase Differences.....	43
4.2.2.1 Crack Path of Biaxial Specimens with 45° Phase Difference in Air and Saltwater Environments	43
4.2.2.1 Crack Path of Biaxial Specimens with 90° Phase Difference in Air and Saltwater Environments	53
4.2.2.1 Crack Path of Biaxial Specimens with 180° Phase Difference in Air and Saltwater Environments	57
4.3 Crack Growth Rate	62
4.3.1 Crack Growth Rate of Uniaxial and Biaxial Specimens without Phase Difference in Air and Saltwater Environments.....	63
4.3.2 Crack Growth Rate of Biaxial Specimens with 45° Phase Difference in Air and Saltwater Environments.....	65
4.3.3 Crack Growth Rate of Biaxial Specimens with 90° Phase Difference in Air and Saltwater Environments.....	70
4.3.2 Crack Growth Rate of Biaxial Specimens with 180° Phase Difference in Air and Saltwater Environments.....	73
4.3.2 Crack Growth Rate of All Specimens with and without Phase Difference in Air and Saltwater Environments.....	76
V. Conclusions and Recommendations	81
5.1 Conclusions	81

5.2 Recommendations	84
Appendix A: Finite Element Approach (FEA)	85
Appendix B: Pictures of the Cracks at Different Biaxility ratio, Conditions and Environments.	94
Appendix C: Matlab Codes which were used to calculate the Directions of the Angles at the Bifurcations.	105
Appendix D: Sum of Crack Growth Rates versus Sum of Strain Energy Release Rate..	140
Bibliography	143

List of Figures

Figure	Page
Figure 1.1: Cost of Corrosion in Different Categories of Industry [2].....	2
Figure 2.1: Intrusion and Extrusion of Fatigue Crack Initiation [32].....	9
Figure 2.2: An Overview of the Mechanism of Corrosion Fatigue Due To Hydrogen Embrittlement [5].....	10
Figure 2.3: The Effect of Environment on the Fatigue Limit of a Material [45].	12
Figure 2.4: The Three Modes of Loading That a Crack Can Experience [5].....	14
Figure 2.5: A Crack Initiated From A Circular Hole While Subjected To Biaxial Remote Stresses.	16
Figure 2.6: Rotation of coordinate axes x_1 and x_2 about axis x_3 through angle φ	18
Figure 2.7: Remote And Local Stresses In Global And Polar Coordinate Systems, Respectively.....	21
Figure 2.8: Propagation of The Crack when $\varphi = 45^\circ$, and $\lambda' = 1$	22
Figure 3.1: The Biaxial Experimental Setup with a Cruciform Specimen.....	35
Figure 3.2: The Uniaxial Experimental Setup with a Test Specimen.	35
Figure 3.3: The Cruciform Specimen With Saltwater Chamber Installed To It.	37
Figure 4.1: The crack path of an AA 7075-T6 uniaxial specimen tested under cyclic load in air and saltwater environments.	41
Figure 4.2: The crack path of an AA 7075-T6 biaxial specimen tested under cyclic load in air environment. [28]	42

Figure 4.3: The direction of the initial crack path of an AA 7075-T6 biaxial specimen with no phase difference tested under cyclic load in air environment using analytical, finite element and experimental methods.....	43
Figure 4.4.a: The applied loads in the Y-Direction and X-Directions versus the Time, when the loads in Y-direction applied, and after one-eighth of a cycle the loads in the X-direction start to be applied, which makes a phase difference of 45°	44
Figure 4.4.b: The Direction of the Two Cracks Of an AA 7075-T6 Biaxial Specimen, with applying the loads in the Y-direction, first, and after phase difference between the applied loads of 45° , the loads in the X-direction start to be applied, Tested Under Cyclic Load in Air Environment.	45
Figure 4.4.c: The direction of the two cracks of an AA 7075-T6 biaxial specimen, with applying the loads in the Y-direction and after one-eighth of a cycle, the loads in the X-direction start to be applied, which makes a phase difference of 45° , tested under cyclic load in air environment (closer picture).	46
Figure 4.5.a: The applied loads of the Y-Direction and X-Directions versus the Time, when applying the loads in the X-direction and after one-eighth of a cycle, the loads in the Y-direction start to be applied, which makes a phase difference of 45°	47
Figure 4.5.b: The direction of the two cracks of an AA 7075-T6 biaxial specimen, when applying the loads in the X-direction and after one-eighth of a cycle, the other load applied, which makes a phase difference of 45° , tested under cyclic load in air environment.	47
Figure 4.5.c: The direction of the two cracks of an AA 7075-T6 biaxial specimen, when applying the loads in the X-direction and after one-eighth of a cycle, the other load	

applied, which makes a phase difference of 45° , tested under cyclic load in air environment. (Closer Picture).....	48
Figure 4.6: The direction of the initial crack path of an AA 7075-T6 biaxial specimen before the crack split with phase difference= 45° , tested under cyclic load in air environment using analytical and finite element methods.....	50
Figure 4.7: Variation of the horizontal (a) and vertical (b) cracks propagation, after bifurcation exists, under biaxial fatigue during one cycle with PD= 45°	51
Figure 4.8: Strain energy release rate versus number of cycles when the phase difference is 45° in air and saltwater environments.....	52
Figure 4.9.a: The applied loads of the Y-Direction and X-Directions versus the Time, when applying the loads in the Y-direction, and after one-fourth of a cycle the other load applied which makes a phase difference of 90°	53
Figure 4.9.b: The direction of the crack path of an AA 7075-T6 biaxial specimen with PD= 90° tested under cyclic load in air environment.	54
Figure 4.10: The direction of the initial crack path of an AA 7075-T6 biaxial specimen with phase difference= 90° tested under cyclic load in air environment using analytical and finite element methods.	55
Figure 4.11: Variation of the right or vertical crack propagation angle, after bifurcation exists, under biaxial fatigue during one cycle with PD= 90°	56
Figure 4.12: Strain energy release rate versus number of cycles when the phase difference is 90° in air and saltwater environments.....	57

Figure 4.13.a: The applied loads of the Y-Direction and X-Directions versus the Time, when applying the loads in the Y-direction, and after one-half of a cycle the other loads start to be applied, which makes a phase difference of 180°	58
Figure 4.13.b: The direction of the crack path of an AA 7075-T6 biaxial specimen with PD= 180° tested under cyclic load in air environment.	59
Figure 4.14: The direction of the initial crack path of an AA 7075-T6 biaxial specimen with phase difference= 180° tested under cyclic load in air environment using analytical and finite element methods.	60
Figure 4.15: Variation of the right or vertical crack propagation angle, after bifurcation exists, under biaxial fatigue during one cycle with PD= 180°	61
Figure 4.16: Strain energy release rate versus number of cycles when the phase difference is 180° in air and saltwater environments.....	62
Figure 4.17 Crack growth rate versus strain energy release rate for uniaxial and biaxial with PD= 0° specimens in air and saltwater environments.....	64
Figure 4.18: Crack length versus number of cycles for biaxial specimen with PD= 45° in air and saltwater when the Y-direction loads applied, and after one-eighth of a cycle the other loads applied, which makes a phase difference of 45°	66
Figure 4.19: Crack length versus number of cycles for biaxial specimen with PD= 45° in air and saltwater when the X-direction loads applied, and after one-eighth of a cycle the other loads applied, which makes a phase difference of 45°	67
Figure 4.20: The relationships between crack growth rate (da/dN) and strain energy release rate (ΔG) for both crack branches when the Y-direction loads applied, and	

after one-eighth of a cycle the other loads applied, which makes a phase difference of 45°, in both air and saltwater environments.	68
Figure 4.21: The relationships between the average crack growths rate (Avg. (da/dN)) and the sum of the strain energy release rate (Sum of (ΔG)) for both horizontal and vertical cracks when the phase difference is 45° in air and saltwater environments.	70
Figure 4.22: Crack length versus number of cycles for biaxial specimen with PD=90° in air and saltwater.	71
Figure 4.23: The relationships between crack growth rate (da/dN) and strain energy release rate (ΔG) for both crack branches when the Y-direction loads applied, and after phase difference between the applied loads of 90°, the loads in the X-direction start to be applied, in both air and saltwater environments.	72
Figure 4.24: The relationships between the average crack growths rate (da/dN) and the sum of the strain energy release rate (ΔG) for both horizontal and vertical cracks when the phase difference is 90° in air and saltwater environments.	73
Figure 4.25: Crack length versus number of cycles for biaxial specimen with PD=180° in air and saltwater.	74
Figure 4.26: The relationships between crack growth rate (da/dN) and strain energy release rate (ΔG) for both crack branches when the Y-direction loads applied, and after one-half of a cycle the other loads applied, in both air and saltwater environments.	75

Figure 4.27: The relationships between the average crack growths rate (da/dN) and the sum of the strain energy release rate (ΔG) for both horizontal and vertical cracks when the phase difference is 180° in air and saltwater environments.	76
Figure 4.28: The crack growth rates versus the strain energy release rate for horizontal and vertical cracks (in case of split) and the crack (in case of no split) for all cases in air environment.	78
Figure 4.29: The crack growth rates versus the strain energy release rate for horizontal and vertical cracks (in case of split) and the crack (in case of no split) for all cases in saltwater environment.	79
Figure 4.30: Average of the crack growth rates (in case of two cracks) and the crack growth rates (in case of one crack) versus the sum of the strain energy release rate (in case of two cracks) and the strain energy release rate (in case of one crack) for all cases in air and saltwater environments.	80
Figure A.1: Sketch of the Whole Specimen in Abaqus Program.	85
Figure A.2: Sketch of the Hole, Notch, Precrack and the Two Cracks in one of the Specimens in Abaqus Program.	85
Figure A.3: The Whole Part of the Specimen in Abaqus Program Including the Cracks.	86
Figure A.4: A Closer Look to the Hole, Notch, Precrack and the Two Cracks in one of the Specimens in Abaqus Program.	86
Figure A.5: Assigning the Material Type which is Aluminum Alloy 7075-T6 to the Specimen.	87

Figure A.6: Creating the Step or in Other Words How Many Cycles of Loads Need to Be There in Order to Find the ΔK s, ΔG s and the Cracks' Directions.	87
Figure A.7: Specifying the Needed Calculated Output Which are the ΔK s, ΔG s and the Cracks' Directions.	88
Figure A.8: Specifying the Location and the Direction Horizontal Crack-tip.	88
Figure A.9: Specifying the Location and the Direction Vertical Crack-tip.	89
Figure A.10: Setting the Boundary Conditions to the Cracks (No Friction between the Adjacent Surfaces of a Certain Crack), Also Choosing the Masters' and the Slaves' edges.	89
Figure A.11: Specifying the Dynamic Loads to the Horizontal End Arms of the Specimen.....	90
Figure A.12: Specifying the Dynamic Loads to the Vertical End Arms of the Specimen.	90
Figure A.13: Creating an Area that Need to Have Concentrated Mesh Later in Order to Get an Accurate Calculated Results.....	91
Figure A.14: Meshing the Whole Specimen including the Concentrated Area.	91
Figure A.15: A Closer Look to the the Concentrated Area Mesh.	92
Figure A.16: Creating a Jop to be Submitted Later.....	92
Figure A.17: One of the Results after finishing the Calculations.....	93
Figure B.1: Crack Shape with 45° of Phase Difference at the Beginning of Cycles in Air Environment When X-matrix Shifted.....	94
Figure B.2: Cracks Shape with 45° of Phase Difference at the 60,000 Cycles in Air Environment When X-matrix Shifted.....	94

Figure B.3: Crack Shape with 45° of Phase Difference at 1,139,198 Cycles in Air	
Environment When X-matrix Shifted.....	95
Figure B.4: Crack Shape with 45° of Phase Difference at the Beginning of Cycles in Air	
Environment When Y-matrix Shifted.....	95
Figure B.5: Crack Shape with 45° of Phase Difference at 52,000 Cycles in Air	
Environment When Y-matrix Shifted.....	96
Figure B.6: Crack Shape with 45° of Phase Difference at 95,000 Cycles in Air	
Environment When Y-matrix Shifted.....	96
Figure B.7: Crack Shape with 45° of Phase Difference at the Beginning of Cycles in	
Saltwater Environment When X-matrix Shifted.....	97
Figure B.8: Crack Shape with 45° of Phase Difference at 135,300 Cycles in Saltwater	
Environment When X-matrix Shifted.....	98
Figure B.9: Crack Shape with 45° of Phase Difference at 305,300 Cycles in Saltwater	
Environment When X-matrix Shifted.....	98
Figure B.10: Crack Shape with 90° of Phase Difference at the Beginning of Cycles in	
Air Environment When X-matrix Shifted.	99
Figure B.11: Crack Shape with 90° of Phase Difference at 170,000 Cycles in Air	
Environment When X-matrix Shifted.....	99
Figure B.12: Crack Shape with 90° of Phase Difference at 270,000 Cycles in Air	
Environment When X-matrix Shifted.....	100
Figure B.13: Crack Shape with 90° of Phase Difference at the Beginning of Cycles in	
Saltwater Environment When X-matrix Shifted.....	100

Figure B.14: Crack Shape with 90° of Phase Difference at 145,000 Cycles in Saltwater Environment When X-matrix Shifted.....	101
Figure B.15: Crack Shape with 90° of Phase Difference at 174,500 Cycles in Air Environment When X-matrix Shifted.....	101
Figure B.16: Crack Shape with 180° of Phase Difference at the beginning of Cycles in Air Environment When X-matrix Shifted.	102
Figure B.17: Crack Shape with 180° of Phase Difference at 80,000 Cycles in Air Environment When X-matrix Shifted.....	102
Figure B.18: Crack Shape with 180° of Phase Difference at 110,000 Cycles in Air Environment When X-matrix Shifted.....	103
Figure B.19: Crack Shape with 180° of Phase Difference at the beginning of Cycles in Saltwater Environment When X-matrix Shifted.....	103
Figure B.20: Crack Shape with 180° of Phase Difference at 10,000 Cycles in Saltwater Environment When X-matrix Shifted.....	104
Figure B.21: Crack Shape with 180° of Phase Difference at 26,000 Cycles in Saltwater Environment When X-matrix Shifted.....	104
Figure C.1: Matlab Code for Calculating the Direction of the Initial Crack Propagation in Case of Biaxial Fatigue test with $PD=45^\circ$	108
Figure C.2: Matlab Code for Calculating the Direction of the Initial Crack Propagation in Case of Biaxial Fatigue test with $PD=90^\circ$	113
Figure C.3: Matlab Code for Calculating the Direction of the Initial Crack Propagation in Case of Biaxial Fatigue test with $PD=180^\circ$	122

Figure C.4: Matlab Code for Calculating the Direction of the Horizontal Crack that split from the precrack in Case of Biaxial Fatigue test with PD=45°	126
Figure C.5: Matlab Code for Calculating the Direction of the Vertical Crack that split from the precrack in Case of Biaxial Fatigue test with PD=45°	128
Figure C.6: Matlab Code for Calculating the Direction of one of the symmetric Cracks that split from the precrack in Case of Biaxial Fatigue test with PD=90°	136
Figure C.7: Matlab Code for Calculating the Direction of one of the symmetric Cracks that split from the precrack in Case of Biaxial Fatigue test with PD=180.	139
Figure D.1: Sum of crack growth rates versus sum of strain energy release rate for all cases in air environment.	140
Figure D.2: Sum of crack growth rates versus sum of strain energy release rate for all cases in salt environment.	141
Figure D.3: Sum of crack growth rates versus sum of strain energy release rate for all cases in air and salt environments.....	142

List of Tables

Table	Page
Table 3.1: Chemical compositions of AA7075-T6 alloy [3].....	32
Table 3.2: Mechanical properties of AA 7075-T6 [3].....	33
Table 4.1: Summary Of The Biaxial Tests Under Fatigue Loads With 0^0 , 45^0 , 90^0 And 180^0 Phase Differences in Air and Saltwater Environments.	40

List of Symbols

Symbol	Definition
Δ	change in a variable (unit less)
a	crack length (mm)
α	angle between the y-axis and the crack (degree)
φ	angle between the x-axis and the crack ($\varphi = \frac{\pi}{2} - \alpha$) (degree)
b	width of specimen (mm)
C	constant for Paris law (unit less)
CF	corrosion fatigue
da/dN	rate of crack growth per cycle (m/cycle)
DOD	Department of Defense
\hat{e}	unit basis vectors of the original coordinate system
\hat{e}'	unit basis vectors of the rotated coordinate system
F_x	applied force in the x-direction (N)
F_y	applied force in the y-direction (N)
G	strain energy release rate
HC	horizontal crack
I	mode one (opening)
K	stress intensity factor (MPa*m ^{0.5})
q	mapping the components of a vector onto the components of the same vector in a second coordinate system

R	stress ratio for cyclic loading (unit less)
r	radius of the circular hole (m)
$S_{xx}=S_x$	remote normal stresses at a long distance from the crack tip in the x-direction with respect to the global coordinate system (xy plane) (N/m^2)
$S_{yy}=S_y$	remote normal stresses at a long distance from the crack tip in the y-direction with respect to the global coordinate system (xy plane) (N/m^2)
S_{xy}	remote shear stresses at a long distance from the crack tip with respect to the global coordinate system (xy plane) (N/m^2)
S'_{xx}	remote normal stresses at a long distance from the crack tip in the x-direction with respect to the local rectangular coordinate system ($x'y'$ plane) (N/m^2)
S'_{yy}	remote normal stresses at a long distance from the crack tip in the y-direction with respect to the local rectangular coordinate system ($x'y'$ plane) (N/m^2)
S'_{xy}	remote shear stresses at a long distance from the crack tip with respect to the local rectangular coordinate system ($x'y'$ plane) (N/m^2)
$S_{\rho\rho}$	remote normal stresses at a long distance from the crack tip at angle of θ with respect to the local polar coordinate system ($\rho\theta$ plane) (N/m^2)
$S_{\theta\theta}$	remote normal stresses at a long distance from the crack tip at an angle of $\theta + 90^\circ$ with respect to the local polar coordinate system ($\rho\theta$ plane) (N/m^2)
$S_{\rho\theta}$	remote shear stresses at a long distance from the crack tip with respect to the local polar coordinate system ($\rho\theta$ plane) (N/m^2)

σ'_{xx}	normal stresses near the crack tip in the x-direction with respect to the local rectangular coordinate system ($x'y'$ plane) (N/m^2)
σ'_{yy}	normal stresses near the crack tip in the y-direction with respect to the local rectangular coordinate system ($x'y'$ plane) (N/m^2)
σ'_{xy}	shear stresses near the crack tip in with respect to the local rectangular coordinate system ($x'y'$ plane) (N/m^2)
$\sigma_{\rho\rho}$	normal stresses near the crack tip at an angle of θ from the local rectangular coordinate system ($x'y'$ plane) and with respect to the local polar coordinate system ($\rho\theta$ plane) (N/m^2)
$\sigma_{\theta\theta}$	normal stresses near the crack tip at an angle of $\theta + 90^\circ$ from the local rectangular coordinate system ($x'y'$ plane) and with respect to the local polar coordinate system ($\rho\theta$ plane) (N/m^2)
$\sigma_{\rho\theta}$	shear stresses near the crack tip with respect to the local polar coordinate system ($\rho\theta$ plane) (N/m^2)
T	stress tensor
T'	transformed stress tensor
t	thickness of specimen (mm)
VC	vertical crack
w	width of specimen (mm)
ω	frequency of the applied load
σ	stress (MPa)
λ	global biaxiality ratio

λ' local biaxiality ratio

CRACK INITIATION AND GROWTH NATURE AT NOTCHED HOLE IN 7075-T6 UNDER BIAXIAL AND UNIAXIAL FATIGUE WITH DIFFERENT PHASES

I. Introduction

1.1 Corrosion

One of the world's common concerns, when it comes to increasing efficiency of most metal products or decreasing their cost of operation, is corrosion. It is almost an unavoidable dilemma in nearly most of the infrastructures. Just about every United States' industrial sector, from infrastructure and transportation to production and manufacturing, suffers from the metallic corrosion, because of the major role that it plays in the efficiency, cost, and durability of every platform or system [14].

Roughly, United States loses 3.1% of its Gross National Product to the corrosion, yearly, which is nearly \$276 Billion [11, 14]. Each year, the transportation sector alone pays around \$29.7 billion for corrosion losses, and this number represents 21.5% of the total cost that United States pay for corrosion [11]. These billions show that the corrosion needs to be addressed more. Humans, ecosystem or environment surrounding these structures are being damaged from this phenomenon. Corrosion on infrastructure can be witnessed through physical effects or even from flaws that can cause unanticipated failures. Figure 1.1 shows that nearly every industry has its own share of suffering from corrosion [2].

The United States Department of Defense has created a broad strategy to fight corrosion throughout its forces [15]. DODs' resources have been directed toward corrosion

prevention. Along with that, it started to look into acquisition level before manufacturing, management decisions, maintenance procedures, and sustainment to extend the life of materiel [15]. Each year, \$22.5 billion is what the United States pay for the DOD to control and prevent corrosion, while the DoD energetically searches for new corrosion solutions and prevention technologies, procedures, products, and management systems for its armed forces and infrastructure [15, 16].

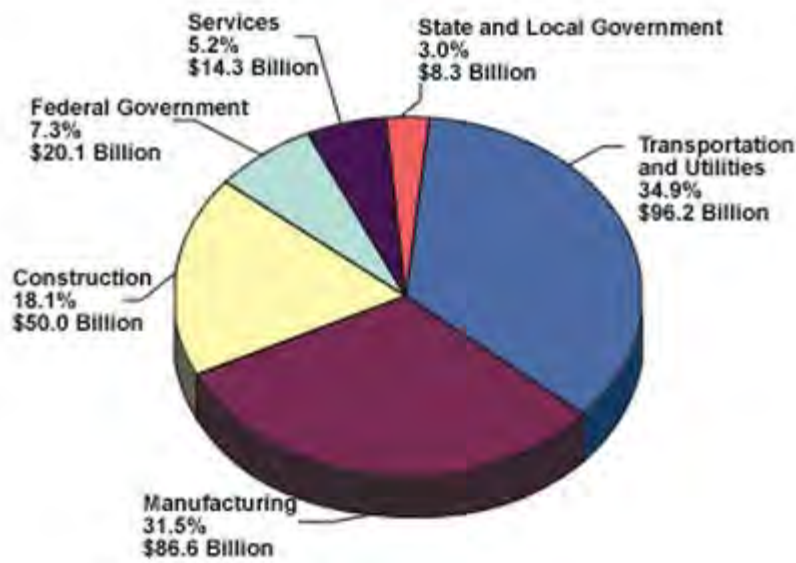


Figure 1.1: Cost of Corrosion in Different Categories of Industry [2].

The United States Air Force also has a huge impact from corrosion. The extension of the service life of the current and future fleets, along with their infrastructures can be addressed by preventing and controlling this phenomenon, which, in return reducing the cost of operations.

Corrosion can be defined as deterioration of a metallic material due to the reaction between the metal and its environment, or there must be an anode, a cathode and an electrolyte joined by an external current circuit [31]. Several methods are out there to

control the corrosion, such as painting, coatings, chemical inhibitors, materials selection, cathodic method, and this list could go on. The proper understanding of the type of corrosion is the key to choose which method is appropriate to control it [31, 35].

Aluminum alloy is the material that is being used in this study, because it is one of the most common metals that is being used in the aircraft industries, due to its light weight, ease of manufacturing, low cost, and resistance to corrosion. Nevertheless, corrosion could affect an aluminum alloy if it is subjected to acidic solutions. [25]

1.2 Corrosion Fatigue

As stated before, the corrosion is the deterioration of a metallic material chemically or electrochemically. On the other hand, fatigue is the failing of a material due to the repetitive applied load under the yield point of that material. There are several factors that contribute to fatigue failures, such as applied cyclic stresses, thermal expansions and contractions, poor assembly, welding, and casting [33]. When these different factors failure modes are combined, the failure occurs sooner. When cracks grow due to both corrosion and cyclic loading, then they say that corrosion fatigue (CF) occurs, and it leads to failure at lower number of cycles as compared to failure under cyclic loading alone [2]. Corrosion fatigue could lead to catastrophic failure if the cracks are not noticed by inspectors in time [12]

Corrosion fatigue takes place when a metal fails at stresses much lower than its tensile strength, while the corrosive environment acts as an accelerator of the crack growth. Besides, the corrosive environment accelerates the crack initiation.

1.3 Biaxial Corrosion Fatigue

Replacing the aircraft's components, failed due to corrosion fatigue, is only one way to answer the question of how to increase the lifetime of the aircraft. Another way to address these failures and to reduce the cost of operations is to understand how these structural materials fail in the first place. Then, by preventing or at least delaying the cause of those failures, the performance of the materials will be enhanced.

During the operation of an aircraft, its structures experience different types of loads and moments in different directions. If the structures experience these loads and moments in a corrosive environment, the initiation and the propagation of cracks will be accelerated, which could result in corrosion fatigue failure. Accordingly, crack initiation and propagation in a corrosive environment is one of the most important topics that need to be addressed and understood in order to prevent the failures associated with it. A very important approach that has been used a lot to examine the propagation of cracks is the damage tolerance approach. This approach is used to study the crack propagation, and follows the assumption that flaws are present in all structures and propagate due to cyclic loading and corrosion. Through the application of the principles of fracture mechanics, this approach is universally used in aerospace engineering to manage the extension of cracks in structure [26].

Researchers have already started studying crack propagation and the affect of environments on the crack growth behavior [26]. At present, a lot of information has been documented from those studies, but most of the studies had been done under uniaxial loading [5, 9, 26]. Nearly all aircraft structures are subjected to mixed mode of stresses, which can limit the benefits gained from the data of the uniaxial fatigue tests.

In-plane biaxial loading is one of the common loading conditions that aircraft structures experience throughout their operations. Hence, a lot of information will be gained from conducting tests in these loading states, which help understanding crack growth rate [26]. There are few studies that had been done in this field and, until lately, nearly all of those studies are done in air environment [27]. For example, by using a cruciform specimen of an aluminum alloy, crack growth behavior had been examined under in-plane biaxial loading and with different biaxial stress ratios [23, 26]. Also, Lee and Taylor have investigated the effects of in-plane stress biaxility on the fatigue life [22]. In addition, earlier studies have shown that biaxial loading has an influence on fatigue crack growth rates [18, 27].

Corrosion fatigue crack growth for aluminum alloys and in corrosive (saltwater) environment has been investigated deeply under uniaxial loading conditions, but none of those studies tried to conduct a test under biaxial loading conditions in a corrosive environment [26]. Under saltwater environment, several studies of an in-plane biaxial fatigue crack growth of aluminum alloy had been conducted to give a better understanding of crack growth rate generated from rivet holes or bolted joints in saltwater environment [27].

1.4 Problem Statement

Fatigue crack growth in specimens around holes should be examined, due to the fact that nearly 70% of fatigue cracks begin growing from rivet holes or bolted joints [22]. Usually, material fatigue data are gained and analyzed from uniaxial stress tests in both air and corrosive environments, but because aircraft structures experience mixed mode of

stresses during their operations, researchers started experimenting with crack growth behavior under an in-plane biaxial fatigue condition in air environment, which is one of the common conditions of mixed mode of stresses [12, 26, 27]. In addition to that, lately, in-plane biaxial fatigue tests in saltwater environment have been started to be conducted [26, 27]. Those tests have been carried out with 0.5 stress ratio, 10 Hz frequency and with different biaxility ratios [26, 27, 28]. None of these tests considered changing the phase difference between the applied fatigue loads and studied the effect of that on crack growth rate, which is the focus of this research, using fracture mechanics approach.

To achieve the objective of this study, the fatigue crack growth behavior of specimen made of 7075-T6 aluminum alloy, which is a broadly used material in aircraft structures [27], was examined under in-plane biaxial loading in both ambient air and saltwater (3.5% NaCl) environments with 45°, 90° and 180° phase difference conditions. After that, the results have been compared to in-phase tests having the same experimental setup, to study the effect of changing the phase difference on crack growth rate, which is what has been lacking in this field up to now. In addition, comparisons of fatigue crack growth behavior have been done with specimens made of the same alloy but under uniaxial fatigue condition, in both ambient air and saltwater environments.

To prepare specimens for biaxial loading tests, cruciform specimens, machined from a 3.18 mm thick sheet of 7075-T6 aluminum alloy, were used. These specimens have stress ratio of 0.5 ($R = 0.5$), and biaxiality ratio of 1 ($\lambda = 1$). Length of the specimen's arm was 120 mm, and width was 45 mm. The radius of curvature at the junction of arms was 45 mm. At the center of the specimen, a 6 mm diameter hole was drilled. Then, a notch, from the edge of the hole, with 1 mm length and 0.25 mm width was machined at 45° to

horizontal and vertical arm. Finally, a precrack was made from the notch. Similar specimens were used for the in-phase biaxial loading tests.

Besides, in a separate study, uniaxial loading tests were conducted on rectangular 7075-T6 aluminum alloy specimens with $R = 0.5$. The specimens are 50 mm wide and 3.18 mm thick. After that, a circular hole of 6 mm diameter was drilled at the center of the specimens. A notch at the edge of the hole was created and then pre-cracked [28]. The results of the biaxial tests were compared to the results of the uniaxial tests in order to study the behavior of the cracks.

The crack growth rate has been measured with the number of cycles to failure. Then, finite element analysis of crack growth for both biaxial and uniaxial loading conditions was carried out to calculate the range of stress intensity factor, ΔK and the strain energy release rate, G . Then, G was linked with the crack growth rate in order to study the behavior of the cracks.

This research provided a great deal of valuable and usable information for fatigue crack growth behavior from a notched hole. It provided a practical data to compare different loading conditions, biaxial and uniaxial loading, in different environments, to better calculate the lifespan of an aging fleet of aircrafts. Also, this study will help to fill the missing part from the previous studies in this field.

II. Background

2.1 Fatigue

Numbers of military aircraft, commercial aircraft, and unmanned aerial vehicles increase with time. So, the need for understanding and improving the Structural integrity analysis of aging aircraft increased too. Since fracture mechanics has come to life, it has been used, along with strength of materials, to push aircraft structures to their limits. As known, cracks initially are assumed to be present in each aircraft structural component. Those cracks are also known to be growing with the aging of the aircraft (fatigue) [1].

The notion of fatigue arose several times when it came to structural integrity. In the Comet aircraft, for instance, the crack growth led to disaster when that crack became large enough to propagate in unstable manner as expected according to the Griffith theory [36]. Fatigue is a stable growth of cracks because of cycling of loads, if the stresses are below the yield point of the material [5, 34]. Several forms of stresses can lead to fatigue failure, such as bending, torsion, and rotation [36].

For metals, generally, fatigue phenomena start at an inner or surface flaw at locations where there are concentrated stresses. First, shear flow along slip planes will occur, and after a certain number of cycles, intrusions and extrusions will be generated from that slip, which leave small steps in the surface. These small steps yield to increase stress in that region and in return infinitesimal cracks (microcracks) initiate [32, 33, 36]. Microcracks come along planes of high shear stress, which is 45° to the load direction. This first stage end here, while the second stage takes over when these tiny voids connect together and propagate through the structure, creating an angle 90° to the load direction,

see Figure 2.1[32]. When the fracture toughness is exceeded, and the fracture occurs, then this is the third stage of fatigue failure [32].

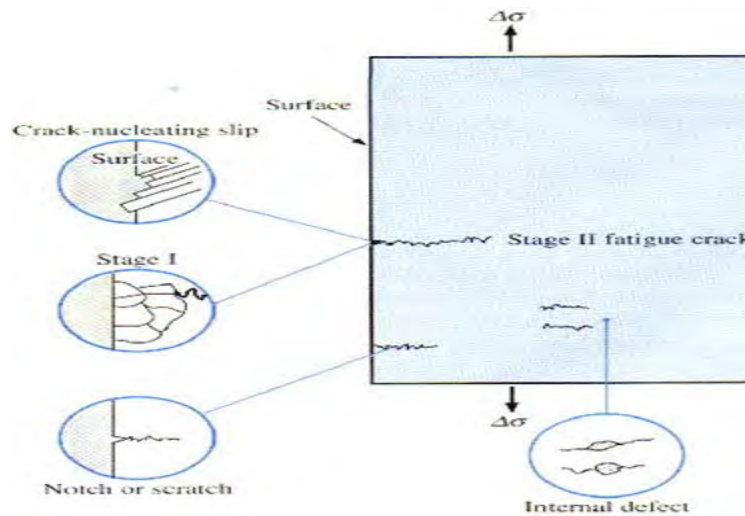


Figure 2.1: Intrusion and Extrusion of Fatigue Crack Initiation [32].

2.2 Corrosion Fatigue

One of the most complicated topics in the modes of failure of aircraft structures is corrosion fatigue failure in metals. Corrosion fatigue can be defined as the damage, in the presence of a corrosive environment, of a metallic structure caused by the buildup and repetitive loading cycles [12, 36]. With increasing load cycle numbers, corrosion fatigue damage builds up and this damage takes place in four stages. These stages are cyclic plastic deformation, microcracks initiation, small crack growth connects them together forming a bigger crack, and lastly macrocrack propagation [12].

Understanding the mechanism of corrosion fatigue is very important in order to help preventing this mode of failure. Film rupture and hydrogen embrittlement are the two mechanisms that explain the corrosion fatigue behavior [5]. The 7075-T6 aluminum alloy is the material that is used for this study and it follows the hydrogen embrittlement

mechanism on its way to corrosion fatigue failure, which is the only mechanism that will be explained here [13]. For hydrogen embrittlement mechanism, the crack growth starts when there is a notch, or flaw, that goes through the protective coating of the material, if there is any, and the surface. When the latter happens, the material is more likely to corrode since it is in contact with the environment. This void often results in the creation of hydrogen ions at the surface of the material, which weaken the metallic binding forces. This hydrogen can pass through to similar flaws and enter into the lattice structure of the material resulting in embrittlement. Hydrogen embrittlement results in a material that is more brittle and more expected to initiate transgranular cracks, which are cracks that propagate through the grains of the material, because of repeated loads. Figure 2.2 provides an overview of the mechanism of corrosion fatigue [5]. As stated, understanding the mechanisms of corrosion fatigue is essential to interpret the lab results. [12, 13]

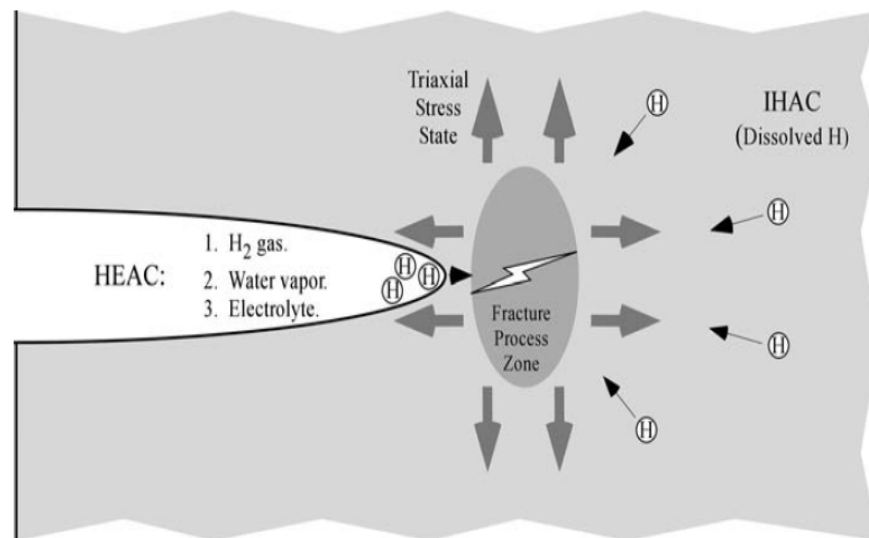


Figure 2.2: An Overview of the Mechanism of Corrosion Fatigue Due To Hydrogen Embrittlement [5].

Just for clarification, corrosion fatigue (CF) and Stress corrosion cracking (SCC) are very similar in several features, such as the mechanism of crack formation and fracture because of embrittlement. On the other hand, the two concepts differ in the type of loading, which is static in SCC and fluctuating in CF. Also, they differ in the crack surface appearance, which is cleavage-like in SCC and beach marks and/or striations in case of CF. Moreover, they differ in the crack morphology, which is branched in SCC, while CF has blunt tip characteristic. [46]

2.3 Effect of Corrosion on Fatigue Life

When a corrosive environment is combined cyclic loading, the resultant damaging effect is higher than the sum of damaging effects of corrosion and cyclic loading, applied separately. This can be called Synergistic damage [45]. The creation of intrusion and extrusion due to fatigue loading results in the formation of notches. Then, when the corrosion gets in contact with the notches, it causes oxidization to the base metal. After that, the material becomes inactive to further corrosion damage. However, the fatigue process will disturb the passive layer and help the corrosive environment to corrode the new visible material. For this reason, the fatigue life of that material will be severely minimized. [45]

There are two concepts that are very common when discussing fatigue. First concept is the fatigue life, which is the number of cycles of a component to failure. The second one is the fatigue limit, which can be defined as the maximum value of varying stress, which a structural material can survive with no failure [20]. Both of these values are reduced in the

presence of corrosive environment [20]. Corrosion affects negatively the fatigue life of a structural component, and this can be expressed by the Damage ratio:

$$\text{Damage Ratio} = \frac{\sigma_{cf}}{\sigma_f} \quad (2.1)$$

where σ_{cf} the corrosion is fatigue strength, and σ_f is the fatigue strength in air environment. [20]

Low values of maximum stress and short time to failure can be noticed if a material is subjected to corrosion fatigue. Figure 2.3 shows the effect of a corrosive environment on both the fatigue limit of a material and the number of cycles to failure.

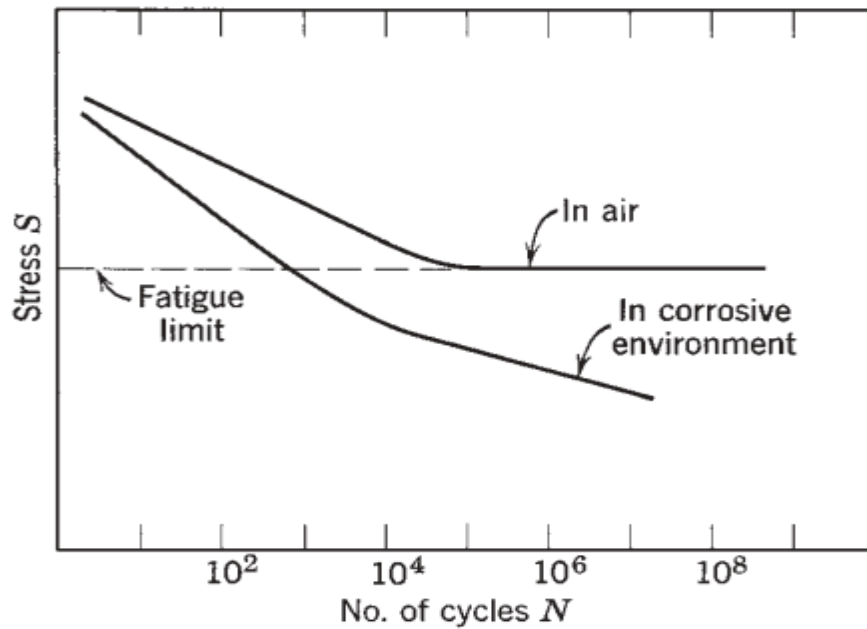


Figure 2.3: The Effect of Environment on the Fatigue Limit of a Material [45].

There are several techniques to prevent a structural material from corrosion fatigue. These techniques involve designing and constructing the materials properly. Inducing

compressive residual stresses in structural component could be helpful to prevent corrosion fatigue, using Shot Peening (SP), Laser peening (LP), or Low Plasticity Burnishing (LPB) [37]. Avoiding notches, dents and rough surface also can be very significant in the prevention of the corrosion fatigue. There are other methods, such as avoiding unnecessary cycling loading, removing environmental factors that could cause corrosion, and applying corrosion protection coatings [20].

2.4 Fracture Mechanics

Fracture mechanics can studies the propagation of cracks in materials, and is used to improve the mechanical performance of structural components [36]. It employs stress and strain analysis of both elastic and plastic materials with flaws and cracks to predict the macroscopic failure [5]. To further understand the cause of failure, a science, which studies the fracture surfaces of materials, known as fractography, is used [30]. The prediction of crack growth behavior is at the core of fracture mechanics. There are three types of loading, which a crack can experience, see Figure 2.4 [5]:

- Mode I (Opening mode): This is a tensile stress that acts normal to the plane of the crack.
- Mode II (Sliding mode): This is a shearing stress that acts parallel to the plane of the crack and perpendicular to the crack front), and
- Mode III (Tearing mode): This is a shearing stress that act parallel to the plane of the crack and parallel to the crack front. [5]

A crack can experience either one of these modes or even a mixture of them [5]. However, this study will deal only with mode I and mode II loadings, due to the fact that the specimens, used in the experiments, experienced only in-plane biaxial tension - tension fatigue.

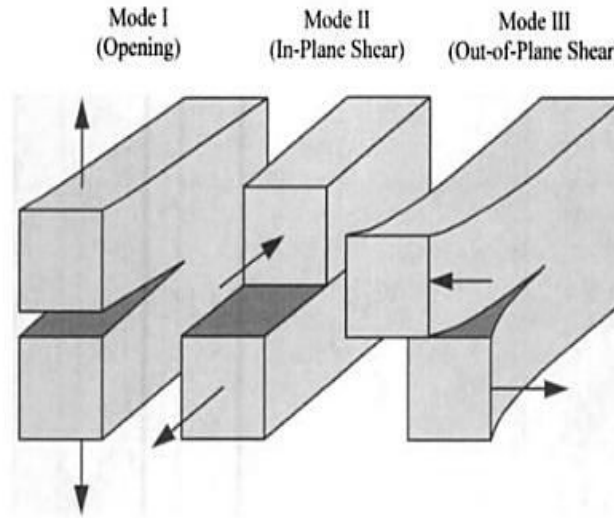


Figure 2.4: The Three Modes of Loading That a Crack Can Experience [5].

In this study, the cracks propagated from a circular hole in thin cruciform specimen under biaxial loading, after being notched and then precracked. Thus, to better understand the propagation of crack, originating from a circular hole, and also to understand the direction of the propagation, the following sections will provide a literature review on the stress intensity factors for crack initiated from a circular hole, stress transformation, global and local coordinate systems and direction of crack propagation, including an analytical approach to predict the direction of crack propagation.

2.4.1 Stress Intensity Factors for a Crack Originating From a Circular Hole in Thin Plate under Biaxial Loading

The stress intensity factor is a characteristic of stress state near the crack tip. [5]. If a crack is originating from a circular hole in a thin plate (plane stress condition) then, the stress intensity factors for mode I and II are given by the following expressions [19]:

$$K_I = \frac{\sqrt{\pi r}}{2\sqrt{2}} \sqrt{\frac{l_0 (l_0 + 2)^3}{(l_0 + 1)^3}} (S_{yy} + S_{xx} - (S_{yy} - S_{xx}) \cos 2\alpha) \quad (2.2)$$

and

$$K_{II} = \frac{\sqrt{\pi r}}{2\sqrt{2}} \sqrt{\frac{l_0 (l_0 + 2)^3}{(l_0 + 1)^3}} (S_{xx} - S_{yy}) \sin 2\alpha \quad (2.3)$$

where

$$l_0 = \frac{1}{2} \left(-1 + \frac{a}{r} + \sqrt{2 \frac{a}{r} + \frac{a^2}{r^2} + 1} \right) \quad (2.4)$$

where:

S_{xx} is the nominal stress at a large distance from the crack tip in the x-direction (N/m²).

S_{yy} is the nominal stress at a large distance from the crack tip in the y-direction (N/m²).

r is the radius of the circular hole (m).

a is the length of the crack (m).

α is the angle between the y-axis and the crack.

φ is the angle between the x-axis and the crack ($\varphi = \frac{\pi}{2} - \alpha$).

Figure 2.5 shows a crack initiated from a circular hole, subjected to biaxial remote stresses (S_x and S_y) with respect to the global rectangular (x and y) coordinate system.

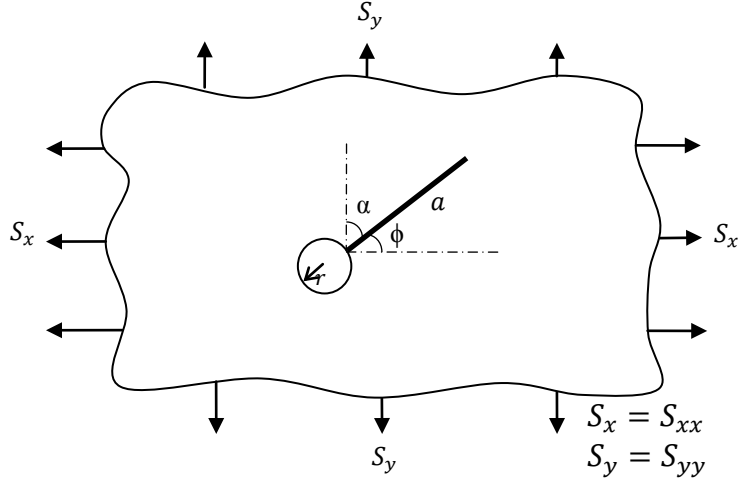


Figure 2.5: A Crack Initiated From A Circular Hole While Subjected To Biaxial Remote Stresses.

Now, when the angle ϕ between the x -axis and the crack is $\phi = \frac{\pi}{4}$ radians = 45° as in the case of this study, then equations (2.2) and (2.3) become [19]:

$$K_I = \frac{\sqrt{\pi r}}{2\sqrt{2}} \sqrt{\frac{l_0 (l_0 + 2)^3}{(l_0 + 1)^3}} (S_{yy} + S_{xx}) \quad (2.5)$$

and

$$K_{II} = \frac{\sqrt{\pi r}}{2\sqrt{2}} \sqrt{\frac{l_0 (l_0 + 2)^3}{(l_0 + 1)^3}} (S_{yy} - S_{xx}) \quad (2.6)$$

Therefore, for $\phi = 45^\circ$, the ratio of the stress intensity factors of mode II and mode I is:

$$\frac{K_{II}}{K_I} = \frac{S_{xx} - S_{yy}}{S_{xx} + S_{yy}} \quad (2.7)$$

2.4.2 Stress Transformation Formulas In Case Of Plane Stress

In this section, components of stress tensor near the crack tip (local stresses) will be denoted by σ with two subscripts, and components of the stress tensor far from the crack tip (remote stresses) will be indicated by S with also two subscripts. In this section a general transformation equations for components of the second-order tensor T_{mn} in a coordinate plane (X_1, X_2) will be considered.

If there is a state of plane stress in the coordinate plane x_1x_2 (plane xy), then upon rotation of coordinate axes about axis x_3 (axis z) through angle φ , as shown in Figure 2.6, the matrix of components of stress tensor:

$$[T] = \begin{bmatrix} T_{11} & T_{12} \\ T_{21} & T_{22} \end{bmatrix} \quad (2.8)$$

is transformed into the matrix:

$$[T'] = \begin{bmatrix} T'_{11} & T'_{12} \\ T'_{21} & T'_{22} \end{bmatrix} \quad (2.9)$$

And according to the general formula of transformation of tensor components [7], equation (2.9) can be written as:

$$[T'] = [q] [T] [q]^T \quad (2.10)$$

where

$$[q] = \begin{bmatrix} q_{11} & q_{12} \\ q_{21} & q_{22} \end{bmatrix} \quad , \quad q_{mn} = \cos(\hat{e}'_m, \hat{e}_n) \quad (2.11)$$

and \hat{e}_m or \hat{e}_n (for $n= 1, 2$ and $m=1,2$) are unit basis vectors of the original coordinate system, and \hat{e}'_m or \hat{e}'_n (for $n= 1, 2$ and $m=1,2$) are unit basis vectors of the rotated coordinate system.

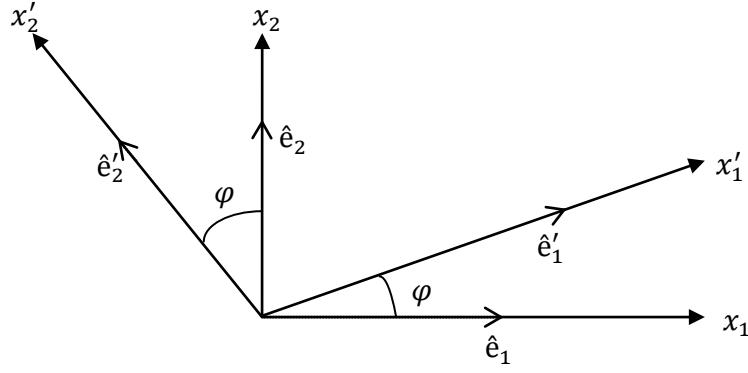


Figure 2.6: Rotation of coordinate axes x_1 and x_2 about axis x_3 through angle φ .

Now,

$$q_{11} = \cos(\hat{e}'_1, \hat{e}_1) = \cos \varphi \quad (2.12.a)$$

$$q_{12} = \cos(\hat{e}'_1, \hat{e}_2) = \sin \varphi \quad (2.12.b)$$

$$q_{21} = \cos(\hat{e}'_2, \hat{e}_1) = -\sin \varphi \quad (2.12.c)$$

$$q_{22} = \cos(\hat{e}'_2, \hat{e}_2) = \cos \varphi \quad (2.12.d)$$

So, the formula of transformation of tensor components, with account of symmetry

($T_{mn} = T_{nm}$), takes the form:

$$\begin{bmatrix} T'_{11} & T'_{12} \\ T'_{21} & T'_{22} \end{bmatrix} = \begin{bmatrix} \cos \varphi & \sin \varphi \\ -\sin \varphi & \cos \varphi \end{bmatrix} \begin{bmatrix} T_{11} & T_{12} \\ T_{12} & T_{22} \end{bmatrix} \begin{bmatrix} \cos \varphi & -\sin \varphi \\ \sin \varphi & \cos \varphi \end{bmatrix} \quad (2.13)$$

Expanding equation (2.13) yields:

$$T'_{11} = T_{11} \cos^2 \varphi + T_{22} \sin^2 \varphi + 2T_{12} \sin \varphi \cos \varphi$$

$$T'_{22} = T_{11} \sin^2 \varphi + T_{22} \cos^2 \varphi - 2T_{12} \sin \varphi \cos \varphi \quad (2.14)$$

$$T'_{12} = T'_{21} = T_{12}(\cos^2 \varphi - \sin^2 \varphi) + (T_{22} - T_{11}) \sin \varphi \cos \varphi$$

And with the use of trigonometric identities

$$\begin{aligned}
\cos^2 \varphi &= \frac{1}{2}(1 + \cos 2\varphi) \\
\sin^2 \varphi &= \frac{1}{2}(1 - \cos 2\varphi) \\
\sin \varphi \cos \varphi &= \frac{1}{2} \sin 2\varphi
\end{aligned} \tag{2.15}$$

equation (2.14) can be written as:

$$\begin{aligned}
T'_{11} &= \frac{1}{2}(T_{11} + T_{22}) + \frac{1}{2}(T_{11} - T_{22}) \cos 2\varphi + T_{12} \sin 2\varphi \\
T'_{22} &= \frac{1}{2}(T_{11} + T_{22}) - \frac{1}{2}(T_{11} - T_{22}) \cos 2\varphi - T_{12} \sin 2\varphi \\
T'_{12} &= T'_{21} = -\frac{1}{2}(T_{11} - T_{22}) \sin 2\varphi + T_{12} \cos 2\varphi
\end{aligned} \tag{2.16}$$

which are the components of the stress tensor with respect to the coordinate system x'_1 and x'_2 . These components will be used in the next section to find stresses with respect to the local polar coordinate ($\rho\theta$ plane) and a local biaxility ratio, which will be defined later.

2.4.3 Global and Local Coordinate Systems

The local polar coordinate system ($\rho\theta$) is defined as such that the angle θ is measured from the direction of the x' - axis, as shown in Figure 2.7. Axes of the global coordinate system xy are aligned with horizontal and vertical arms of the specimen (Figure 2.7). Axis x' of the local coordinate system $x'y'$ is aligned with the notch (Figure 2.7).

The components of the stress tensor far from the crack tip (remote stresses) with respect to the global coordinate system (xy plane) will be denoted as S_{xx} , S_{yy} and S_{xy} , while remote stresses with respect to the local rectangular coordinate system ($x'y'$ plane) will be

denoted as S'_{xx} , S'_{yy} and S'_{xy} . On the other hand, remote stresses with respect to the local polar coordinate system ($\rho\theta$ plane) will be denoted as $S_{\rho\rho}$, $S_{\theta\theta}$ and $S_{\rho\theta}$.

The components of stress tensor near the crack tip (local stresses) with respect to the local rectangular coordinate system ($x'y'$ plane) will be denoted as σ'_{xx} , σ'_{yy} and σ'_{xy} and the local stresses with respect to the local polar coordinate system ($\rho\theta$ plane) will be denoted as $\sigma_{\rho\rho}$, $\sigma_{\theta\theta}$ and $\sigma_{\rho\theta}$, as Figure 2.7 shows.

The global biaxiality ratio λ is defined as the ratio of the horizontal force F_x to the vertical force F_y [5]:

$$\lambda = \frac{F_x}{F_y} = \frac{S_{xx}}{S_{yy}} \quad (2.17)$$

The local biaxiality ratio λ' is defined as:

$$\lambda' = \frac{S'_{xx}}{S'_{yy}} \quad (2.18)$$

Under the loading by the external stresses $S_x = S_{xx}$ and $S_y = S_{yy}$, as shown in Figure 2.5, and since $S_{xy} = 0$, equation (2.16) can be written as:

$$\begin{aligned} S'_{xx} &= \frac{1}{2}(S_{xx} + S_{yy}) + \frac{1}{2}(S_{xx} - S_{yy}) \cos 2\varphi \\ S'_{yy} &= \frac{1}{2}(S_{xx} + S_{yy}) - \frac{1}{2}(S_{xx} - S_{yy}) \cos 2\varphi \\ S'_{xy} &= S'_{yx} = -\frac{1}{2}(S_{xx} - S_{yy}) \sin 2\varphi \end{aligned} \quad (2.19)$$

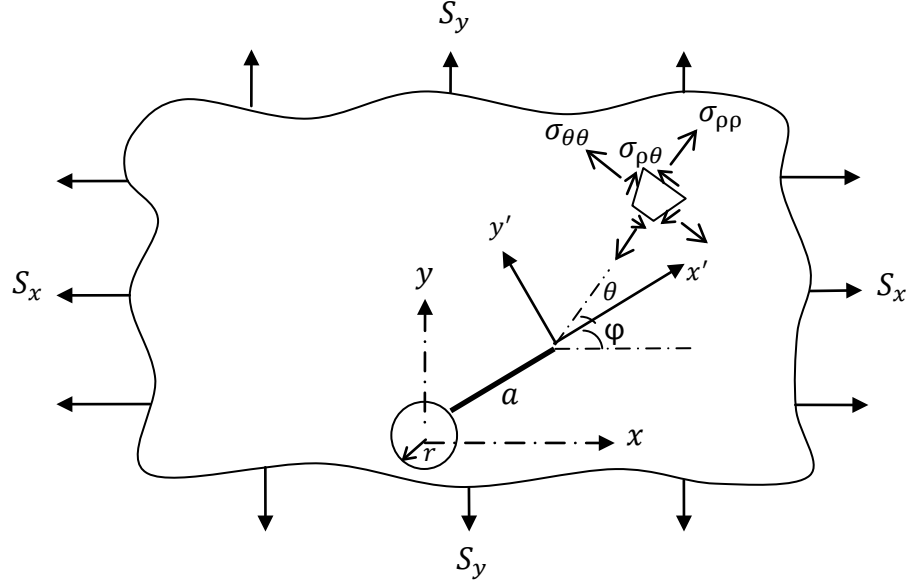


Figure 2.7: Remote And Local Stresses In Global And Polar Coordinate Systems, Respectively.

Placing equation (2.19) into equation (2.18) gives:

$$\lambda' = \frac{\lambda + 1 + (\lambda - 1) \cos 2\varphi}{\lambda + 1 - (\lambda - 1) \cos 2\varphi} \quad (2.20)$$

In our study $\varphi = 45^\circ$. So, setting $\varphi = 45^\circ$ in eq.(2.20), we receive

$$\lambda' = 1 \quad (2.21)$$

Also, when $\varphi = 45^\circ$ and $S_{xy} = 0$, as in the experiment of this study, the stresses at equation (2.19) take the form of:

$$S'_{xx} = S'_{yy} = \frac{S_{xx} + S_{yy}}{2}, S'_{xy} = \frac{S_{yy} - S_{xx}}{2} \quad (2.22)$$

Substituting equation (2.22) into equation (2.6), we receive

$$K_{II} = \frac{\sqrt{\pi r}}{\sqrt{2}} \sqrt{\frac{l_0 (l_0 + 2)^3}{(l_0 + 1)^3}} S'_{xy} \quad (2.23)$$

So, when $S'_{xy} = 0$, that is when the shearing stresses along the crack are zero, then $K_{II} = 0$, see Figure 2.8.

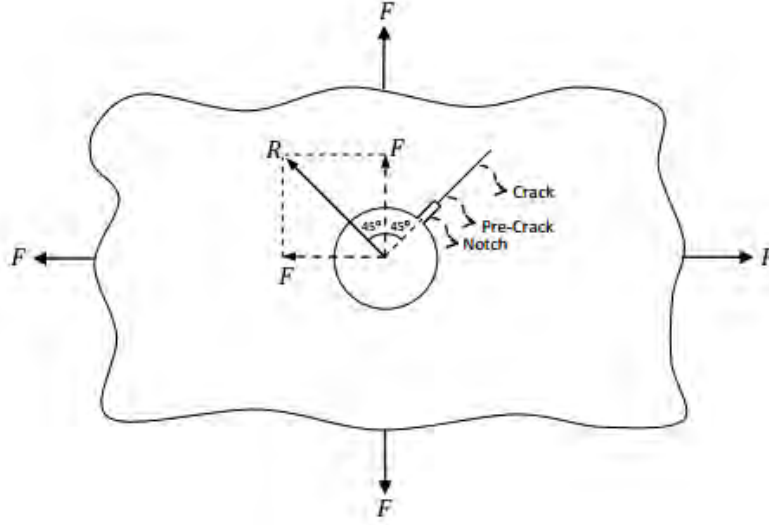


Figure 2.8: Propagation of The Crack when $\varphi = 45^\circ$, and $\lambda' = 1$.

Now, the local polar stresses can be written as a function of the angle θ and local transformed stresses as follow:

$$\begin{aligned}\sigma_{\rho\rho} &= \frac{1}{2}(\sigma'_{xx} + \sigma'_{yy}) + \frac{1}{2}(\sigma'_{xx} - \sigma'_y) \cos 2\varphi + \sigma'_{xy} \sin 2\varphi \\ \sigma_{\theta\theta} &= \frac{1}{2}(\sigma'_{xx} + \sigma'_{yy}) - \frac{1}{2}(\sigma'_{xx} - \sigma'_y) \cos 2\varphi - \sigma'_{xy} \sin 2\varphi \\ \sigma_{\rho\theta} &= \sigma_{\theta\rho} = -\frac{1}{2}(\sigma'_{xx} - \sigma'_{yy}) \sin 2\varphi + \sigma'_{xy} \cos 2\varphi\end{aligned}\tag{2.24}$$

Now, as Anderson stated in [5], the stress fields ahead of crack tip for mode I and mode II in linear elastic, isotropic material is defined as:

$$\begin{aligned}
\sigma'_{xx} &= \frac{K_I}{\sqrt{2\pi\rho}} \cos \frac{\theta}{2} \left(1 - \sin \frac{\theta}{2} \sin \frac{3\theta}{2} \right) - \frac{K_{II}}{\sqrt{2\pi\rho}} \sin \frac{\theta}{2} \left(2 + \cos \frac{\theta}{2} \cos \frac{3\theta}{2} \right) \\
\sigma'_{yy} &= \frac{K_I}{\sqrt{2\pi\rho}} \cos \frac{\theta}{2} \left(1 + \sin \frac{\theta}{2} \sin \frac{3\theta}{2} \right) + \frac{K_{II}}{\sqrt{2\pi\rho}} \sin \frac{\theta}{2} \cos \frac{\theta}{2} \cos \frac{3\theta}{2} \\
\sigma'_{xy} &= \sigma'_{yx} = \frac{K_I}{\sqrt{2\pi\rho}} \sin \frac{\theta}{2} \cos \frac{\theta}{2} \cos \frac{3\theta}{2} + \frac{K_{II}}{\sqrt{2\pi\rho}} \cos \frac{\theta}{2} \left(1 - \sin \frac{\theta}{2} \sin \frac{3\theta}{2} \right)
\end{aligned} \tag{2.25}$$

Substituting the last equation into equation (2.24) gives:

$$\begin{aligned}
\sigma_{\rho\rho} &= \frac{K_I}{4\sqrt{2\pi\rho}} \left(5 \cos \frac{\theta}{2} - \cos \frac{3\theta}{2} \right) + \frac{K_{II}}{4\sqrt{2\pi\rho}} \left(-5 \sin \frac{\theta}{2} + 3 \sin \frac{3\theta}{2} \right) \\
\sigma_{\theta\theta} &= \frac{K_I}{4\sqrt{2\pi\rho}} \left(3 \cos \frac{\theta}{2} + \cos \frac{3\theta}{2} \right) + \frac{K_{II}}{4\sqrt{2\pi\rho}} \left(-3 \sin \frac{\theta}{2} - 3 \sin \frac{3\theta}{2} \right) \\
\sigma_{\rho\theta} &= \sigma_{\theta\rho} = \frac{K_I}{4\sqrt{2\pi\rho}} \left(\sin \frac{\theta}{2} + \sin \frac{3\theta}{2} \right) + \frac{K_{II}}{4\sqrt{2\pi\rho}} \left(\cos \frac{\theta}{2} + 3 \cos \frac{3\theta}{2} \right)
\end{aligned} \tag{2.26}$$

And these are the local stresses in polar coordinate system as functions of stress intensity factors for mode I and mode II. This last equation, (2.26), will be used in the next section to predict the direction of crack propagation.

2.4.4 Direction of Crack Propagation

When $\sigma_{\theta\theta}(\theta)$ takes the maximum value, that is when $\theta = \theta^*$, then the crack propagates in the direction defined by the angle $\theta = \theta^*$ at which the stress component $\sigma_{\theta\theta}(\theta)$ takes the maximum value, according to Erdogan and Sih [10] (Figure 2.7). Thus, to find the crack propagation direction according to Erdogan and Sih criterion, the following equation is used:

$$\left. \frac{\sigma_{\theta\theta}}{\partial\theta} \right|_{\theta=\theta^*} = 0 \quad (2.27)$$

Substituting $\sigma_{\theta\theta}(\theta)$ from equation (2.26) into equation (2.27) and solving for θ^* , we receive the formula for the direction of crack propagation:

$$\theta^* = 2 \arctan \frac{1 - \sqrt{1 + 8 \left(\frac{K_{II}}{K_I} \right)^2}}{4 \left(\frac{K_{II}}{K_I} \right)} \approx -2 \frac{K_{II}}{K_I} + \frac{14}{3} \left(\frac{K_{II}}{K_I} \right)^3 + \dots \quad (2.28)$$

Other researchers tried to predict the direction of the crack propagation with the results shown below.

Sih Cha [39,40]:

$$\theta^* = -2 \frac{K_{II}}{K_I} - \frac{2\kappa - 30}{9 - 3\kappa} \left(\frac{K_{II}}{K_I} \right)^3 + \dots \quad (2.29)$$

where

$$\kappa = \begin{cases} 3 - 4\nu & \text{for plane strain} \\ \frac{3 - \nu}{1 + \nu} & \text{for plane stress} \end{cases} \quad (2.30)$$

and ν is the Poisson's ratio.

Berezhnitski and Gromyak criterion [6]:

$$\theta^* = -2 \frac{K_{II}}{K_I} - \frac{168 - 2(\kappa - 1)^2}{36 - 3(\kappa - 1)^2} \left(\frac{K_{II}}{K_I} \right)^3 + \dots \quad (2.31)$$

Tian, Lu and Zhu criterion [43]:

$$\theta^* = -2 \frac{K_{II}}{K_I} + \frac{20\kappa - 6}{3\kappa} \left(\frac{K_{II}}{K_I} \right)^3 + \dots \quad (2.32)$$

Tiroshu criterion [44]:

$$\theta^* = -2 \frac{K_{II}}{K_I} + \frac{20}{3} \left(\frac{K_{II}}{K_I} \right)^3 + \dots \quad (2.33)$$

This study uses thin specimens (plane stress condition) of aluminum alloy 7075-T6 for which the young's modulus E and the Poisson's ratio ν are [1]:

$$E = 7.17 \times 10^{10} \text{Pa}, \quad \nu = 0.33 \quad (2.34)$$

which make

$$\kappa = \frac{3 - \nu}{1 + \nu} = 2.0075 \quad (2.35)$$

and for the conditions of this study, the angle of the crack propagation in power series form using the previous formulas becomes:

Erdogan and Sih criterion:

$$\theta^* = -2 \frac{K_{II}}{K_I} + 4.6667 \left(\frac{K_{II}}{K_I} \right)^3 + \dots \quad (2.36)$$

Sih Cha criterion:

$$\theta^* = -2 \frac{K_{II}}{K_I} + 8.7271 \left(\frac{K_{II}}{K_I} \right)^3 + \dots \quad (2.37)$$

Berezhnitski and Gromyak criterion:

$$\theta^* = -2 \frac{K_{II}}{K_I} + 5.0363 \left(\frac{K_{II}}{K_I} \right)^3 + \dots \quad (2.38)$$

Tian, Lu and Zhu criterion:

$$\theta^* = -2 \frac{K_{II}}{K_I} + 5.6704 \left(\frac{K_{II}}{K_I} \right)^3 + \dots \quad (2.39)$$

Tiroshu criterion:

$$\theta^* = -2 \frac{K_{II}}{K_I} + 6.6667 \left(\frac{K_{II}}{K_I} \right)^3 + \dots \quad (2.40)$$

Because K_{II} is much less than K_I , the first term in eq. (2.36) to (2.40) will dominate the angle of crack propagation. Since all of equations (2.36) to (2.40) will give nearly the same answer, equation (2.36) will be used in later sections to predict the angle of the crack propagation.

2.5 Previous Research

The failure behavior due to the combined effect of corrosion and fatigue has been studied experimentally. These studies have been conducted with different types of materials and loading conditions. In 1985, McEvily used a fatigue testing machine to study crack growth in aluminum alloys 7075-T6 and 2024-T3 [24]. Paris was the first to study the stress intensity factor range (ΔK) versus the crack propagation rate (da/dN) [21]. Lately, several kinds of research have been carried out in different aspects of this subject and with the advanced technology. As stated earlier, researchers have already addressed investigating the crack propagation and the effect of environments on the crack growth behavior [26]. Documented information are available from those studies, but most of the studies had been performed under uniaxial fatigue condition while nearly all of aircraft structures are subjected to mixed mode of stresses, which can limit the benefits from the data of the uniaxial fatigue tests [5, 9, 26]. Current research focuses on using biaxial fatigue test

machines to characterize the crack growth behavior under the in-plane biaxial loading condition in both ambient air and the saltwater (3.5%) environment, using a fracture mechanics approach and cruciform-type specimens. Thus, studies about biaxial loading conditions need to be mentioned in detail.

Liu and Dittmer [23] had investigated the fatigue crack growth behavior of center-cracked using cruciform specimens of 7075-T7351 and 2024-T351 aluminum alloys under biaxial loading conditions with different biaxial stress ratios and the results showed that:

- 1) When the stress component parallel to the crack direction is equal or smaller than the stress component normal to the crack direction, the crack will grow in a straight line.
- 2) Depending on the biaxiality ratio, the stress parallel to the crack has small to negligible effects on crack growth rates.
- 3) The larger biaxial stress component controls the crack growth rate.

Hopper and Miller [17] used central circular notches and un-notched plates under biaxial stresses to study the propagation of fatigue cracks by using a servo-hydraulic testing machine. They did not cycle both the horizontal and vertical components of stresses at the same time because the machine they used was not capable of doing this function, so they kept the horizontal stress fixed while cycling the vertical stress component with $\lambda = -1, 0$ and 1. In addition, a microscope and curve-fitting technique were used to measure crack length. Also, a number of cycles was calculated to find out the crack growth rate. The results showed that:

- 1) Tensile loading parallel to the crack decreases the crack growth rates while the compressive loading result in increase in crack growth rates.

Anderson and Garrett [4] performed their own changeover tests on cruciform specimens made of steel with central crack to inspect the effect of biaxial stress on the crack growth. The biaxiality ratio (λ) was defined exactly as it is in this study, see equation (2.17). In the middle of the test they changed the biaxiality ratio and recorded the change in crack growth rate. Their results showed the following:

- 1) In biaxial loading with tensile stress parallel to the crack, the crack growth rate is lower than in uniaxial loading.
- 2) In biaxial loading with compressive stress parallel to the crack, the crack growth rate is higher than in uniaxial loading.

Sunder and Ilchenko put an effort to simulate the mixed mode of internal cabin pressure and gust loading in a laboratory environment in order to study the fatigue crack growth by applying biaxial quasi-static load, with constant amplitude, to cruciform test coupons. The cruciform specimen was made of steel of 1 mm thickness and was used in the first test which had been done under constant amplitude loading and aimed to examine the feasibility of the testing system and process. The other set of cruciform specimens was made of 2.7 mm thickness 2024-T3 aluminum alloy, and was tested under Marker-TWIST, which is described in reference [41], and it was concluded that the fatigue crack growth rates are sensitive to the load biaxiality [42].

Shanyavskiy, as well, carried out fatigue crack growth experiments under biaxial cyclic loadings using cruciform specimens with thickness of 1.2 to 10 mm and made of AK4-1T1 and Al-alloy D16T [38]. The biaxiality ratio had a value between -1.4 and +1.5, and the stress ratio range from 0.05 to 0.8. Under constant and variable amplitude of cyclic loads, he simulated the crack growth to characterize the crack closure effects under plane-

stress condition, plane-strain condition and out-of phase loading. He noticed that the plastic zone increased with the increase of phase difference from 0° to 180° , and it decreased with further increasing of the phase difference [38]. Also, he concluded that fatigue cracks grow faster with larger biaxiality stress ratios. [38]

Lee and Taylor [22] tried to examine three things in the field of fatigue. They looked into the effect of biaxial stresses on the fatigue life, fatigue crack growth and path. They tested aluminum alloys 1100-H14 and 7075-T651 cruciform specimens using sheets of 2 mm thickness with a horizontal or a 45° inclined center notch. These specimens were subjected to in-phase or out-of-phase biaxial load with biaxiality ratio λ ranging from 0 to 1.5, stress ratio $R=0.1$ and loading frequency 15 Hz in air. The results showed that:

- 1) As longitudinal stress decreased, the fatigue life increased for both in-phase and out-of-phase loading, but in-phase loading condition has better fatigue life comparing to the out-of-phase loading, at a given biaxiality ratio.
- 2) The path of fatigue crack was affected by biaxiality ratio, phase angle and initial center notch location.
- 3) For a high biaxiality ratio and under in-phase loading, the fatigue crack growth rate decreased which in return increase the fatigue life, while there was tiny change with change in biaxiality ratio under out-of-phase condition.

Yuuki et al. [47] also inspected the effect of biaxial stresses on the fatigue crack growth using biaxial fatigue testing machine. For center cracks, they tried to evaluate the stress intensity factor in cruciform specimens made of SUS 304 stainless steel with constant and changing biaxial stress condition tests, the biaxiality ratio, $\lambda = -1, 0$, and $+1$ and the stress ratio $R=0.1$, while using a travelling microscope to measure the crack length. The results

showed that the biaxiality had negligible effect on crack growth rates at low stress levels, but noticeable effect at high stress levels [47].

Misak, Perel, Sabelkin and Mall conducted fatigue crack growth experiments under biaxial cyclic loadings in ambient laboratory air and saltwater (3.5% NaCl) environments with biaxiality ratios, $\lambda=1$ and 1.5. The stress ratio was 0.5. They used cruciform specimens of aluminum alloy 7075-T6 with 3.18 mm thickness, and a center hole of 6 mm diameter with a machined notch of a 1 mm long and 0.25 mm wide at an angle 45° to horizontal and vertical arms [28, 29]. After that, the notch was pre-cracked under biaxial fatigue loading condition, and both the notch and the crack were perpendicular to the rolling direction of the specimen [28, 29]. An optical microscope system was used to measure the crack lengths. Also, they used a finite element analysis program to calculate the stress intensity factors. In the same configuration, the uniaxial fatigue crack growth experiments were conducted. The results stated that:

- 1) Crack initiated and grew coplanar with the notch under $\lambda = 1$, and non coplanar with the notch under $\lambda = 1.5$ [28].
- 2) Under biaxial fatigue, the crack initiation took place at a lower crack driving force level comparing to uniaxial fatigue, and when biaxiality ratio increased, the crack initiation driving force would decrease [28].
- 3) In air environment, crack growth rate was same for biaxial fatigue with $\lambda = 1$ and for the uniaxial fatigue ($\lambda = 0$), while it was faster when $\lambda = 1.5$, at a given crack driving force [28].

- 4) In saltwater environment, crack growth rate was the slowest for the uniaxial fatigue, it was the fastest for biaxial fatigue with $\lambda = 1.5$, and it was in-between for biaxial fatigue with $\lambda = 1$, at a given crack driving force [27].
- 5) Fatigue damage mechanisms, under air environment, were planar slip when $\lambda = 0$, wavy slip when $\lambda = 1.5$, and combination of the two when $\lambda = 1$ [27].
- 6) Fatigue damage mechanisms under saltwater environment showed that fatigue crack propagation was transgranular for both uniaxial and biaxial fatigue with $\lambda = 1$ [27].

2.6 Why This Thesis?

Much is known about fatigue crack growth under uniaxial loading conditions, but there is a limited number of studies under biaxial loading conditions. These studies have shown that biaxial fatigue has an effect on the crack growth rate. Some of these studies had addressed the in-phase or out-of-phase loading conditions [38]. None of them studied the effect of phase difference other than 0° and 180° on fatigue crack growth behavior of a material that is subjected to biaxial loading in air and saltwater environments. The present research is a unique study where the fatigue crack growth behavior of specimen made of 7075-T6 aluminum alloy was inspected under in-plane biaxial loading in both air and saltwater (3.5% NaCl) environments with 45° , 90° and 180° phase difference conditions and then compared to in-phase condition to study the effect of changing the phase on crack growth rate, which is what lacked in this field up to now. In addition, fracture mechanics was used to explain and predict the results. This research documents and presents the results of these experiments, which can be helpful in understanding the concept of corrosion fatigue and overcome this mode of failure in the coming future.

III. Methodology

3.1 Material

Aluminum alloy 7075, where zinc is the main alloying element, is the material that is used in this research. Besides of its high strength-to-density ratio, it also has other good essential properties that are suitable for aerospace applications. Table 3.1 shows the chemical composition of AA 7075-T6 [3]. Its strength is as good as strength of many steels, and has good fatigue strength, but it has a reduced resistance to corrosion comparing to other Aluminum alloys [3]. It has several tempers where T6 is the type of temper that is chosen for this research, because it is used in aeronautical applications. This temper is typically attained by homogenizing the cast 7075 at 450C for several hours, followed by aging at 120C for 24 hours [3, 1].

Table 3.1: Chemical compositions of AA7075-T6 alloy [3].

Element	Weight Percentage
Aluminum	87.1 - 91.4
Zinc	5.1-6.1
Magnesium	2.1-2.9
Copper	1.2-2
Iron	Max 0.5
Silicon	Max 0.4
Manganese	Max 0.3
Chromium	0.18-0.28
Titanium	Max 0.2
Other	each Max 0.05
Other	total Max 0.15

The necessity of using aluminum alloy 7075-T6 in the aerospace structure is increased when the mixture of high strength, low density, moderate toughness and corrosion resistance is needed [3]. Thus, AA 7075-T6 is one of the most common alloys used in the aircraft structures. Table 3.2 shows AA 7075-T6 mechanical properties [3].

Table 3.2: Mechanical properties of AA 7075-T6 [3].

Mechanical Properties			
	Metric	English	Comments
Hardness, Brinell	150	150	AA; Typical; 500 g load; 10 mm ball
Hardness, Knoop	191	191	Converted from Brinell Hardness Value
Ultimate Tensile Strength	572 MPa	83000 psi	AA; Typical
Tensile Yield Strength	503 MPa	73000 psi	AA; Typical
Elongation at Break	11 %	11 %	AA; Typical; 1/16 in. (1.6 mm) Thickness
Modulus of Elasticity	71.7 GPa	10400 ksi	AA; Typical; Average of tension and compression. Compression modulus is about 2% greater than tensile modulus.
Poisson's Ratio	0.33	0.33	
Fatigue Strength	159 MPa	23000 psi	AA; 500,000,000 cycles completely reversed stress;
Fracture Toughness	20 MPa-m ^{1/2}	18.2 ksi-in ^{1/2}	K(IC) in S-L Direction
Fracture Toughness	25 MPa-m ^{1/2}	22.8 ksi-in ^{1/2}	K(IC) in T-L Direction
Fracture Toughness	29 MPa-m ^{1/2}	26.4 ksi-in ^{1/2}	K(IC) in L-T Direction
Machinability	70 %	70 %	0-100 Scale of Aluminum Alloys
Shear Modulus	26.9 GPa	3900 ksi	
Shear Strength	331 MPa	48000 psi	AA; Typical
Density	2.81 g/cc	0.102 lb/in ³	AA; Typical

3.2 Test Specimens

The test specimens, used in this study, were cruciform specimens. As stated, the material of this study was 3.18 mm thick sheet of 7075-T6 aluminum alloy. These sheets were used to machine cruciform specimens with a length of 120 mm and a width of each arm of 45 mm, and a radius of curvature at the junction of arms of 45 mm. Each specimen had a hole of 6 mm diameter, which was drilled at the center of the specimen, and then a notch of 1 mm length and 0.25 mm width was machined to create stress concentration, using electro-discharge method, at an angle of 45° to horizontal and vertical arms. Thus, the crack was formed, later, at the location of the stress concentration. Next, a precrack of length 1mm was created from the machined notch and collinearly to it, under biaxial cyclic loading with biaxility ratio, $\lambda = 1$, with phase difference equal to 0° . The pre-cracking was performed by fatigue to create initial sharp crack, because the machined notch (0.25 mm wide) is not sharp enough. The initial crack had to be sharp in order for the initial stress intensity factor to be meaningful, because the stress intensity factor is a characteristic of a very sharp crack [5]. The applied maximum and minimum loads throughout the precracking of the specimens were similar to that during the actual tests. Figure 3.1 shows the experimental setup for biaxial loading along with the cruciform specimens.

In a separate study, uniaxial fatigue crack growth tests, which are considered as tests with $\lambda = 0$, were carried out with the use of the same material and with the same method of creating a precrack originating from the notch near the circular hole [28]. In these specimens, the notches and the precracks were created perpendicular to the applied loads and not at 45° as in the biaxial specimens. Also, the uniaxial specimens have rectangular shapes. Figure 3.2 shows the uniaxial experimental setup along with a test specimen.

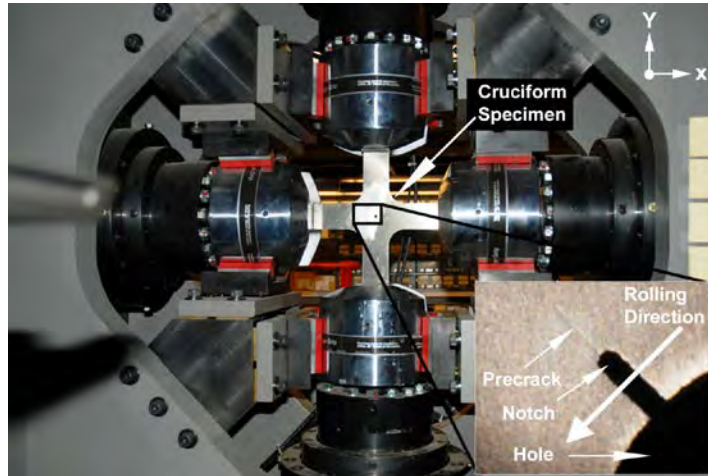


Figure 3.1: The Biaxial Experimental Setup with a Cruciform Specimen.

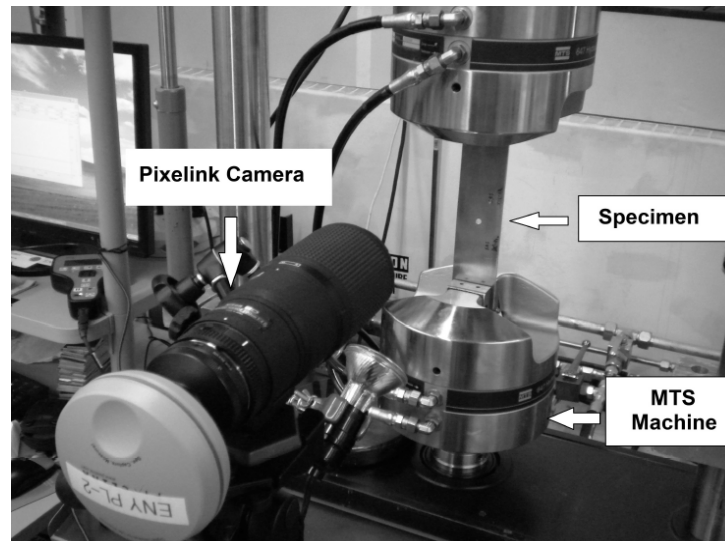


Figure 3.2: The Uniaxial Experimental Setup with a Test Specimen.

The cruciform and rectangular specimens were cut in such a way that the notch and the precrack were perpendicular to the rolling direction, because all the previous tested specimens had been done in this way, and in order to compare the experiments in this research with the previous ones.

3.3 Test Procedures

After preparing the cruciform specimens, a Material Testing System machine (MTS) was used to conduct the biaxial experiments. This MTS has the ability to apply a cyclic biaxial loading in vertical and horizontal directions separately, which could let a researcher create the phase differences between the two applied cyclic loads as desired. In the experiments, the stress ratios for the horizontal and vertical loading were $R_x=R_y=0.5$, respectively. These stress ratio values were chosen to minimize the crack closure effect. The frequency of both applied loads was 10 Hz.

Throughout the tests, images of the cracks were taken after certain numbers of cycles to capture the crack behaviors by using a PixelINK camera having a resolution of 3 mega-pixels with an AF Micro Nikko 200 mm lens. When a crack reached a length of about 20 mm, the experiment was stopped and the specimen was considered a failure.

After conducting the tests, “uSCOPE” software was used to measure the crack lengths from the images which had been taken during the tests with a resolution of a 0.01 mm. Figure 3.1 and Figure 3.2 show the set up of the experiments.

All of previous procedures had been done in air. Then, by using a chamber that has saltwater (3.5% NaCl) in it, the tests have been conducted again to find the effect of the corrosion on the crack behavior under fatigue loads. Figure 3.3 shows the cruciform specimen with saltwater chamber attached to it.

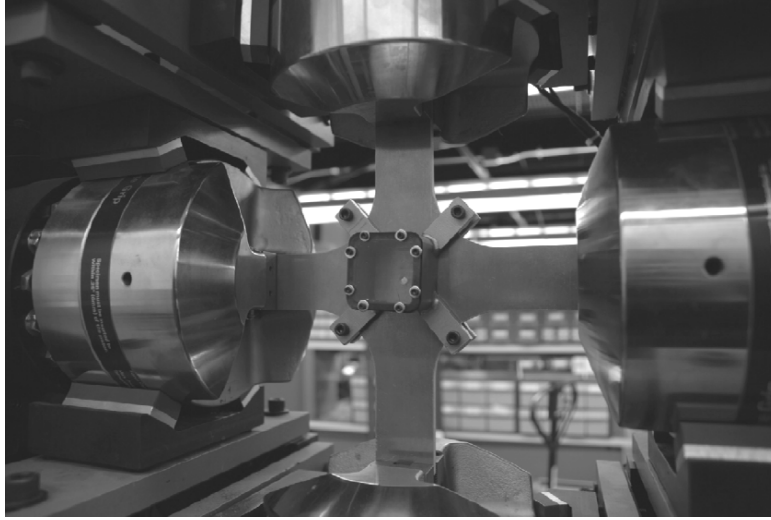


Figure 3.3: The Cruciform Specimen With Saltwater Chamber Installed To It.

3.4 Finite Element Modeling

In order to address the phase differences 45° , 90° or 180° between the applied loads, a dynamic finite element analysis was carried out, using finite element program called Abaqus. After that, stress intensity factors (K) and strain energy release rate (G) were calculated. The strain energy release rate is related to mode I stress intensity factor (K_I) and mode II stress intensity factor (K_{II}), as follow:

$$G = \frac{K_I^2}{E} + \frac{K_{II}^2}{E} \quad (3.1)$$

where E is the Young's modulus.

The maximum and minimum external stresses, applied to the arms of the specimens, were:

$$(S_x)_{\max} = (S_y)_{\max} = 1.055 \times 10^8 \text{ Pa} \quad (3.2)$$

$$(S_x)_{\min} = (S_y)_{\min} = 5.274 \times 10^7 \text{ Pa} \quad (3.3)$$

The time variation of the applied remote stresses was:

$$S_x(t) = \frac{(S_x)_{\max} + (S_x)_{\min}}{2} + \frac{(S_x)_{\max} - (S_x)_{\min}}{2} \sin(\omega t) \quad (3.4)$$

$$S_y(t) = \frac{(S_y)_{\max} + (S_y)_{\min}}{2} + \frac{(S_y)_{\max} - (S_y)_{\min}}{2} \sin(\omega t + \gamma) \quad (3.5)$$

Where t is the time, γ is the phase difference between the applied loads, and ω is the frequency of the applied load.

. Therefore the biaxility stress ratio $\lambda \equiv \frac{S_x}{S_y}$ is time-dependent. In these experiments,

$(S_x)_{\max} = (S_y)_{\max}$ and $R_x = R_y = 0.5$, so:

$$\lambda(t) = \frac{1.5 + 0.5 \sin(\omega t)}{1.5 + 0.5 \sin(\omega t + \gamma)} \quad (3.6)$$

Equation 3.6 provides the values of the biaxility stress ratio with time.

Now, Equation 3.1 shows that the strain energy release rate can be calculated if K_I and K_{II} are known, along with the Young's modulus. Abaqus was used to calculate the stress intensity factors of the test specimens, for both modes. For Abaqus, following assumptions have to be made, and they are as follow:

1. The aluminum alloy 7075-T6 material was isotropic and homogeneous.
2. The mechanical properties of the aluminum alloy were constant during the experiments ($E=73 \text{ GPa}$, $\nu=0.33$).

3. The hole has a uniform shape with smooth edges.
4. The specimens have no flaws and the cracks initiated from either the precracked notched hole or the corroded precracked notched hole.
5. There is no variation in the applied loads.

In Abaqus, a specimen was modeled having exactly the same dimensions as that of the actual specimen. Then, a notch and precrack were put from the drawn specimen in order to match the real specimens. Then, the sketch is added to a part. After that, the material (AA 7075-T6) and its properties were assigned to the part. Next, the precrack direction was specified to the tip of the precrack with setting all the needed constraints around it. Afterward, the dynamic loads and the specimen constraints were specified to the part. Next, a mesh was created to the whole specimen. Then, a job was created and submitted to run the model. Finally, the results, which have K_I , K_{II} , G and the direction of the precrack, were taken from the computed results. As a result of the first run, the precrack bifurcated into two cracks. Therefore, this whole process was repeated couple of times for the two cracks to find out K_I , K_{II} , G and the direction of the cracks as the cracks grow after certain number of cycles. Appendix A shows the figures that illustrate the steps of the procedure of calculating K_I , K_{II} , G and the direction of the cracks in case of biaxial fatigue test with a 45° of phase difference, using Abaqus. The other cases have the exact same procedures, but with changing the lengths of the two cracks and the dynamic loads.

IV. Results and Discussion

4.1 Overview

As mentioned in the previous chapters, the fatigue crack growth behavior of specimens prepared from 7075-T6 aluminum alloy were tested under in-plane biaxial loading in both ambient air and saltwater (3.5% NaCl) environments with 45°, 90° and 180° phase difference between biaxial fatigue loads and then compared to uniaxial fatigue test and biaxial fatigue test with no phase difference to study the effects of the phase difference on crack propagation path and crack growth rate.

Section 4.2 will study the crack propagation path in specimens tested under uniaxial and biaxial with and without phase differences in air and saltwater environments. Then, section 4.3 will present and study the effects of the phase difference on the crack growth rate in both air and saltwater environments. Table 4.1 shows a summary of the biaxial tests under fatigue loads with 0°, 45°, 90° and 180° phase differences in air and saltwater environments.

Table 4.1: Summary of biaxial tests with 0°, 45°, 90° and 180° phase differences in air and saltwater environments.

Environment	Phase Difference (°)	$R_{x,y}$	λ	Frequency (Hz)	Crack Splitting	Total Initial ΔG (N/m) (FEA)
Air	0	0.5	1	10	No	316.42
Air	45	0.5	1	10	Yes	357.13
Air	90	0.5	1	10	Yes	812
Air	180	0.5	1	10	Yes	1138
Saltwater	0	0.5	1	10	No	302.72
Saltwater	45	0.5	1	10	Yes	560.38
Saltwater	90	0.5	1	10	Yes	834
Saltwater	180	0.5	1	10	Yes	1000.5

4.2 Crack Path

4.2.1 Crack Path of Uniaxial and Biaxial Specimens without Phase Difference in Air and Saltwater Environments

For the sake of clarification and comparison, the uniaxial and biaxial cases will be discussed in this section. The baseline case is the uniaxial one ($\lambda = 0$), where rectangular specimens made of AA 7075-T6 material have been tested under fatigue loads in air and saltwater environments, both gave the same result from crack path point of view. Figure 4.1 show the crack path of a uniaxial specimen tested under cyclic load in air and saltwater. In both environments, the crack path was collinear to the notch and precrack direction and at an angle of 90° to the direction of loads. In each case, up to the failure of the specimens, the crack path did not change at all due to the absence of mode II stress intensity factor ($K_{II} = 0$). [27]

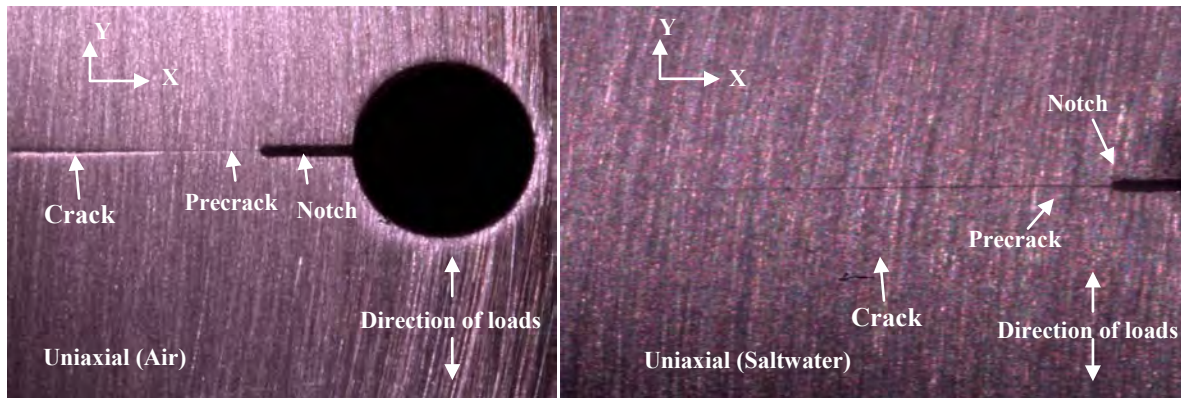


Figure 4.1: The crack path of an AA 7075-T6 uniaxial specimen tested under cyclic load in air and saltwater environments.

The biaxial cruciform specimens has biaxility ratio of $\lambda = 1$, i.e. fatigue loads in vertical and horizontal directions were equal and in-phase. There is no phase difference

applied between the horizontal and vertical loads. The result of the biaxial fatigue test in air and saltwater environments with no phase difference was a crack with a path collinear with the notch as in the case of the uniaxial fatigue [27]. However, the notch was at 45° to the directions of the applied forces in biaxial case and so was the crack. Figure 4.2 shows the crack path of an AA 7075-T6 biaxial specimen tested under cyclic load in air environment. From crack path point of view, the test in saltwater environment had the same result as in air environment.

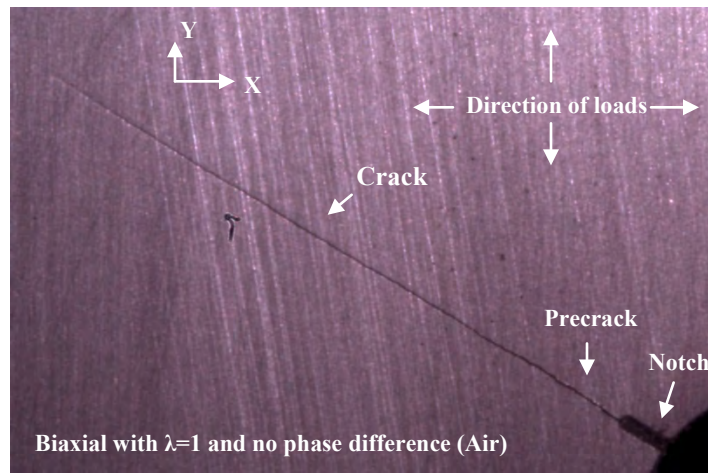


Figure 4.2: The crack path of an AA 7075-T6 biaxial specimen tested under cyclic load in air environment. [28]

This initial collinear crack didn't change its path as it grew. Therefore, same explanation as the uniaxial could be concluded from the collinear path of the crack in the biaxial test with no phase difference which is the absence of the mode II stress intensity factor. This conclusion can be proved analytically using equation (2.36) which is the expansion in power series of Erdogan and Sih criterion to predict the direction of the crack propagation and also, from the finite element analysis. Figure 4.3 shows the direction of crack propagation for this case.

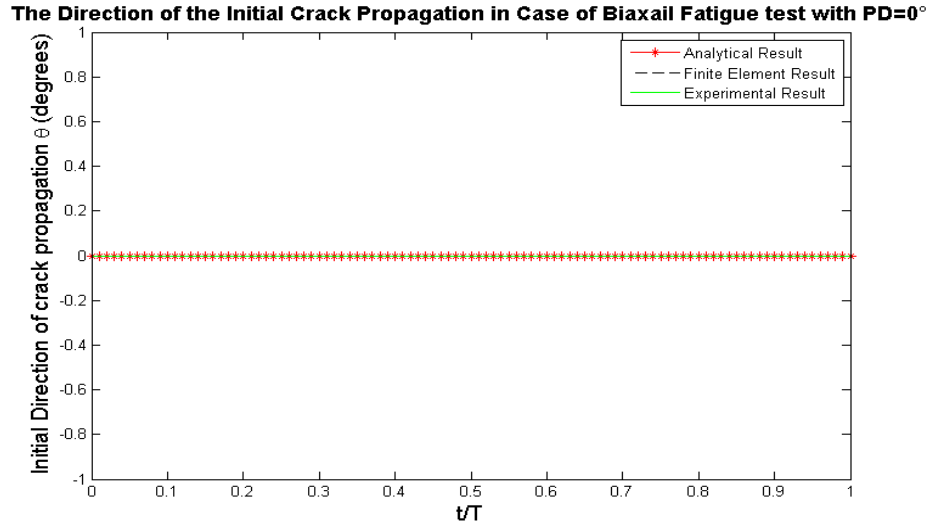


Figure 4.3: The direction of the initial crack path of an AA 7075-T6 biaxial specimen with no phase difference tested under cyclic load in air environment using analytical, finite element and experimental methods.

4.2.2 Crack Path of Biaxial Specimens with Phase Differences

The next biaxial cruciform tests were conducted in air and saltwater environments with biaxility ratio of $\lambda = 1$. The phase differences between the applied horizontal and vertical loads were 45° , 90° and 180° , respectively. These specimens have the same configuration as the biaxial fatigue test with no phase difference, as stated in section 4.2.1, except that the applied loads for each specimen had different phase, i.e. 45° , 90° or 180° .

4.2.2.1 Crack Path of Biaxial Specimens with 45° Phase Difference in Air and Saltwater Environments

For this case, the phase difference between the applied horizontal and vertical loads was set to be 45° (PD= 45°). Two approaches have been done. First approach is

done by applying the loads in the Y-direction, and after one-eighth of a cycle the loads in the X-direction start to be applied, which makes a phase difference of 45° , Figure 4.4.a. It resulted in the formation of two unsymmetrical cracks. Figures 4.4.b and 4.4.c show that these two cracks are not symmetric with respect to the direction of the precrack. The horizontal crack has a length of 3.8 cm while the vertical crack has a length of 0.69 cm. Also, it shows that they grew without any further splitting.

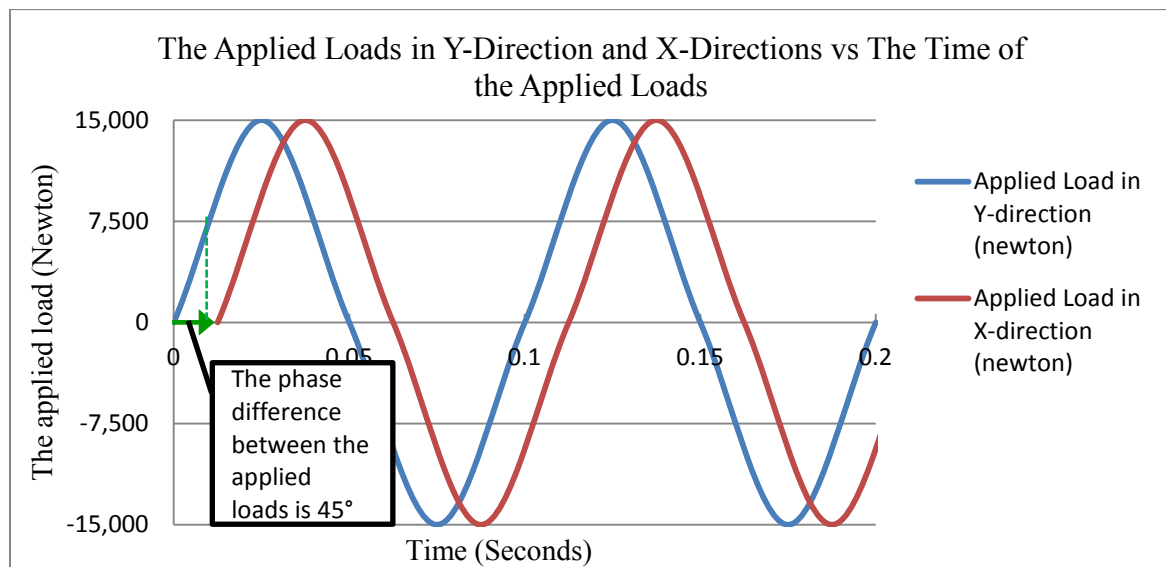


Figure 4.4.a: The applied loads in the Y-Direction and X-Directions versus the Time, when the loads in Y-direction applied, and after one-eighth of a cycle the loads in the X-direction start to be applied, which makes a phase difference of 45° .

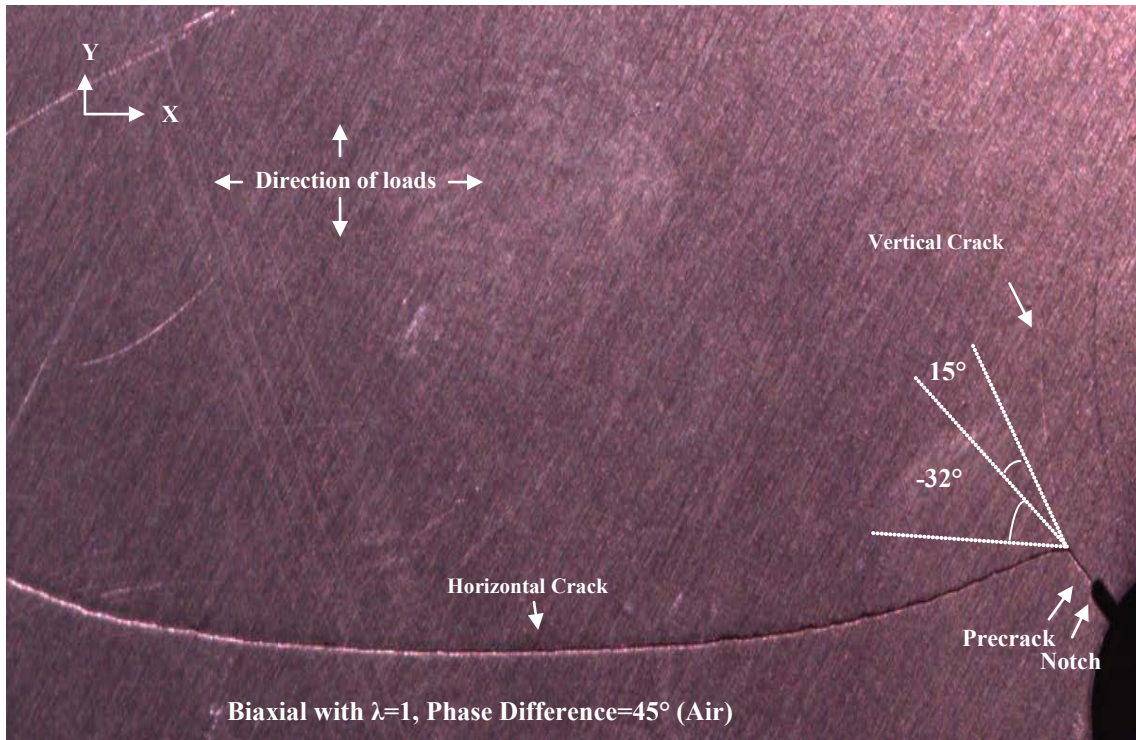


Figure 4.4.b: The Direction of the Two Cracks Of an AA 7075-T6 Biaxial Specimen, with applying the loads in the Y-direction, first, and after phase difference between the applied loads of 45° , the loads in the X-direction start to be applied, Tested Under Cyclic Load in Air Environment.

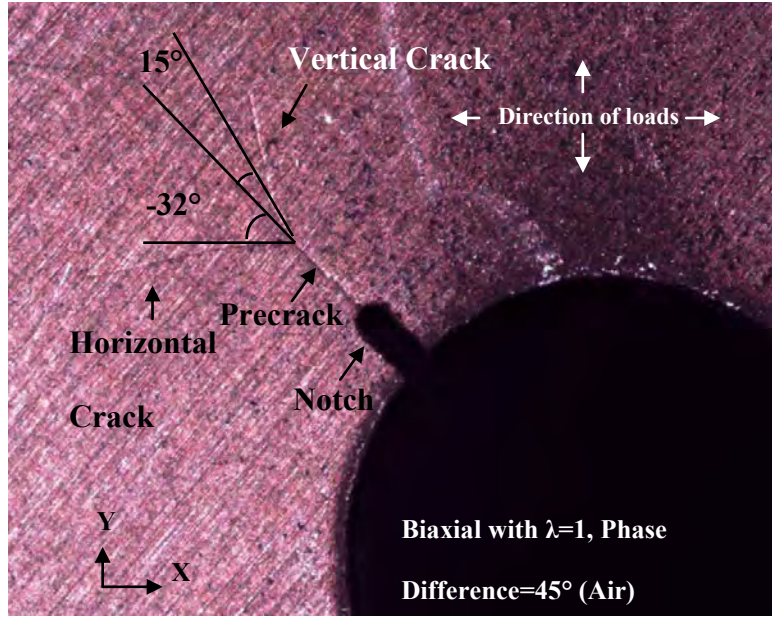


Figure 4.4.c: The direction of the two cracks of an AA 7075-T6 biaxial specimen, with applying the loads in the Y-direction and after one-eighth of a cycle, the loads in the X-direction start to be applied, which makes a phase difference of 45° , tested under cyclic load in air environment (closer picture).

The second approach was done by applying the loads in the X-direction and after one-eighth of a cycle, the loads in the Y-direction start to be applied, which makes a phase difference of 45° , Figure 4.5.a. Also, it resulted in the formation of two unsymmetrical cracks, but with swapping the horizontal crack values with the vertical cracks one. So, the vertical crack has a length of 3.8 cm while the horizontal crack has a length of 0.69 cm, Figure 4.5.b and 4.5.c.

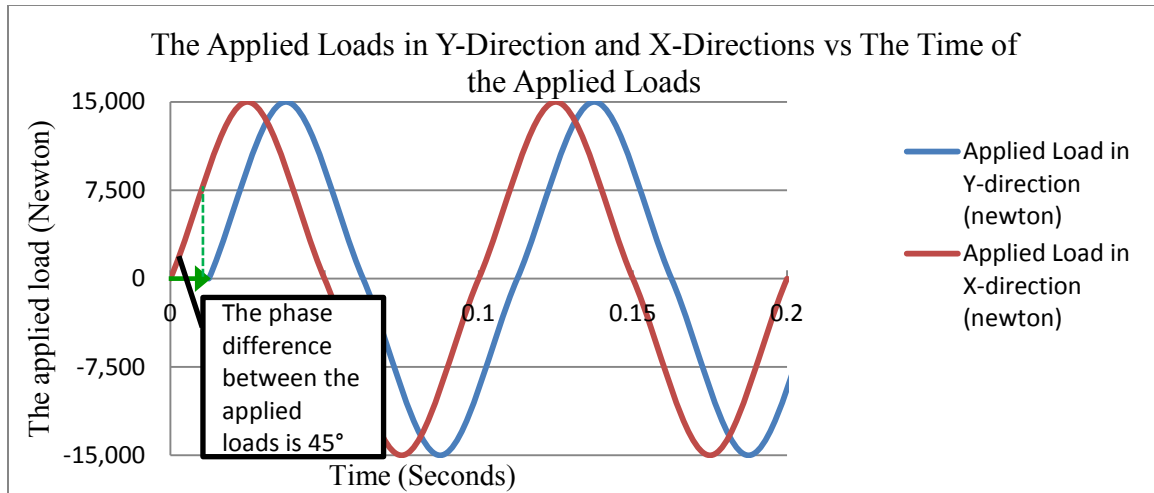


Figure 4.5.a: The applied loads of the Y-Direction and X-Directions versus the Time, when applying the loads in the X-direction and after one-eighth of a cycle, the loads in the Y-direction start to be applied, which makes a phase difference of 45° .

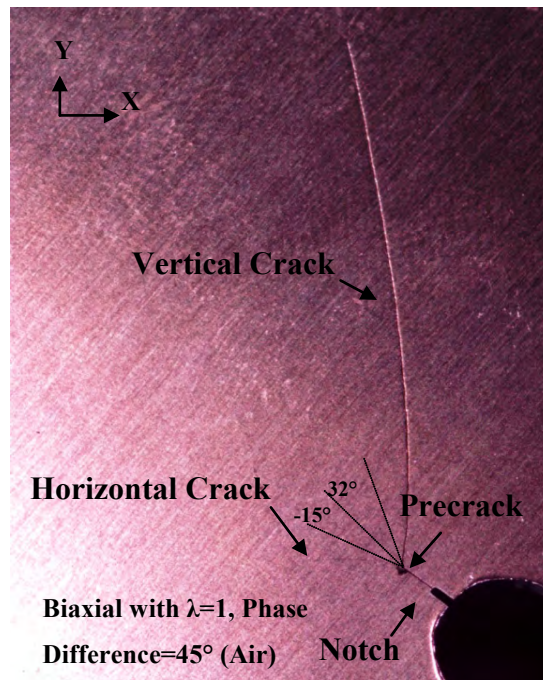


Figure 4.5.b: The direction of the two cracks of an AA 7075-T6 biaxial specimen, when applying the loads in the X-direction and after one-eighth of a cycle, the other load applied, which makes a phase difference of 45° , tested under cyclic load in air environment.

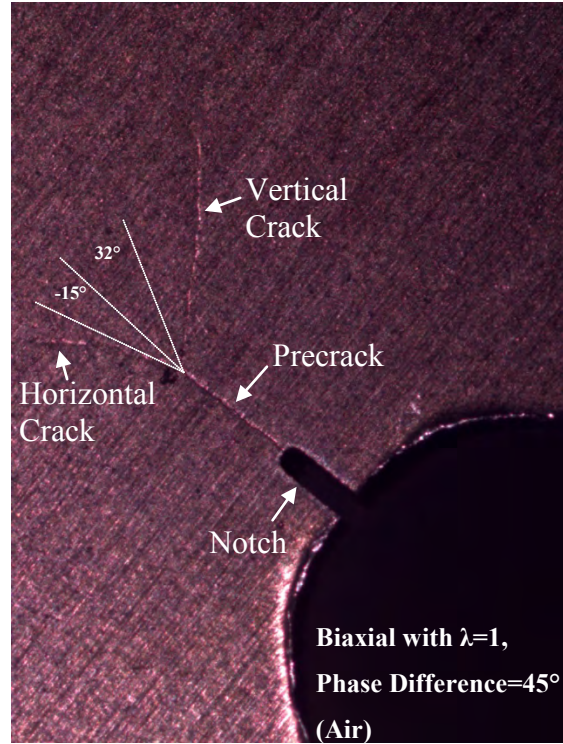


Figure 4.5.c: The direction of the two cracks of an AA 7075-T6 biaxial specimen, when applying the loads in the X-direction and after one-eighth of a cycle, the other load applied, which makes a phase difference of 45° , tested under cyclic load in air environment. (Closer Picture).

Two solutions has been addressed to study this splitting behavior of the precrack into two unsymmetrical cracks under biaxial loads with $PD=45^\circ$. These solutions are analytical solution, and Finite Element Analysis (FEA). Equation (2.36) and values of stress intensity factors before the precrack split, calculated from the finite element analysis, were used to plot the initial directions of the crack propagation (θ°) from the precrack direction as a function of time under the biaxial loading with a phase difference of 45° to help understanding the reason for the splitting of the precrack into two

unsymmetrical cracks. Figures 4.4.c provide a closer look to these angles which are calculated experimentally.

Since, starting either the applied load in the Y-direction, first, or X-direction, just swap the two formed cracks characteristics, the analysis will be focused on the case of starting Y-direction applied load first.

As Figure 4.6 shows, the analytical and FEA curves indicates that the maximum angle in one loading cycle is $+15^\circ$ and the minimum angle is -15° , except that the minimum angle in one loading cycle, calculated experimentally, is -32° . Since all methods agreed in calculating the initial angles of the crack propagation, it is very possible that the minimum angle that is calculated experimentally was -15° initially, and then it changed suddenly to -32° . So, when the load is applied with $PD = 45^\circ$, one crack was expected to develop in the direction $+15^\circ$ with respect to the precrack path throughout the first half-cycle of loading, which exactly happened experimentally when the maximum $\theta(t)$ reached. Similarly, the other crack should grow in the direction of -15° as in the analytical and FEA solutions through the second half-cycle load, in which the minimum $\theta(t)$ affect the precrack tip. Consequently, the chances of the precrack to grow in the two directions are feasible, which can cause splitting the precrack into two cracks, and this is exactly what happened in the experiment, Figure 4.4.b.

Figures 4.4.b and 4.4.c show the two cracks' initial angles as seen experimentally are $+15^\circ$ for the vertical crack, with crack length of 0.69 cm, and -32° for the horizontal crack, with crack length of 3.8 cm. These two cracks did not split any further down the path and by plotting the instant directions of further crack propagation of the two cracks

during the 10,001st fatigue cycle, the crack path can be addressed for each one of them using equation (2.36) and values of the stress intensity factors obtained from the FEA, Figure 4.7.a and Figure 4.7.b.

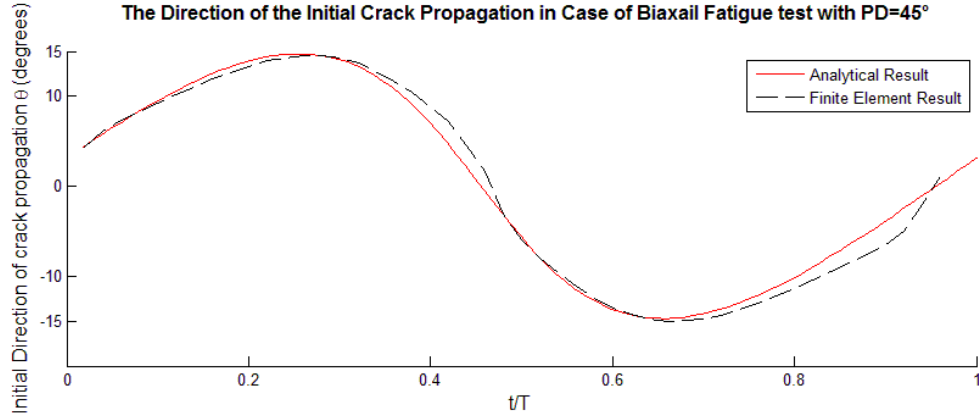


Figure 4.6: The direction of the initial crack path of an AA 7075-T6 biaxial specimen before the crack split with phase difference=45°, tested under cyclic load in air environment using analytical and finite element methods.

It was found in the experiment that at the 10,001st cycle of fatigue loading, after the initial formation of the two cracks, the further branching of these cracks did not occur. In the figure 4.7.a (for the horizontal crack), the absolute value of the maximum angle of crack propagation is very close 0°, $|\theta_{max}| \approx 0$, and the absolute value of the minimum negative angle of crack propagation is 29°, $|\theta_{min}| = 29^\circ$, i.e. $|\theta_{max}|$ is very small as compared to $|\theta_{min}|$. This explains why further branching of the two cracks is not probable, i.e. why they keep propagating as shown in Figure 4.7.a.

Similar explanation may be applicable for the vertical crack. In the figure 4.7.b (for the vertical crack), the absolute value of the maximum angle of crack propagation is 17° , $|\theta_{max}| = 17^\circ$, and the absolute value of the minimum angle of crack propagation is 16° , $|\theta_{min}| = 16^\circ$, i.e. $|\theta_{max}|$ is very close to $|\theta_{min}|$. This explains why further branching of the two cracks is not probable, i.e. why they keep propagating as shown in Figure 4.7.a. In the saltwater environment, the same crack path was observed in the test.

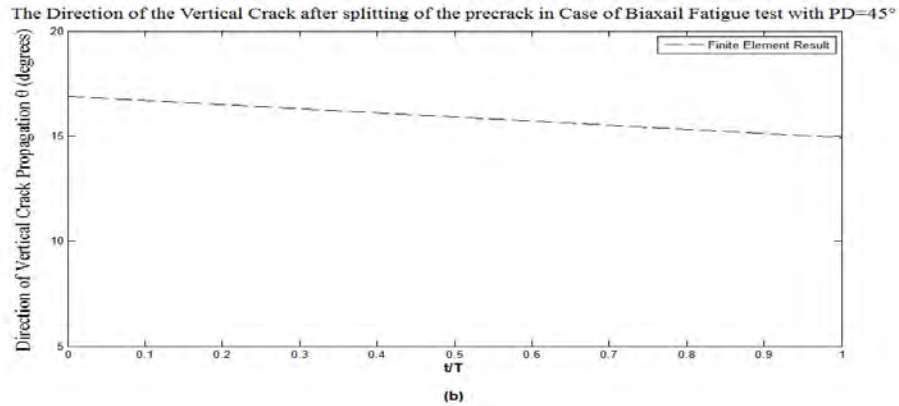
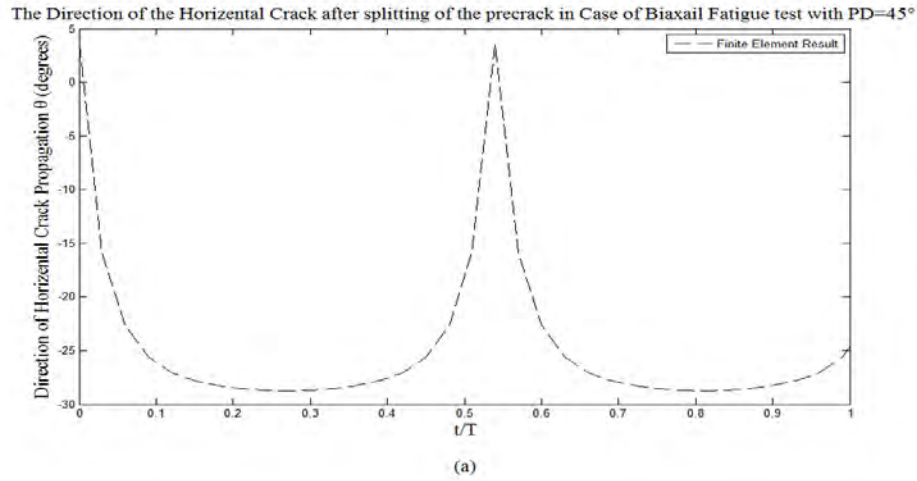


Figure 4.7: Variation of the horizontal (a) and vertical (b) cracks propagation, after bifurcation exists, under biaxial fatigue during one cycle with PD= 45°.

Figure 4.8 shows the strain energy release rate versus the number of cycles when the PD=45 ° in air and saltwater environments, for both horizontal and vertical cracks. In air environment, the horizontal and the vertical cracks have the same strain energy release rate up to around 460,000 cycles, where the strain energy release rate for the horizontal crack start to increase dramatically. The strain energy release rate for the vertical crack kept increasing, with increasing the number of cycles. This explains why the horizontal crack is longer than the vertical one, since it has more strain energy release rate than the vertical one. In the saltwater environment, the strain energy release rate for the horizontal crack is more than that for the vertical crack, which caused the horizontal crack to be longer than the vertical one, as noticed from the experiment.

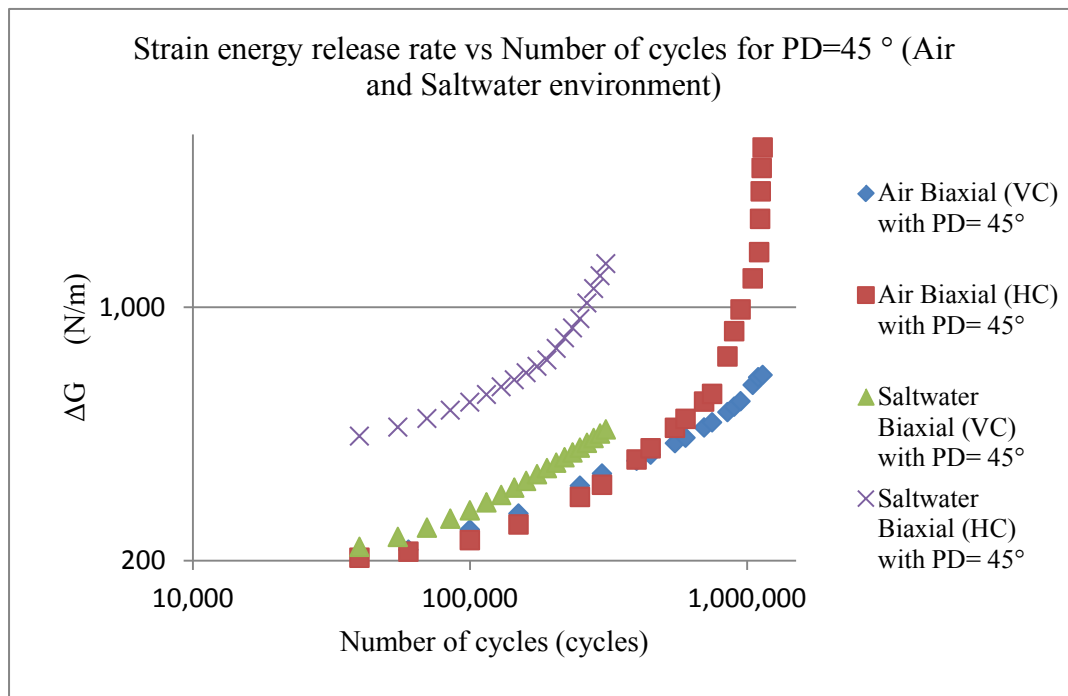


Figure 4.8: Strain energy release rate versus number of cycles when the phase difference is 45° in air and saltwater environments.

4.2.2.1 Crack Path of Biaxial Specimens with 90° Phase Difference in Air and Saltwater Environments

The loads in the Y-direction, and after one-fourth of a cycle the loads in the X-direction start to be applied, which makes a phase difference of 90°, Figure 4.9.a. The result is two cracks, formed nearly symmetric with respect to the direction of the precrack and the notch as shown in Figures 4.9.b. These two cracks grew without any additional division.

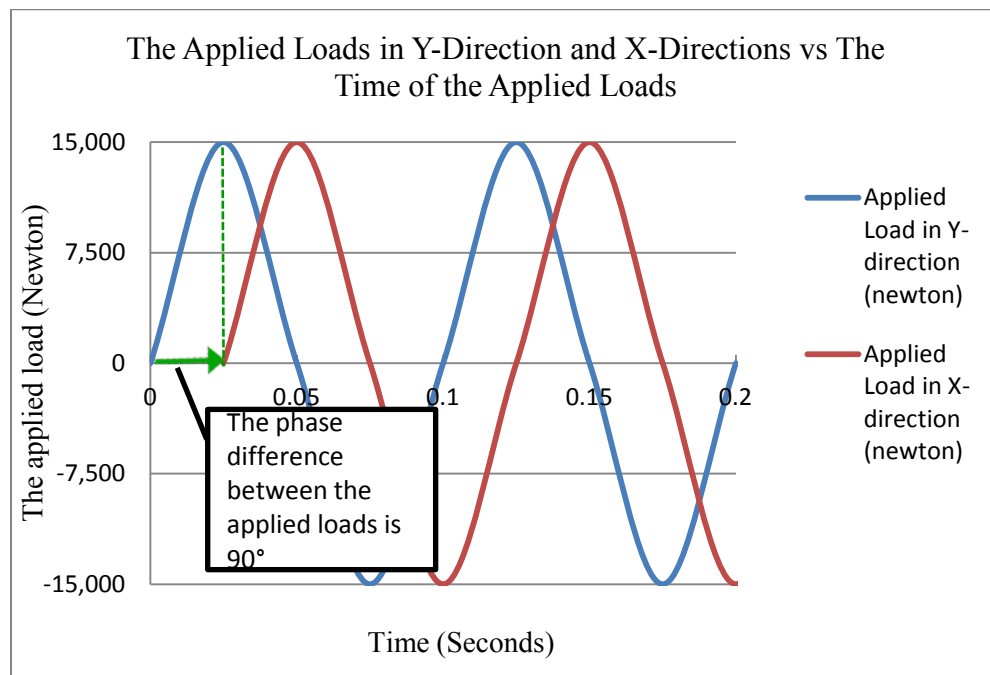


Figure 4.9.a: The applied loads of the Y-Direction and X-Directions versus the Time, when applying the loads in the Y-direction, and after one-fourth of a cycle the other load applied which makes a phase difference of 90°.

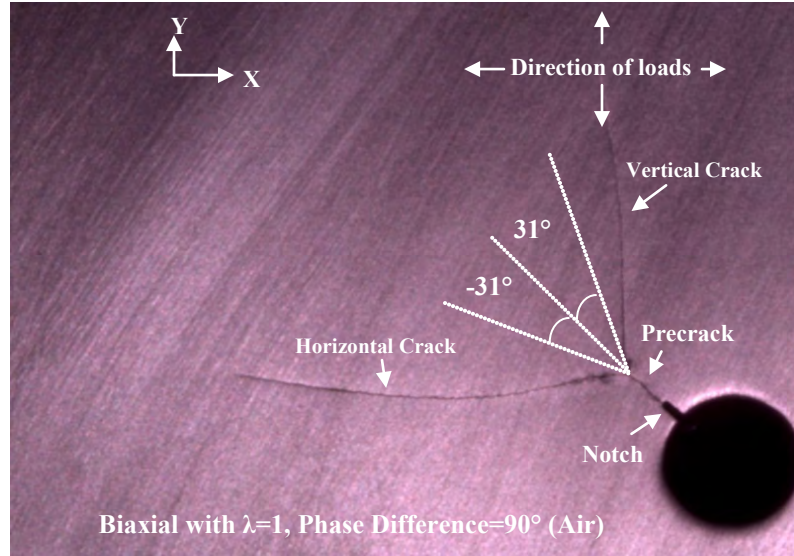


Figure 4.9.b: The direction of the crack path of an AA 7075-T6 biaxial specimen with $PD=90^\circ$ tested under cyclic load in air environment.

Since, starting either the applied load in the Y-direction, first, or X-direction, just swap the two formed symmetric cracks characteristics, which does not change the result, the analysis will be focused on the case of starting Y-direction applied load first.

This behavior can be explained by using equation (2.36) and values of stress intensity factors calculated from the finite element analysis before the crack split to plot the angle of the initial directions of the crack propagation from the precrack direction as a function of time under the biaxial loading with a phase difference of 90° to find out the crack path, Figure 4.10.

The analytical solution showed that the maximum angle in one loading cycle is $+24^\circ$ and the minimum angle is -24° . On the other hand, the finite element solution gave a close result where the maximum angle in one loading cycle is $+29^\circ$ and the minimum is

-29°. So, when the load is applied, one crack should grow in the direction ranging around +24° or +29° with respect to the precrack path throughout the first half-cycle of loading. This happens when the maximum $\theta(t)$ reached. The other crack should grow in the direction close to -24° or -29° through the second half-cycle of loading, in which the minimum $\theta(t)$ have affect. As a result, both directions of crack splitting are equally possible and that's why the crack splits in these two directions. This clarifies the initial pattern of the two cracks and their symmetry with respect to the precrack, as can be shown in Figure 4.9.b.

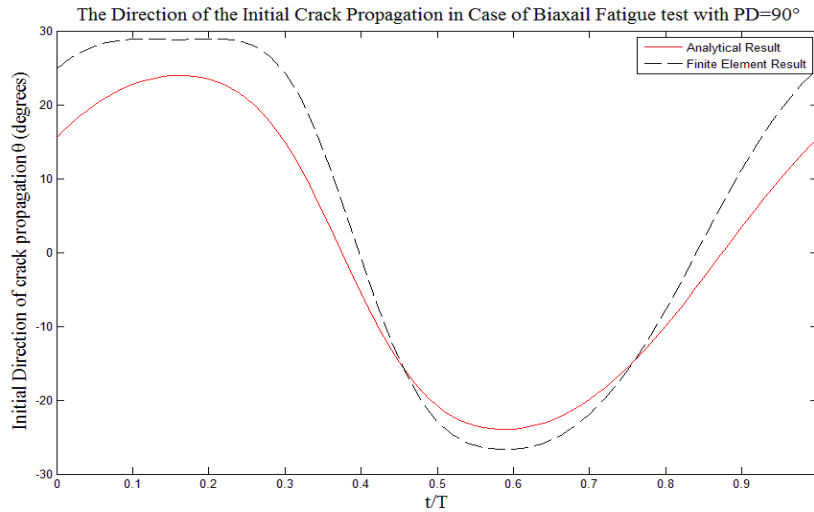


Figure 4.10: The direction of the initial crack path of an AA 7075-T6 biaxial specimen with phase difference=90° tested under cyclic load in air environment using analytical and finite element methods.

Figure 4.9.b also shows the angles of the initial paths of the two cracks observed experimentally which are +31° and -31°. The experimental result are very close to the predicted ones that have been determined analytically or using FEA, i.e. ±24° or ± 29°.

The two cracks did not split any further throughout the experiment. This can be explained by studying the plot of the direction of further crack propagation at the 5,001st cycle of fatigue loading, after the formation of the two cracks using equation (2.36) and values of the stress intensity factors obtained from the FEA, Figure 4.11. Because of the symmetry, only right or vertical crack has been focused on.

By looking at Figure 4.11, it is noticeable that the absolute value of the maximum angle of crack propagation is 29° , $|\theta_{max}| = 29^\circ$, and the absolute value of the minimum negative angle of crack propagation is 4° , $|\theta_{min}| = 4^\circ$, i.e. $|\theta_{max}|$ is very large as compared to $|\theta_{min}|$. This explains why further branching of the two cracks is not probable, i.e. why they keep propagating as shown in Figure 4.11. In the saltwater environment, the exact same result of the crack path was observed in the test.

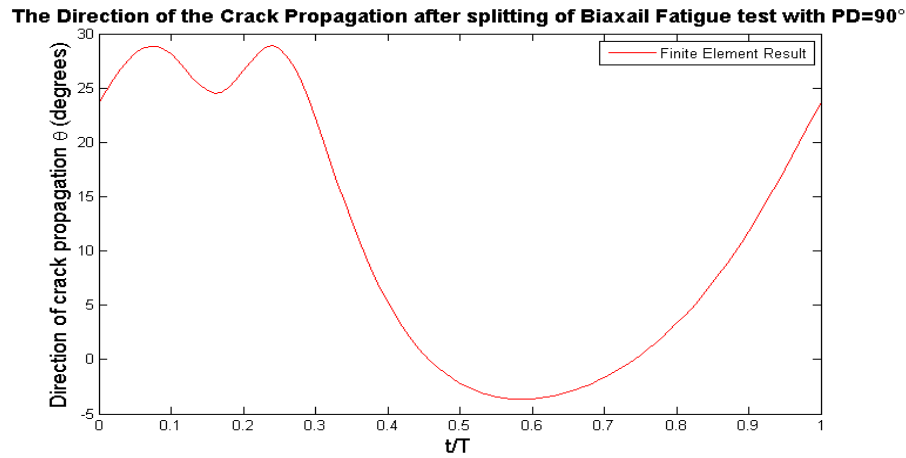


Figure 4.11: Variation of the right or vertical crack propagation angle, after bifurcation exists, under biaxial fatigue during one cycle with PD= 90° .

Figure 4.12 shows the strain energy release rate versus the number of cycles when the PD= 90° in air and saltwater environments, for both horizontal and vertical cracks. In air environment, the horizontal and the vertical cracks have the same strain energy release

rate with increasing the number of cycles. This explains why the horizontal and vertical cracks have the same length, since they have the same strain energy release rate. Also, in the saltwater environment, the strain energy release rates were the same with increasing the number of cycles for both cracks. So, the same results are there, as noticed from the experiment.

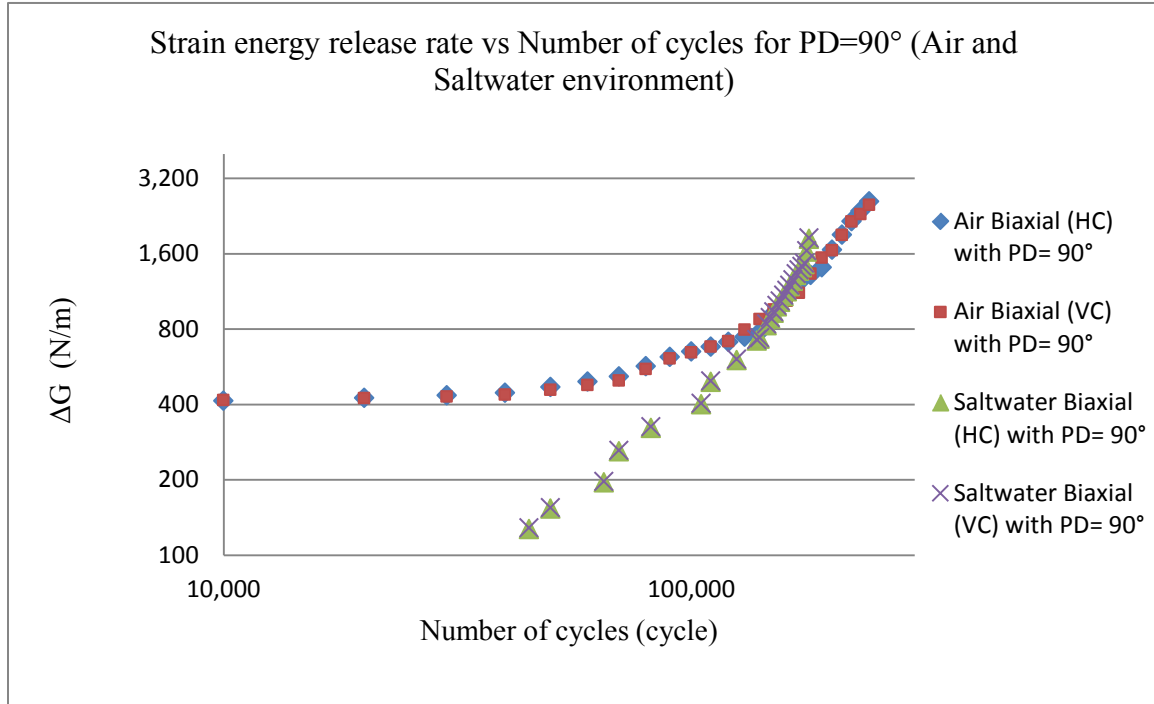


Figure 4.12: Strain energy release rate versus number of cycles when the phase difference is 90° in air and saltwater environments.

4.2.2.1 Crack Path of Biaxial Specimens with 180° Phase Difference in Air and Saltwater Environments

The loads in the Y-direction was applied, and after one-half of a cycle the other loads start to be applied, which makes a phase difference of 180°, Figure 4.13.a. The

result is two cracks, formed nearly symmetric with respect to the direction of the precrack and the notch as shown in Figures 4.13.b. These two cracks grew without any additional division.

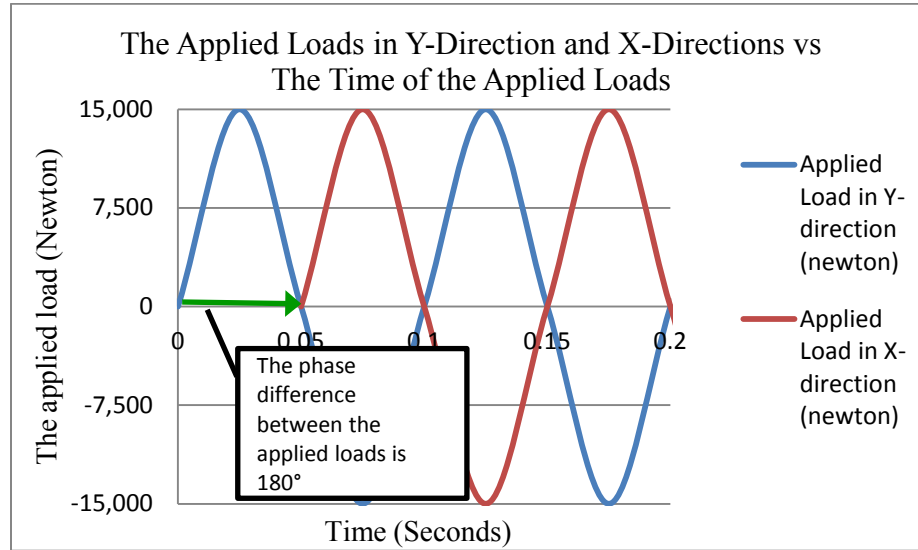


Figure 4.13.a: The applied loads of the Y-Direction and X-Directions versus the Time, when applying the loads in the Y-direction, and after one-half of a cycle the other loads start to be applied, which makes a phase difference of 180° .

Starting either the applied loads in the Y-direction, first, or X-direction, just swap the two formed symmetric cracks characteristics, which does not change the result, because the two formed cracks have the same lengths and angles from the precrack. Because of the previous reason, the analysis will be focused on the case of starting Y-direction applied load first.

For this case, the precrack split into two symmetric cracks as in the case when the phase difference was 90° , but with different initial angles than that in the 90° case, as will

be shown later in this section. These two split cracks grew without any further branching, Figure 4.13.b.

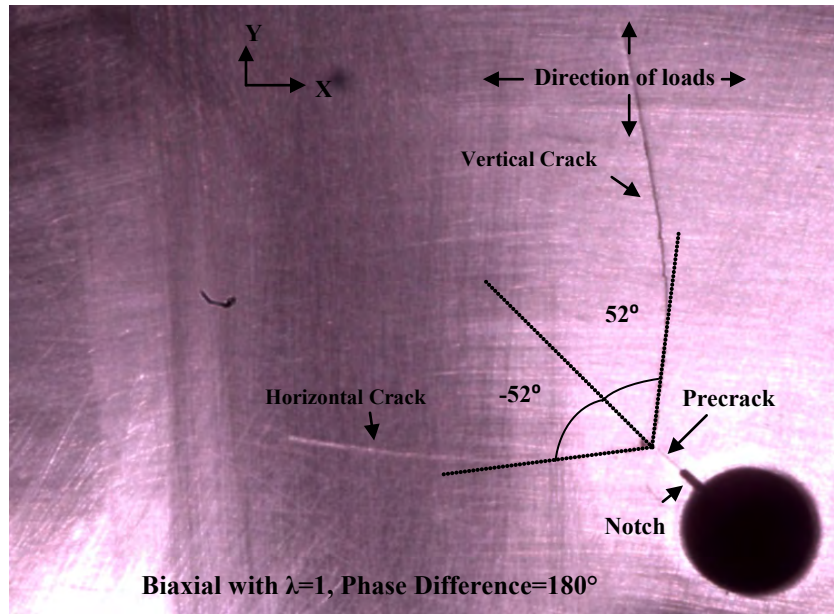


Figure 4.13.b: The direction of the crack path of an AA 7075-T6 biaxial specimen with PD=180° tested under cyclic load in air environment.

Similar to the previous cases, two solutions has been addressed to study this behavior of the splitting of the precrack into two symmetrical cracks under biaxial loads with PD=180°. These solutions are analytical solution, and Finite Element Approach (FEA). Figure 4.14 shows the angles of the initial crack path that each approach provides, and it was plotted before the crack split.

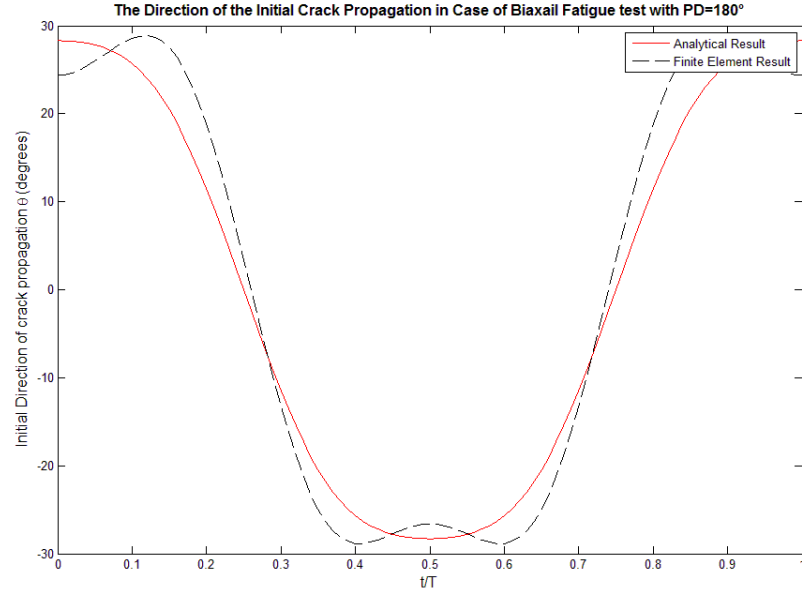


Figure 4.14: The direction of the initial crack path of an AA 7075-T6 biaxial specimen with phase difference= 180° tested under cyclic load in air environment using analytical and finite element methods.

Both the analytical and FEA curves granted that the maximum angle in one loading cycle is $+29^\circ$ and the minimum angle is -29° , Figure 4.14. On the other hand, the experimental method showed that the maximum angle is $+52^\circ$, and the minimum one is -52° , Figure 4.10. Despite the fact that experimental result showed different angles, the same conclusion could be stated, since both analytical and FEA agreed in calculating the initial angles of the crack propagation, it is very probable that the maximum and minimum angles initiated experimentally were $\pm 29^\circ$ initially, and then it changed suddenly to $\pm 52^\circ$. So, when the load is applied with $PD = 180^\circ$, one crack grows in the direction $+29^\circ$ with respect to the precrack path throughout the first half-cycle of loading. Likewise, the other crack grows in the direction of -29° during the second half-cycle load.

Thus, the chances of the precrack to split and grow symmetrically in the two directions are feasible, which was noticed experimentally, as in Figure 4.13.b.

As the previous cases, the cracks did not split any further after the first split, and by analyzing the plot of the instant directions of further crack propagation, after bifurcation exists, this can be confirmed, Figure 4.15. Because of the symmetry, only right or vertical crack has been focused on.

By looking at Figure 4.15, it is clear that the absolute value of the maximum angle of crack propagation is 52° , $|\theta_{max}| = 52^\circ$, and the absolute value of the minimum negative angle of crack propagation is 1° , $|\theta_{min}| = 1^\circ$, i.e. $|\theta_{max}|$ is very large as compared to $|\theta_{min}|$. This explains why further branching of the two cracks is not probable, i.e. why they keep propagating as shown in Figure 4.15. In the saltwater environment, the exact same result of the crack path was observed in the test.

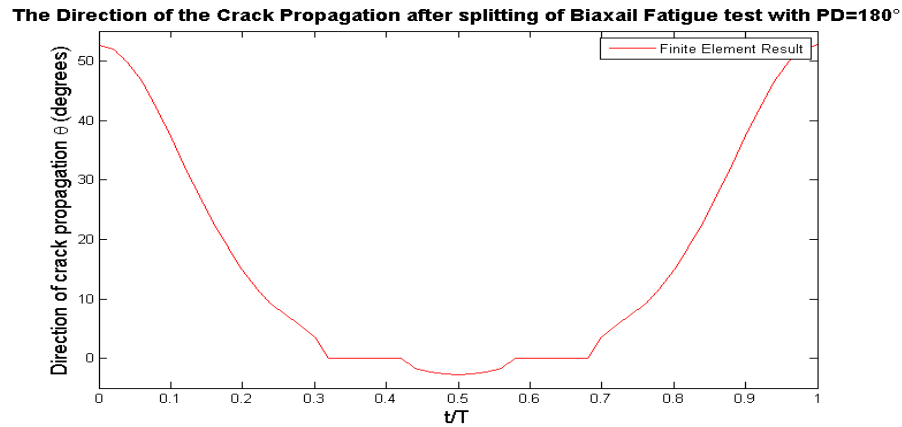


Figure 4.15: Variation of the right or vertical crack propagation angle, after bifurcation exists, under biaxial fatigue during one cycle with PD= 180° .

Figure 4.16 shows the strain energy release rate versus the number of cycles when the PD= 180° in air and saltwater environments, for both horizontal and vertical cracks.

In air environment, the horizontal and the vertical cracks have the same strain energy release rate with increasing the number of cycles. This explains why the horizontal crack and the vertical one have the same length, since they have the same strain energy release rate. Also, in the saltwater environment, the strain energy release rates were the same with increasing the number of cycles for both cracks. So, the same results are there, as noticed from the experiment.

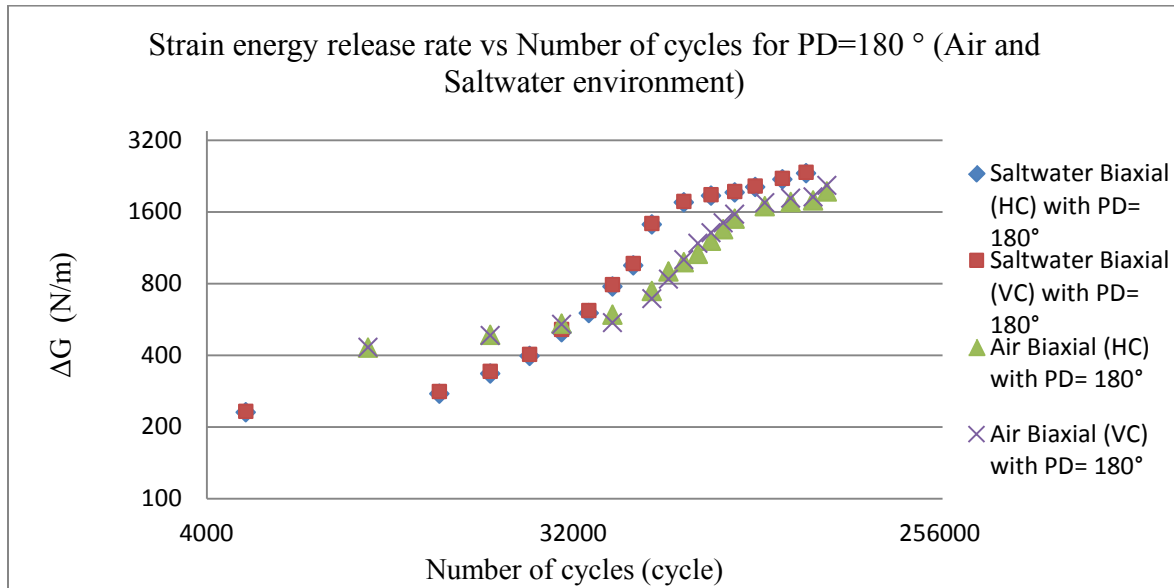


Figure 4.16: Strain energy release rate versus number of cycles when the phase difference is 180° in air and saltwater environments.

4.3 Crack Growth Rate

It is common to describe fatigue crack growth behavior by the relationship between crack growth rate (da/dN) and the crack driving force. Crack growth rates (da/dN) were computed from the relationship between the measured crack length and

number of cycles. After that, these were correlated with the crack driving forces to explain the fatigue crack growth behavior.

Mode I stress intensity factor range (ΔK_I) usually states the crack driving force, and that's when the crack is collinear to the precrack. On the other hand, when the crack is non collinear, both mode I (ΔK_I) and mode II (ΔK_{II}) are used to express the crack driving force. These two can be combined together to form the total strain energy release rate range (ΔG) using equation (3.1). Therefore, the total strain energy release rate range (ΔG) is a more appropriate parameter when comparing to the previous biaxial tests with different phases. Another reason for using (ΔG) over (ΔK) is that in the case of phase difference of 180° , (ΔK) = 0 which prevent comparing it to the other cases. Thus, (da/dN) versus (ΔG) will be used to represent the crack growth rate in this section.

4.3.1 Crack Growth Rate of Uniaxial and Biaxial Specimens without Phase

Difference in Air and Saltwater Environments

For sake of clarification and comparisons, the crack growth rate of uniaxial and biaxial specimens without phase difference in air and saltwater environments is discussed. As mentioned earlier in Figures 4.1 and 4.2, the crack path of uniaxial and biaxial Specimens, without phase difference, were straight and collinear to their precrack paths. So, only mode I crack driving forces, (K_I) are there. For that reason, (ΔK_I) factors were computed from the FEA to find out the total strain energy release rate range(ΔG).

Figure 4.17 shows the relationship between the crack growth rate (da/dN) and the strain energy release rate (ΔG) for uniaxial and biaxial tests with no phase difference ($PD=0^\circ$) in both air and saltwater environments. In the air environment, both uniaxial and biaxial, with $PD=0^\circ$, seem to have the same crack growth rate versus strain energy release rate curve. In other words, as (ΔG) increase, the (da/dN) increased too at the same rate for both cases. Similar behavior was observed in the saltwater environment, but this time the curves of crack growth rate versus strain energy release rate are higher, for both uniaxial and biaxial, with $PD=0^\circ$.

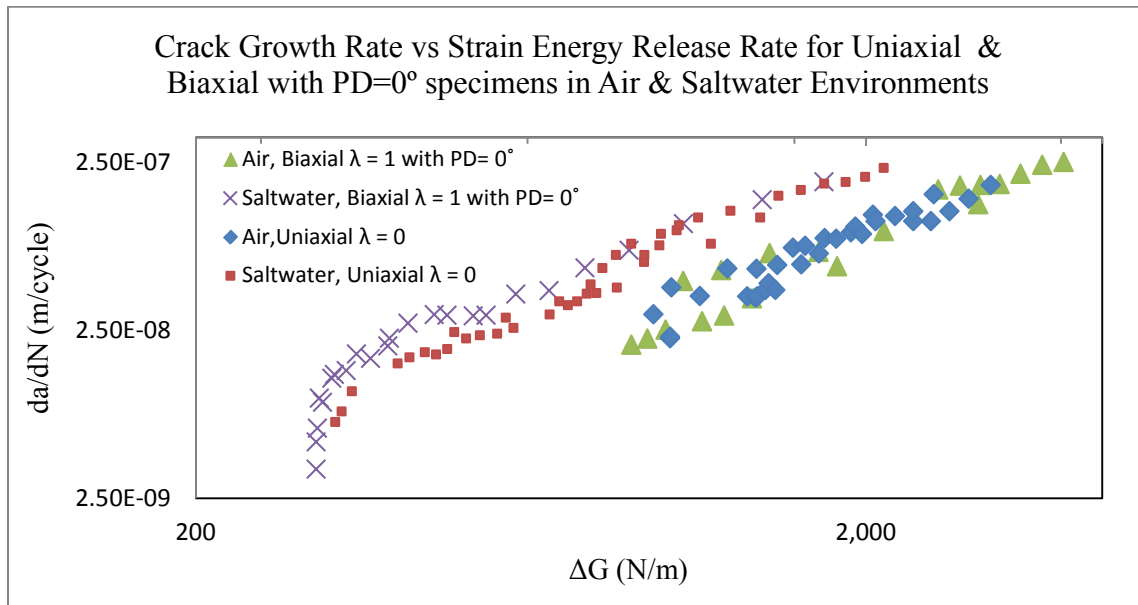


Figure 4.17 Crack growth rate versus strain energy release rate for uniaxial and biaxial with $PD=0^\circ$ specimens in air and saltwater environments

4.3.2 Crack Growth Rate of Biaxial Specimens with 45° Phase Difference in Air and Saltwater Environments

Figure 4.18 shows the crack length versus number of cycles for biaxial specimen with $PD=45^\circ$ in air and saltwater environments. In this case, the Y-direction loads applied, and after one-eighth of a cycle the other loads applied, which makes a phase difference of 45° . With that being explained, the result of the experiment in both environments will be next.

In the air environment, as the number of cycles (N) increased, the crack length (a) increased too for both right-vertical crack (VC) and left-horizontal crack (HC). Figure 4.18, also, showed that up to around 750,000 cycles both cracks had nearly the same (a) vs. (N) curve, and then the (HC) length increased rapidly at a higher rate while the (VC) length kept the same rate of increasing as before the 750,000 cycles. In the saltwater environment, same behavior was observed. (N) increases as (a) increase for both (HC) and (VC). Also, cracks' lengths were the same up to 120,000 cycles, then (HC) length increased quickly at a higher rate while the (VC) length kept the same rate of increasing as before the 120,000 cycles. Moreover, when comparing both (HC) and (VC) in the air environment to the saltwater ones, it was observed that the saltwater environment cracks were plotted to the left of the ones from the air environment, which means that both (HC) and (VC) needed much less amount of cycles to grow until failures.

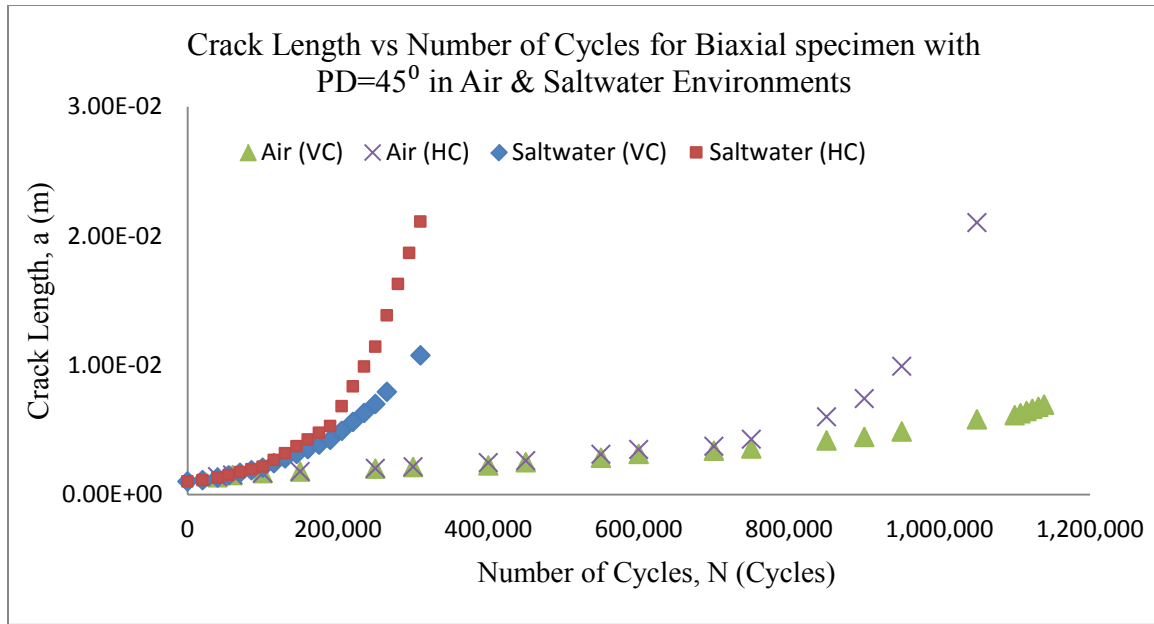


Figure 4.18: Crack length versus number of cycles for biaxial specimen with $PD=45^\circ$ in air and saltwater when the Y-direction loads applied, and after one-eighth of a cycle the other loads applied, which makes a phase difference of 45° .

Figure 4.19 shows the crack lengths versus the number of cycles for biaxial specimen with $PD=45^\circ$ in air & saltwater environments. This case was done by starting the X-direction applied loads, and after one-eighth of a cycle the other loads applied, which makes a phase difference of 45° . This case provided the exact same curves for the crack lengths versus the number of cycles as resulted in Figure 4.18, but with swapping the horizontal crack values with the vertical crack ones. Therefore, starting the test with Y-direction loads, first, or X-direction loads influence the result dramatically when the phase difference between the applied loads is 45° .

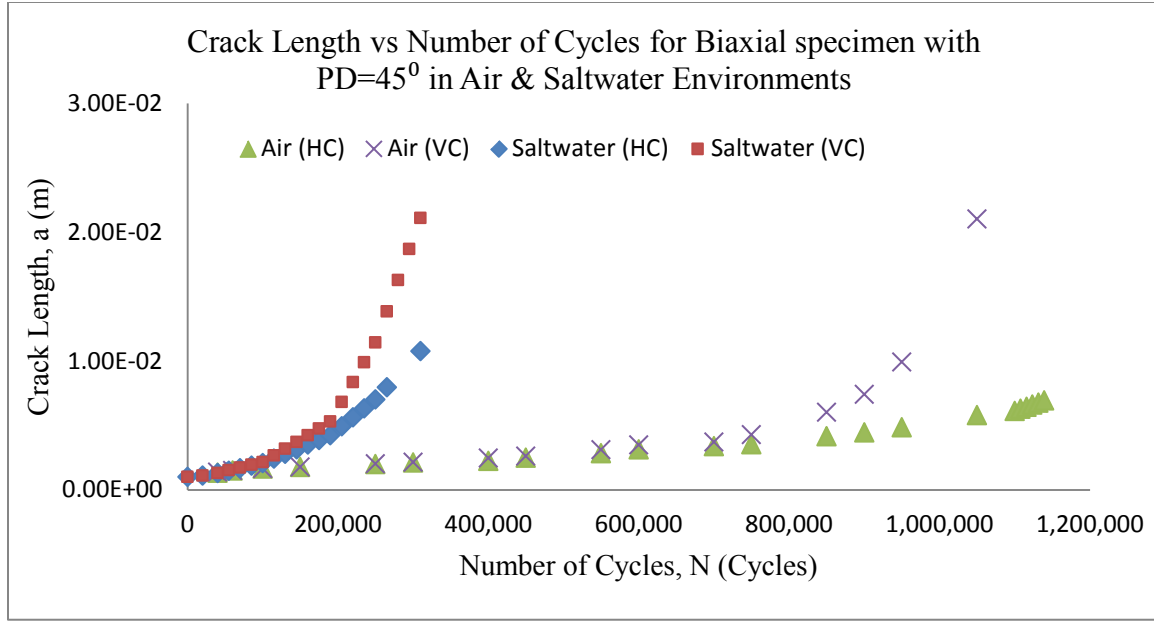


Figure 4.19: Crack length versus number of cycles for biaxial specimen with $PD=45^\circ$ in air and saltwater when the X-direction loads applied, and after one-eighth of a cycle the other loads applied, which makes a phase difference of 45° .

As mentioned earlier, the precrack split into two curved cracks. So, both mode I and II crack driving forces, (K_I) and (K_{II}) are there for both cracks. Thus, ranges of stress intensity factors, (ΔK_I) and (ΔK_{II}) , were calculated from the FEA to find out the total strain energy release rate range (ΔG) for each crack. After that, the crack growth rate (da/dN) plotted versus the calculated strain energy release rate (ΔG) for each crack and in both environments, i.e. air and saltwater.

Figure 4.20 shows the relationships between crack growth rates (da/dN) and strain energy release rate (ΔG) for both crack branches when the phase difference is 45° in air and saltwater environments. Figure 4.20 was plotted when the Y-direction loads applied, and after one-eighth of a cycle the other loads applied. In the air environment, the

relationship between crack growth rate (da/dN) and strain energy release rate (ΔG) for both vertical crack (VC) and horizontal crack (HC) when the phase difference 45° is almost identical up to 360 (N/m) , where the crack growth rate for the horizontal crack (HC) start to grow at a higher rate while the vertical crack growth rate follow the same rate of increasing as from the beginning of the experiment. In the saltwater environment, similar result achieved but the increase in the horizontal crack growth rate start earlier, at 480 (N/m) . Also, it was observed that the (da/dN) are higher in the saltwater comparing to the air environment one, which means that corrosion accelerates the crack growth rate for both (HC) and (VC).

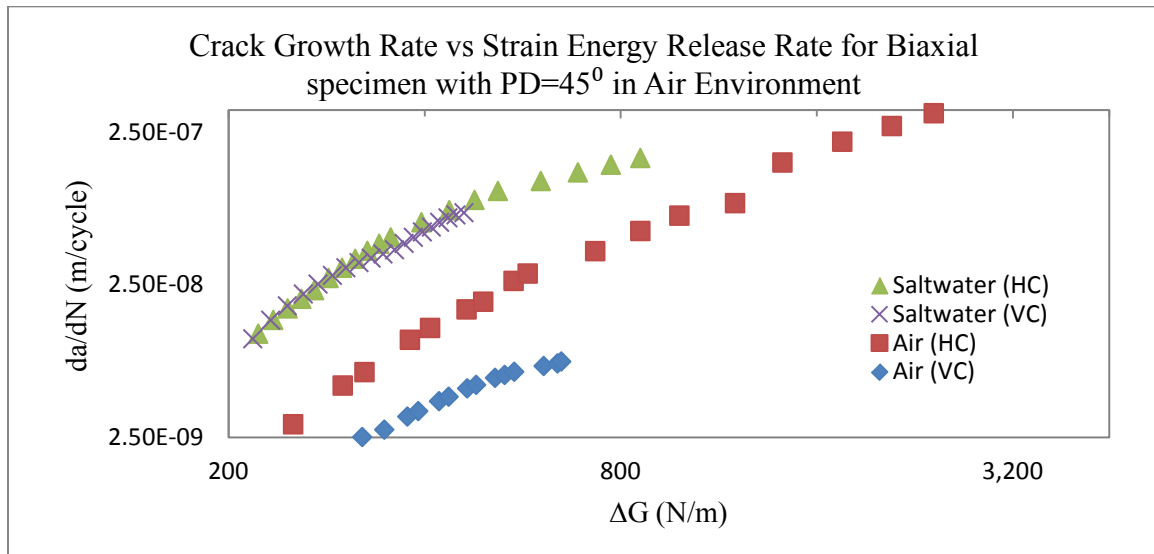


Figure 4.20: The relationships between crack growth rate (da/dN) and strain energy release rate (ΔG) for both crack branches when the Y-direction loads applied, and after one-eighth of a cycle the other loads applied, which makes a phase difference of 45° , in both air and saltwater environments.

Figure 4.21 shows the relationships between the average crack growth rates (da/dN) and the total strain energy release rate (ΔG) for both horizontal and vertical cracks when the phase difference is 45° in air and saltwater environments. Because the vertical crack has a different crack growth rate (da/dN) than the horizontal one, the crack growth rate (da/dN) will be shown as an average crack growth rate of the two cracks (avg. da/dN), in order to compare it later with the cases when the phase difference are 90° , and 180° . In addition to that, since two cracks are there, the strain energy release rate will be the sum of both strain energy release rate for both cracks.

Figure 4.21 shows that as the sum of the strain energy release rate for both cracks increased, the average crack growth rate increased too. The same curve shape in the saltwater environment has been drawn, but the curve is higher, which indicates that the corrosion accelerate the average crack growth rate compared to the same experiment in air environment.

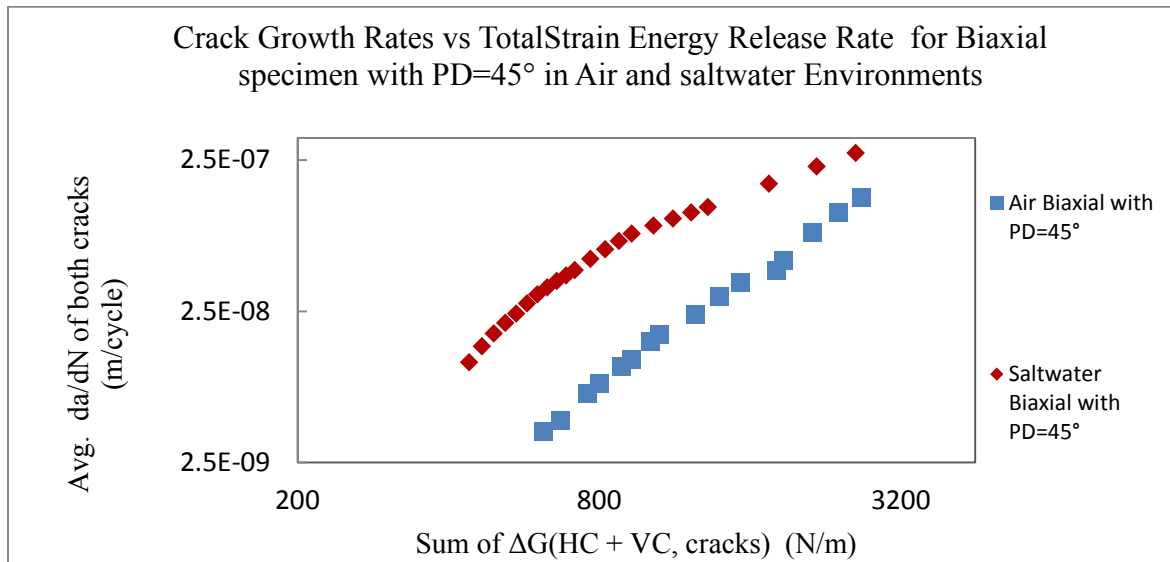


Figure 4.21: The relationships between the average crack growths rate (Avg. (da/dN)) and the sum of the strain energy release rate (Sum of (ΔG)) for both horizontal and vertical cracks when the phase difference is 45° in air and saltwater environments.

4.3.3 Crack Growth Rate of Biaxial Specimens with 90° Phase Difference in Air and Saltwater Environments

The relationship between the crack length and the number of cycles for the biaxial case, when the Y-direction or X-direction loads applied and after one-fourth of a cycle the other loads start to be applied, provides the same result in air environments, Figure 4.22. The Figure shows that as the number of cycles increased, cracks' lengths increased too. Also, since the lengths of the horizontal and vertical cracks are about the same, therefore starting the test with applying Y-direction loads, first, or X-direction loads does not change the result, because it just swap the horizontal crack characteristics with the vertical ones. In the saltwater environment, the same result was observed, but the curves of the crack length versus number of cycles are shifted to the left comparing to those from the air experiment, which means that the cracks needed less number of cycles to grow until failures in the saltwater atmosphere.

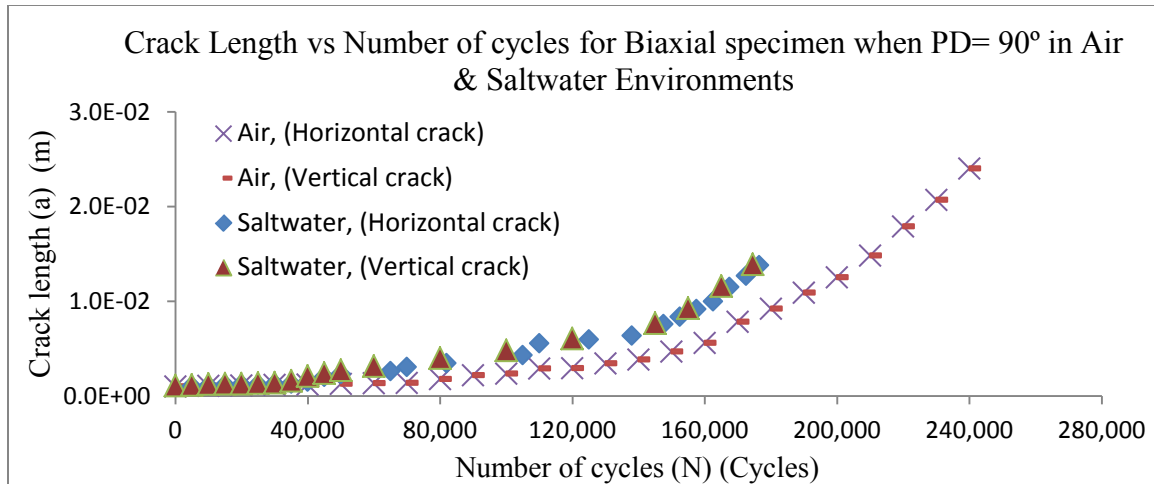


Figure 4.22: Crack length versus number of cycles for biaxial specimen with $PD=90^\circ$ in air and saltwater.

Figure 4.23 shows the relationships between crack growth rates (da/dN) and strain energy release rate (ΔG) for both crack branches when the phase difference is 90° in air and saltwater environments. Figure 4.23 was plotted when the Y-direction loads applied, and after one-fourth of a cycle the other loads start to be applied, which makes a phase difference of 90° . In the air environment, the relationship between crack growth rate (da/dN) and strain energy release rate (ΔG) for both vertical crack (VC) and horizontal crack (HC) was almost identical up to the failure of the specimen. In the saltwater environment, similar result was observed as in the air environment. Also, it was observed that the (da/dN) curve was higher in the saltwater comparing to the air environment, which indicates that corrosion accelerates the crack growth rate for both (HC) and (VC).

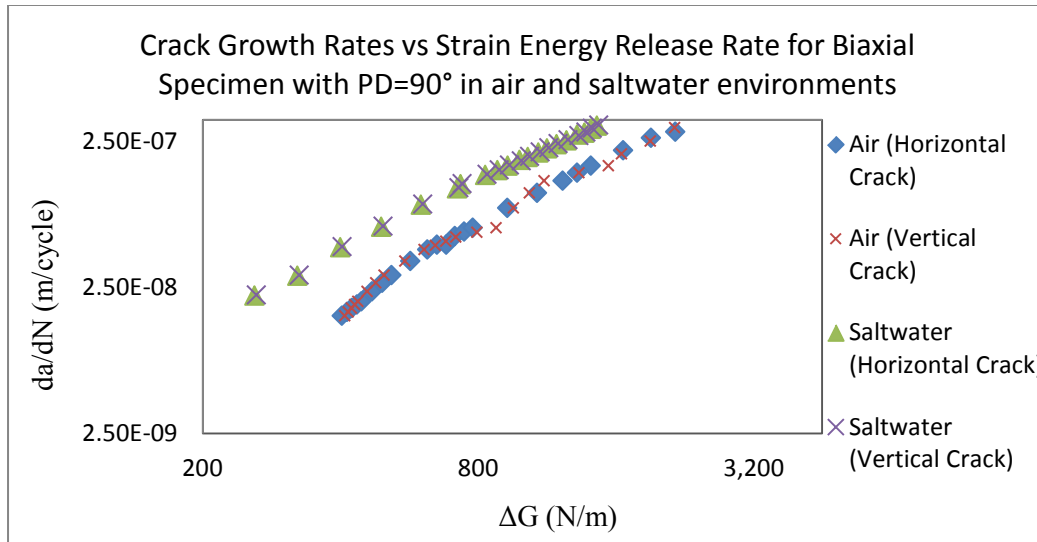


Figure 4.23: The relationships between crack growth rate (da/dN) and strain energy release rate (ΔG) for both crack branches when the Y-direction loads applied, and after phase difference between the applied loads of 90° , the loads in the X-direction start to be applied, in both air and saltwater environments.

Figure 4.24 shows the relationships between crack growth rates (da/dN) and strain energy release rate (ΔG) for both horizontal and vertical cracks when the phase difference was 90° in air and saltwater environments. Since both horizontal and vertical cracks have the same length, the crack growth rate (da/dN) will be shown as an average crack growth rate of the two cracks, in order to compare it later with the cases when the $PD=45^\circ$. In addition to that, since two cracks are there, the strain energy release rate will be the sum of both strain energy release rate for both cracks. Now, for the air environment, it is exciting that the relationship between the average crack growth rate (Avg. (da/dN)) and the sum of the strain energy release rate (sum of ΔG) for both vertical crack (VC) and horizontal crack (HC) when the phase difference 90° is almost identical all the way up to

the failure point. Also, Figure 4.24 shows that as the sum of the strain energy release rate for both cracks increased, the average crack growth rate increased too. The same curve shape in the saltwater environment has been drawn, but the curve is higher, which indicates that the corrosion accelerate the average crack growth rate compared to the same experiment in the air atmosphere.

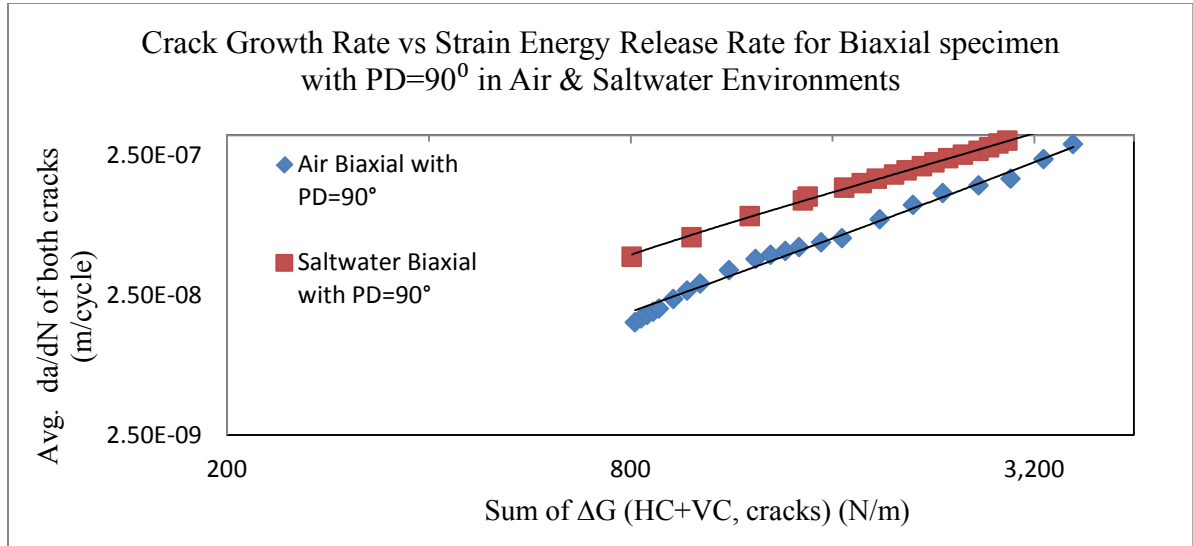


Figure 4.24: The relationships between the average crack growths rate (da/dN) and the sum of the strain energy release rate (ΔG) for both horizontal and vertical cracks when the phase difference is 90° in air and saltwater environments.

4.3.2 Crack Growth Rate of Biaxial Specimens with 180° Phase Difference in Air and Saltwater Environments

Figure 4.25 demonstrates the relationship between the cracks' lengths and the number of cycles for biaxial specimens when the Y-direction loads applied, and after one-half of a cycle the other loads applied, which makes a phase difference of 180°. As

illustrated before, if the lengths of the horizontal and vertical cracks are the same, starting the test with applying Y-direction loads, first, or X-direction loads does not change the result, because it just swap the horizontal crack characteristics with the vertical ones. As expected, the experiment showed an increase in the cracks' lengths as the number of cycles increased. The same curves resulted from the test in the saltwater environment. Those curves were drawn to the left comparing to those from the air experiment, which indicated that the cracks, generated in the saltwater environment, required much less number of cycles to failure.

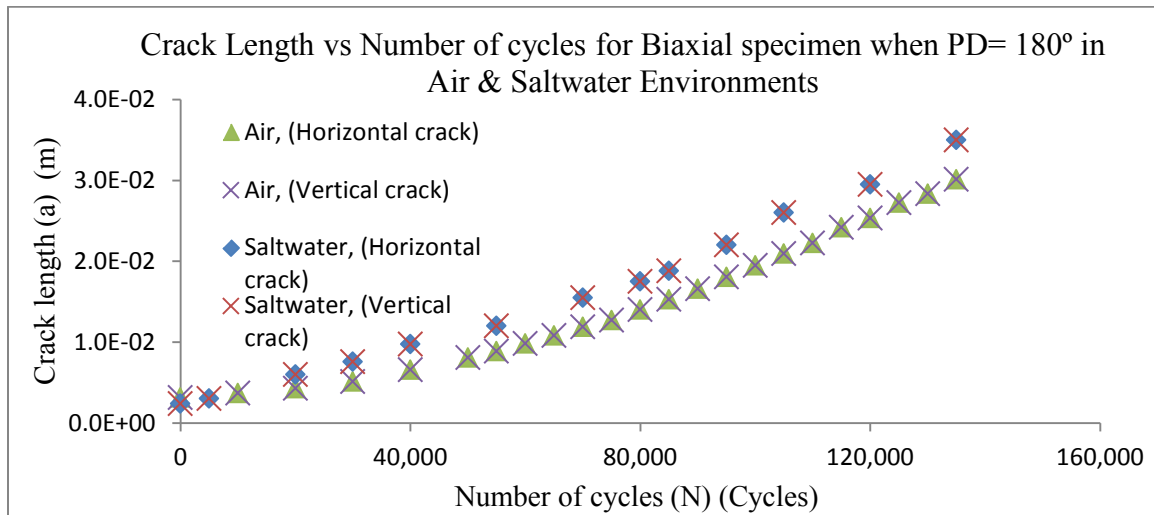


Figure 4.25: Crack length versus number of cycles for biaxial specimen with PD=180° in air and saltwater.

Figure 4.26 shows the relationships between crack growth rates (da/dN) and strain energy release rate (ΔG) for both crack branches when the phase difference was 180° in air and saltwater environments. Figure 4.26 was plotted when the Y-direction loads applied, and after one-half of a cycle the other loads applied, which makes a phase difference of 180°. In the air environment, the relationship between crack growth rate

(da/dN) and strain energy release rate (ΔG) for both vertical crack (VC) and horizontal crack (HC) was almost identical up to failure of the specimen. In the saltwater environment, similar result was observed as in the air environment. Also, it was observed that the (da/dN) curve was higher in the saltwater comparing to the air environment, which means that corrosion accelerates the crack growth rate for both (HC) and (VC).

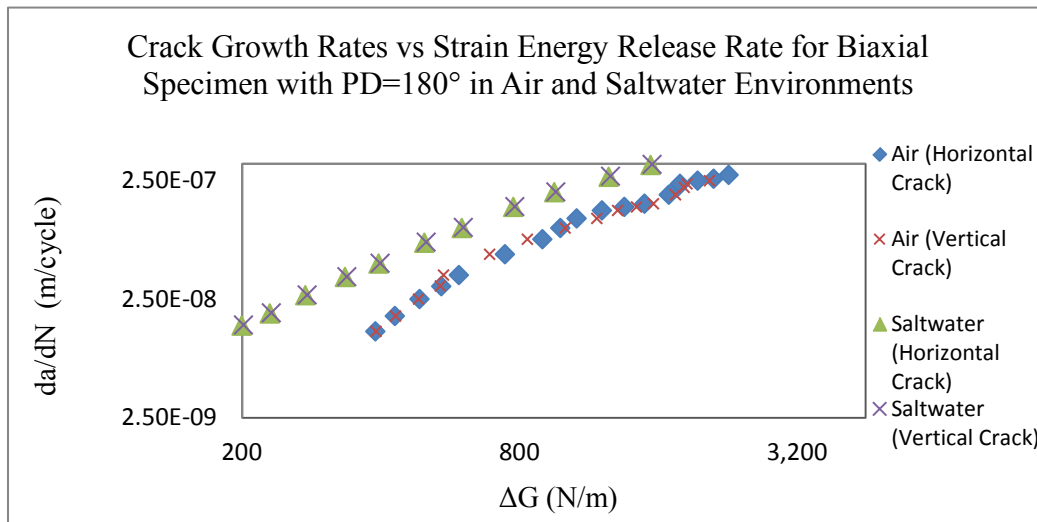


Figure 4.26: The relationships between crack growth rate (da/dN) and strain energy release rate (ΔG) for both crack branches when the Y-direction loads applied, and after one-half of a cycle the other loads applied, in both air and saltwater environments.

The relationships between average crack growth rates (Avg. (da/dN)) and sum of the strain energy release rate (Sum of (ΔG)) for both horizontal and vertical cracks, when the phase difference was 180° , in air and saltwater environments are illustrated in Figure 4.27. For the air environment, the curve of the average crack growth rate (Avg. (da/dN)) versus the sum of the strain energy release rate (sum of ΔG) for both cracks is almost indistinguishable all the way up to the failure of the specimen. Moreover, Figure 4.27

shows that as the sum of the strain energy release rate for both cracks increased, the average crack growth rate increased too. As expected, the tests in the saltwater environment gave the exact same result, but with accelerating the average crack growth rate compared to the same experiment in air atmosphere, Figure 4.27.

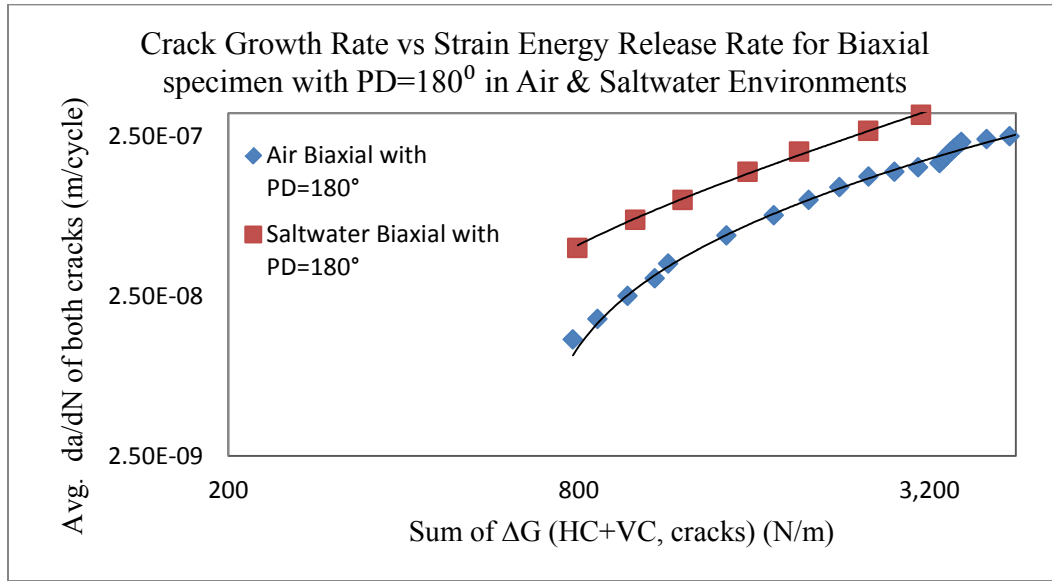


Figure 4.27: The relationships between the average crack growths rate (da/dN) and the sum of the strain energy release rate (ΔG) for both horizontal and vertical cracks when the phase difference is 180° in air and saltwater environments.

4.3.2 Crack Growth Rate of All Specimens with and without Phase Difference in Air and Saltwater Environments

Now, for sake of clarification and comparison, all of the previous tests will be gathered together in couple of figures to give a closer look to the influence of changing the phase difference on the crack growth rate versus the strain energy release rate. Figure 4.28 illustrates the crack growth rates (da/dN) versus the strain energy release rate (ΔG) for horizontal and vertical cracks in case of split (i.e. under biaxial fatigue with phase

differences of 45° , 90° and 180°) and the crack in case of non-split (i.e. under biaxial fatigue with 0° phase difference and the uniaxial fatigue test). This sums up all cases in air environment. In Figure 4.28, and for each case, the Y-direction loads applied, and after one-eighth, one-fourth, or one-half of a cycle, depending on the required phase difference, the other loads applied. Figure 4.28 shows that the curves of (da/dN) versus (ΔG) of the horizontal and vertical split cracks (i.e. tests with 45° , 90° and 180° phase differences) are higher comparing to those of non-split cracks generated from biaxial fatigue test with 0° phase difference or from the uniaxial fatigue test, except that for the case of the vertical crack when $PD=45^\circ$. The (da/dN) versus (ΔG) for the case of the vertical crack when $PD=45^\circ$ was plotted below all the other cases. This means that at a given crack growth rate the horizontal and vertical split cracks grew faster and required less amount of energy to grow than those under uniaxial test, biaxial test with $PD=0^\circ$, and the vertical crack in biaxial test with $PD=45^\circ$. Also, it is interesting to see that the vertical crack, which generated under biaxial fatigue load with $PD=45^\circ$, did not grow as when the phase difference is 90° or 180° . In case of $PD=45^\circ$, the curve of (da/dN) versus (ΔG) for the vertical split crack grow very slow and at lower rate of growth comparing to all cases including the uniaxial one.

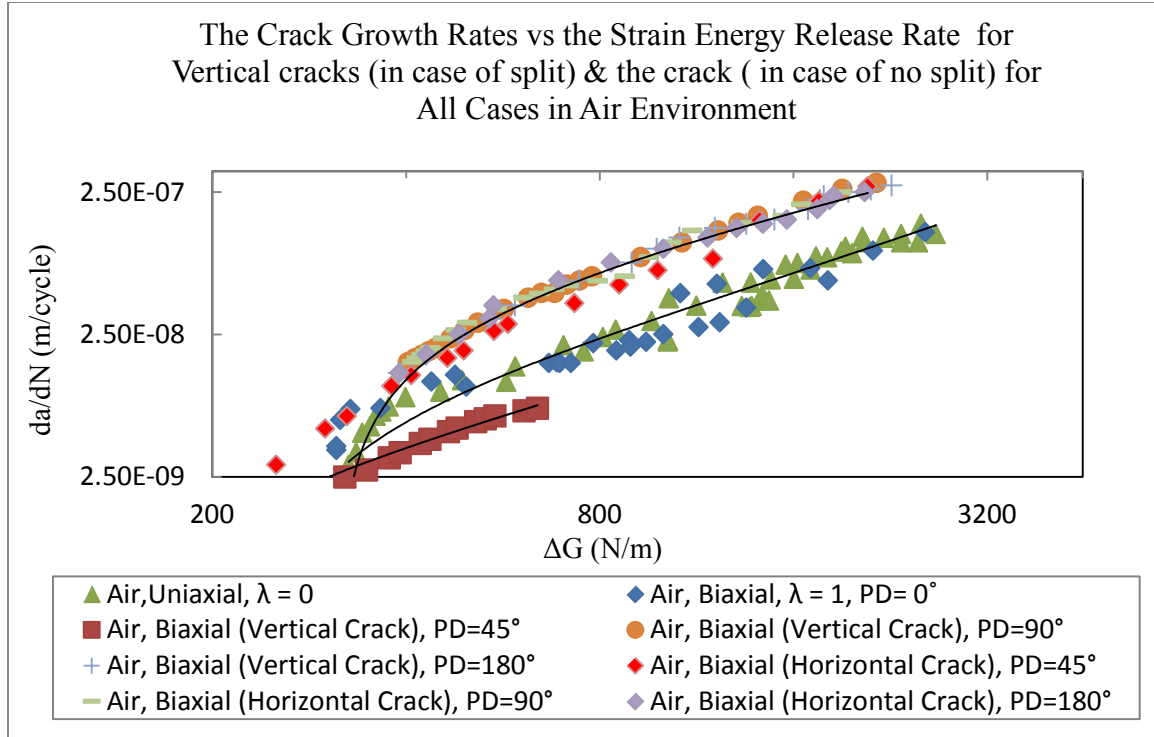


Figure 4.28: The crack growth rates versus the strain energy release rate for horizontal and vertical cracks (in case of split) and the crack (in case of no split) for all cases in air environment.

Figure 4.29 demonstrates the same comparisons as in Figure 4.28, but in saltwater environments. It shows that the curves of (da/dN) versus (ΔG) for the horizontal and vertical split cracks (i.e. tests with PD=45°, PD=90° and PD=180°) are higher than that from the non-split cracks, generated from biaxial fatigue test with PD=0° or from the uniaxial fatigue test. This means that at a given crack growth rate the horizontal and vertical split cracks grew faster and required less amount of energy to grow than those under uniaxial test, and biaxial test with PD=0°. Also, the vertical split crack in case of PD=45° influenced by the saltwater environment, which leads to an increase to its crack growth rate comparing to that in the air environment.

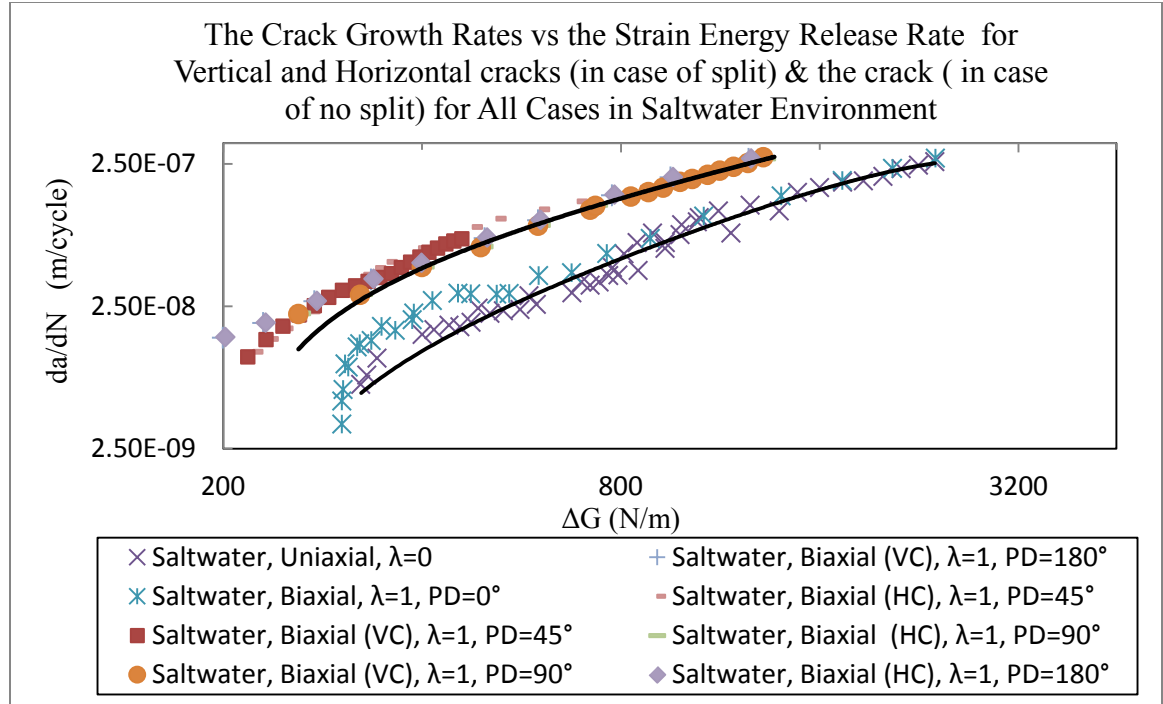


Figure 4.29: The crack growth rates versus the strain energy release rate for horizontal and vertical cracks (in case of split) and the crack (in case of no split) for all cases in saltwater environment.

Finally, in the air environment, the average of the crack growth rates of the two split cracks for each phase difference are calculated and then plotted versus the sum of the strain energy release rates (ΔG) of the two split cracks at each phase difference (i.e. 45°, 90° and 180°) and the strain energy release rates in case of tests with non-split cracks (i.e. biaxial test with 0° phase difference and the uniaxial fatigue test), Figure 4.30. The reason of this step is to evaluate the affect of changing the phase difference on the specimen and compare it to the non-split cracks results. The evaluation proves that these relationships are close to each other. Moreover at a given crack growth rate, it verifies

that the strain energy release rate of the non-split crack is equivalent to the sum of strain energy release rates of the two split cracks. In saltwater environment, the same plot has been drawn and the result is a similar curve, but higher, which indicates that corrosion played its role in accelerating the crack growth rates.

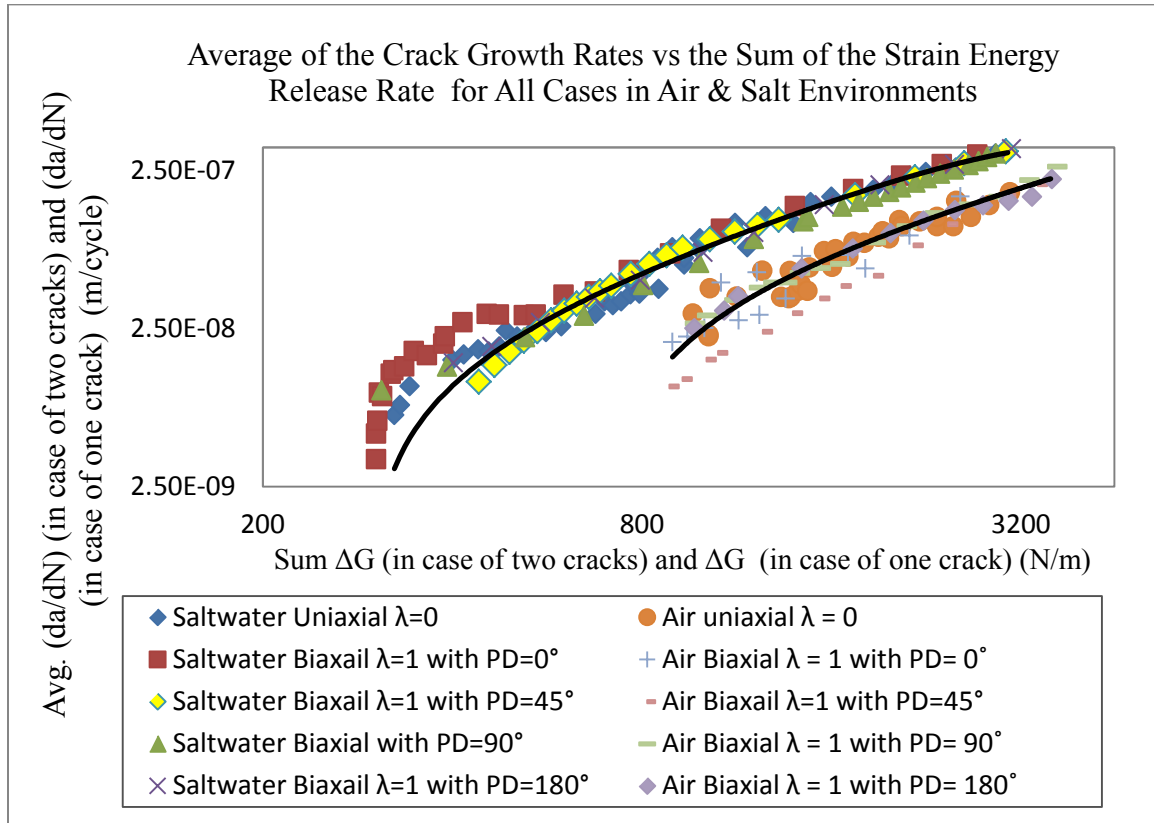


Figure 4.30: Average of the crack growth rates (in case of two cracks) and the crack growth rates (in case of one crack) versus the sum of the strain energy release rate (in case of two cracks) and the strain energy release rate (in case of one crack) for all cases in air and saltwater environments.

V. Conclusions and Recommendations

5.1 Conclusions

The present research studied the fatigue crack growth behavior of cruciform specimens made of 7075-T6 aluminum alloy under in-plane biaxial loading in air and saltwater (3.5% NaCl) environments with 45°, 90° and 180° phase difference between the two biaxial loads. The biaxility ratio was unity and the stress ratio was 0.5. A hole had been cut at the center of the specimens and then notched at a 45° angle from the two arms. Later, this notch was precracked for 1 mm, and then the experiment was executed. The results of this study were compared to an in-phase condition to study the effect of the phase difference on crack growth rate. After that, fracture mechanics was used to analyze the results. This research presents and documents the details of these experiments which can be helpful in understanding the concept of corrosion fatigue and overcome this mode of failure in the real applications. The following conclusion can be drawn from this study:

1. In case of biaxial fatigue with no phase difference and uniaxial fatigue, a single crack propagates collinear with the precrack and notch.
2. For biaxial fatigue with 90° or 180° phase difference, the single precrack splits into almost two symmetrical cracks that grow at almost the same rate of growth. The paths of the two split cracks diverge sharply at the beginning of the split and then they change their directions slowly as the test proceeds. Not to forget that at a certain number of fatigue cycles the lengths of both split cracks are almost equal. What's more, these two split cracks grow with no additional split.

For this case, the loads in the Y-direction was applied, and after one-half of a cycle the other loads start to be applied, which makes a phase difference of 180° . In addition, starting either the applied loads in the Y-direction, first, or X-direction, just swap the two formed symmetric cracks characteristics, which does not change the result, because the two formed cracks have the same lengths and angles from the precrack.

3. For biaxial fatigue with 45° phase difference, the precrack splits into two clearly unsymmetrical cracks that grow at different rate of growth. A long and a short crack were generated under this condition depending on which loads applied first i.e. Y-direction loads or X-direction loads.

The following points will provide explanations for this type of phase shift, and Figure 4.4.a and Figure 4.5.a help visualizing them:

- a. If the Y-direction loads applied first to the specimen and after one-eighth of a cycle the X-direction loads applied, which makes a phase difference of 45° , then the vertical crack created under this condition is short and the horizontal crack is way longer than the vertical one.
- b. On the other hand, if the X-direction loads applied first to the specimen and after one-eighth of a cycle the Y-direction loads applied, which makes a phase difference of 45° , then the vertical crack created under this condition is long and the horizontal crack is way shorter than the vertical one.

The longer crack have taken a path similar in its way of growing to the other biaxial fatigue cracks under 90° or 180° , while the shorter one have taken a completely different approach in its way of developing. Further, these two split cracks grow with no additional split.

4. For the 45° of phase difference, and in case of applying the loads in the Y-direction first, the longer crack grows horizontally. Therefore, the curves of crack growth rate (da/dN) versus the strain energy release rate (ΔG) of the horizontal split cracks (i.e. tests with 45° , 90° and 180° phase differences) grew faster and required less amount of energy to develop comparing to those non-split cracks generated from biaxial fatigue test with 0° phase difference or from the uniaxial fatigue test, Figure 4.28.

The crack growth rates (da/dN) versus the strain energy release rate (ΔG) for the vertical cracks in case of split and the crack in case of non-split in air environment shows same exact results as for the horizontal cracks, except for the vertical crack that grew under biaxial fatigue test with 45° of phase difference. The curve of (da/dN) versus (ΔG) of the vertical split crack grew very slow and at lower rate of growth comparing to all cases including the uniaxial one, Figure 4.28.

5. The relationships of the average of the crack growth rates (Avg. (da/dN)) of the two split cracks for each phase difference versus the sum of the strain energy release rates (Sum of (ΔG)) of the two split cracks at each phase difference (i.e. 45° , 90° and 180°) are almost the same as the curves for the

crack growth rates versus the strain energy release rates for the biaxial case without phase difference and the uniaxial case. In addition, at a given Average of crack growth rates, the strain energy release rate of the non-split crack is equivalent to the sum of strain energy release rates of the two split cracks. In saltwater environment, similar results were determined, but the curves were higher than that in the air environment, which points out that corrosion played its role in accelerating the crack growth rate.

5.2 Recommendations

Due to the variability that is inherent in materials testing, further testing on the fatigue crack growth from cracks originating from a circular hole in air and saltwater environment in AA 7075-T6 should be conducted. There are a wide range of test variables that could be altered that would also provide useful information with regard to the fatigue life of aluminum alloys with flaws. Also, further analysis could be done for the case of the phase difference of 45° , to find out why the strain energy release rate for horizontal crack is more than that for the vertical one, which leads to a long horizontal crack and a short vertical one, i.e. when the Y-direction loads applied first.

Appendix A: Finite Element Approach (FEA)

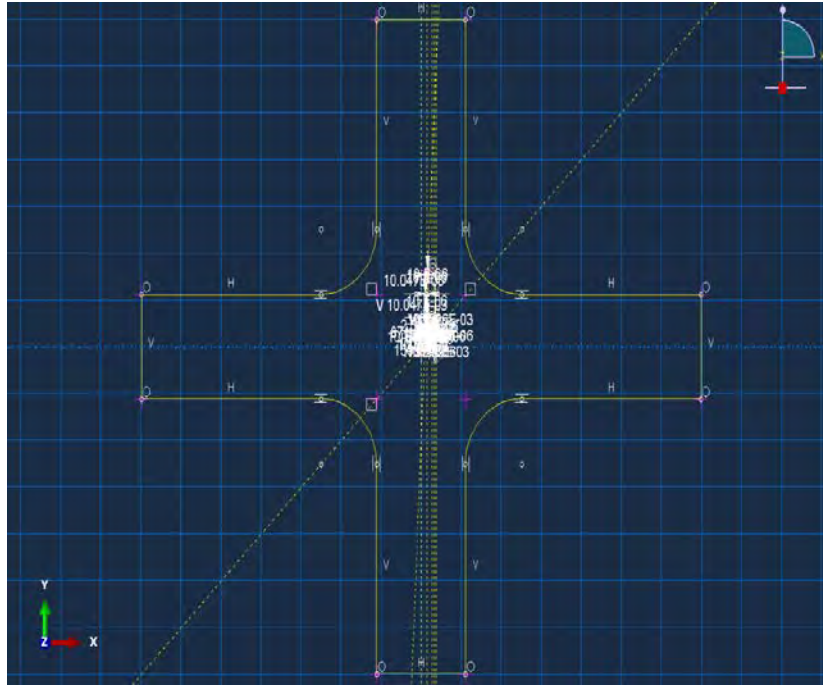


Figure A.1: Sketch of the Whole Specimen in Abaqus Program.

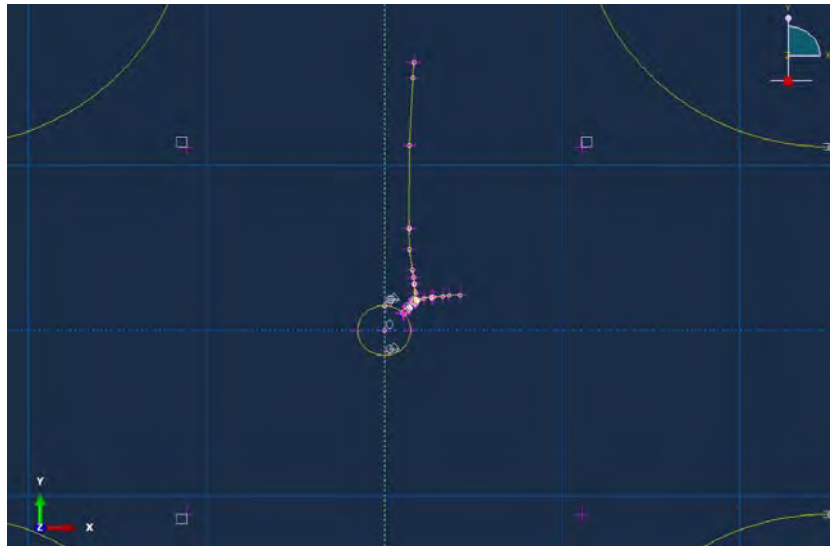


Figure A.2: Sketch of the Hole, Notch, Precrack and the Two Cracks in one of the Specimens in Abaqus Program.

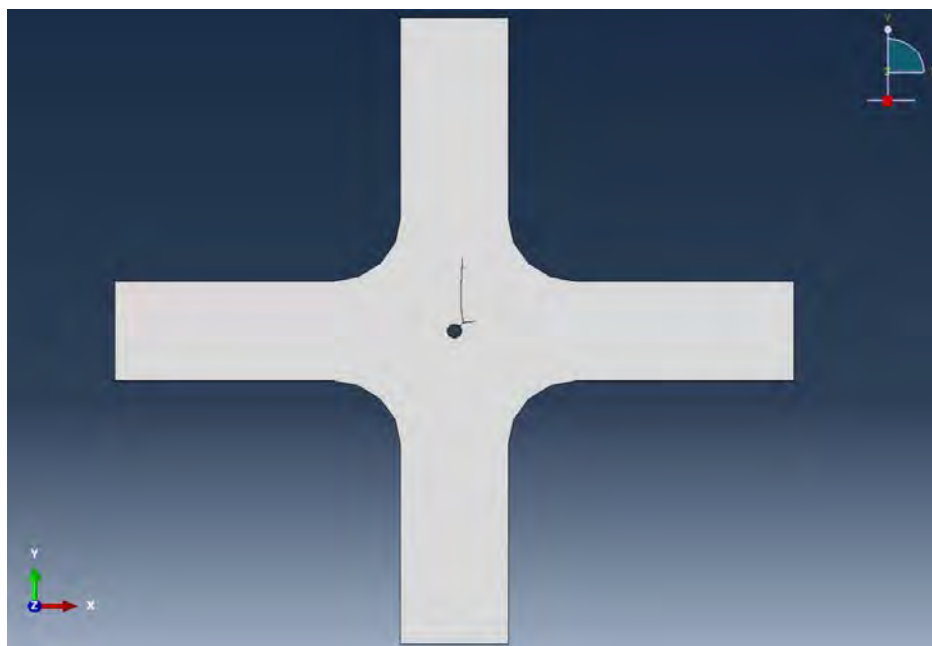


Figure A.3: The Whole Part of the Specimen in Abaqus Program Including the Cracks.

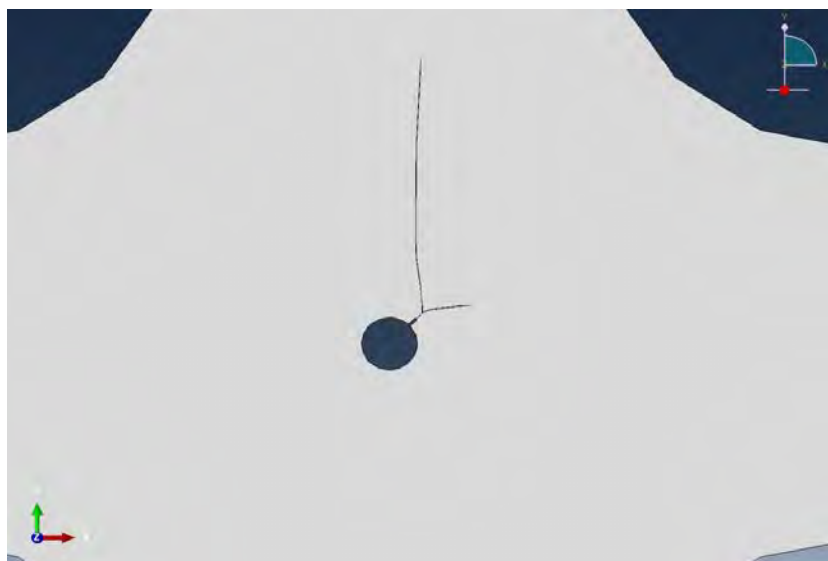


Figure A.4: A Closer Look to the Hole, Notch, Precrack and the Two Cracks in one of the Specimens in Abaqus Program.

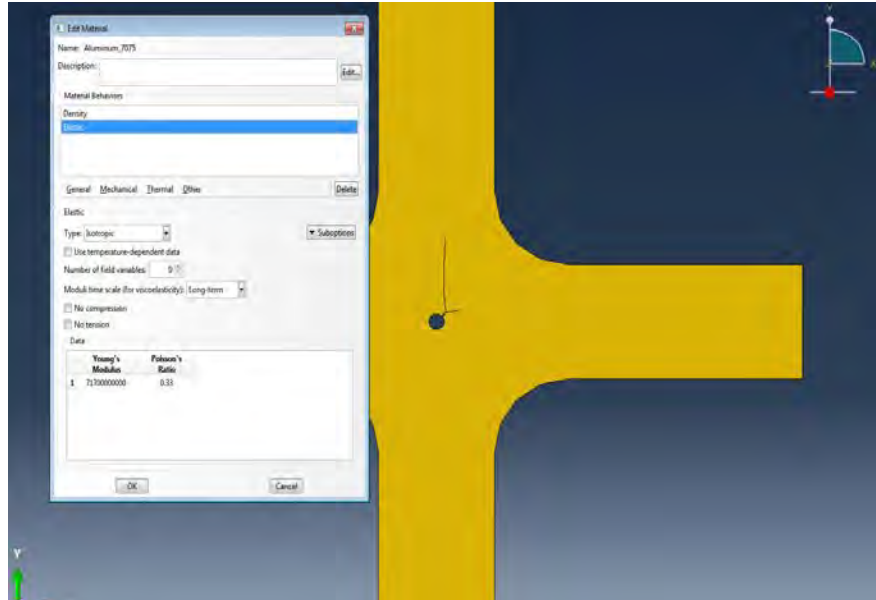


Figure A.5: Assigning the Material Type which is Aluminum Alloy 7075-T6 to the Specimen.

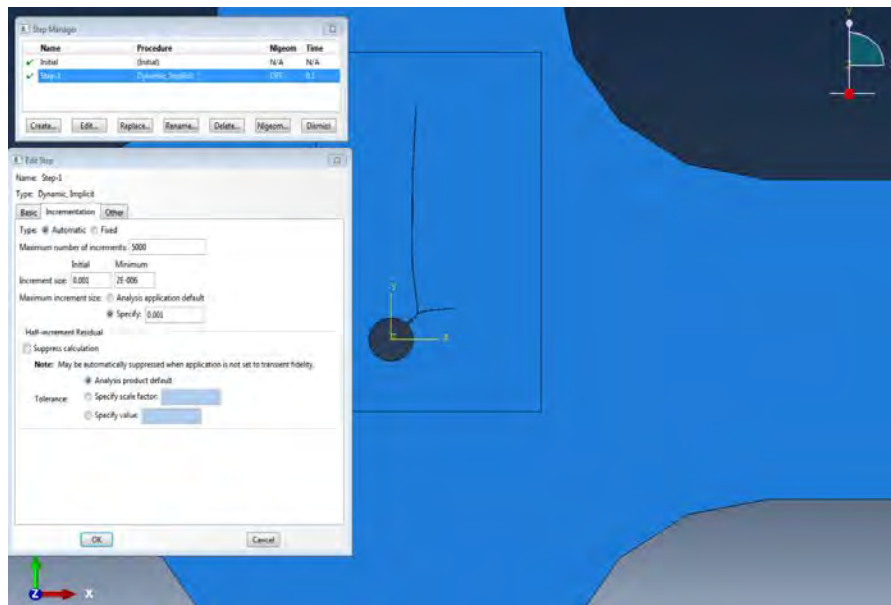


Figure A.6: Creating the Step or in Other Words How Many Cycles of Loads Need to Be There in Order to Find the ΔK s, ΔG s and the Cracks' Directions.

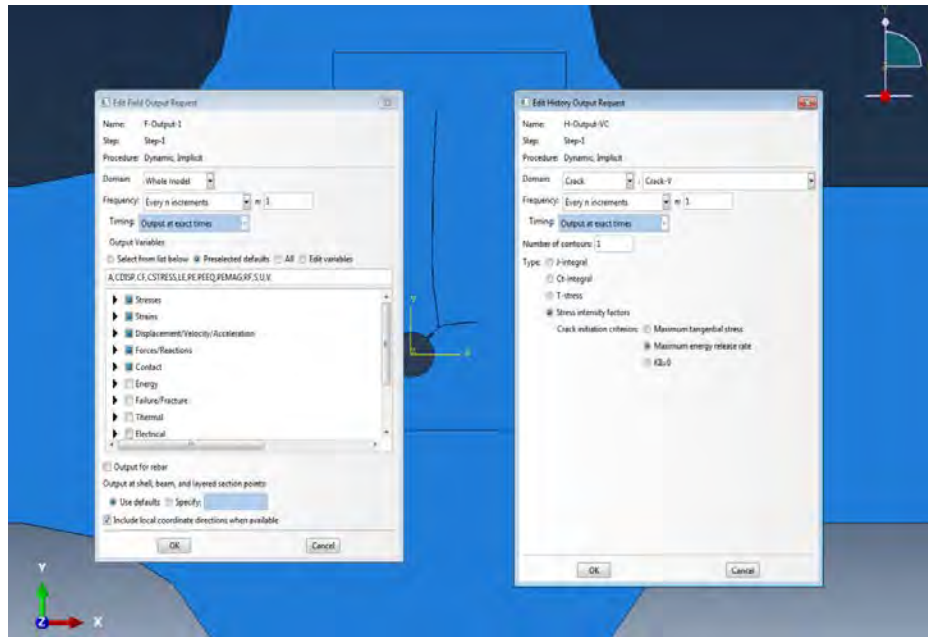


Figure A.7: Specifying the Needed Calculated Output Which are the ΔK s, ΔG s and the Cracks' Directions.

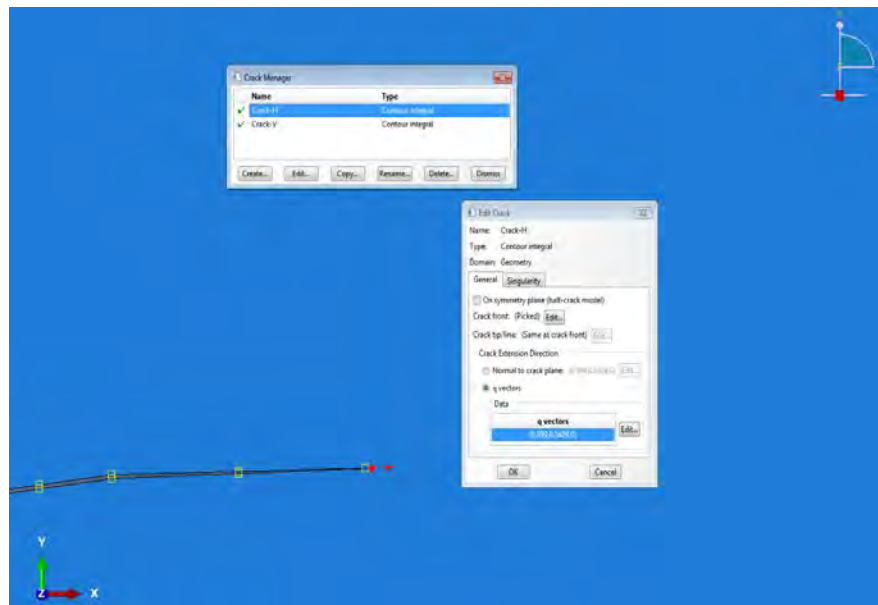


Figure A.8: Specifying the Location and the Direction Horizontal Crack-tip.

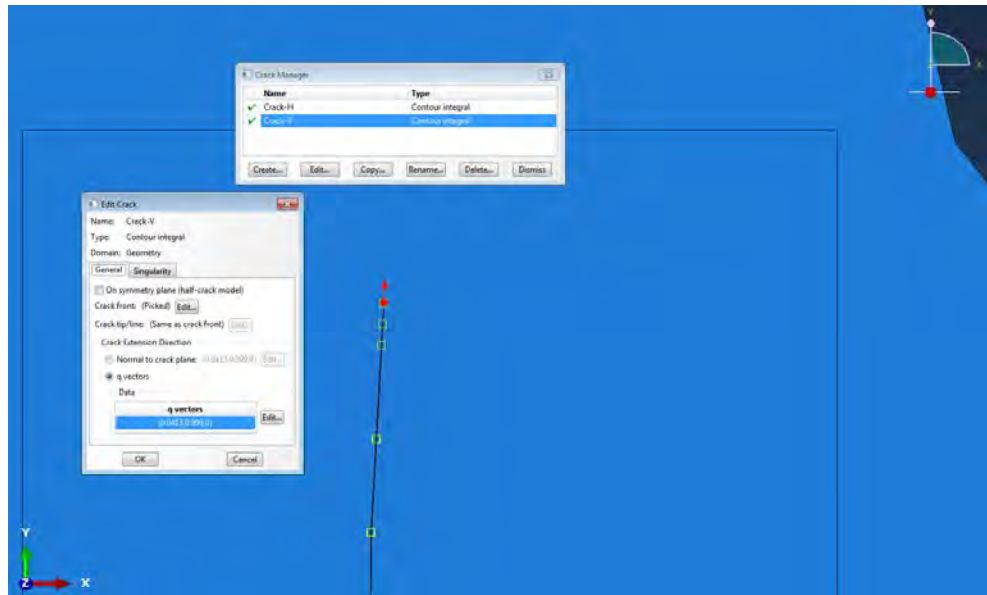


Figure A.9: Specifying the Location and the Direction Vertical Crack-tip.

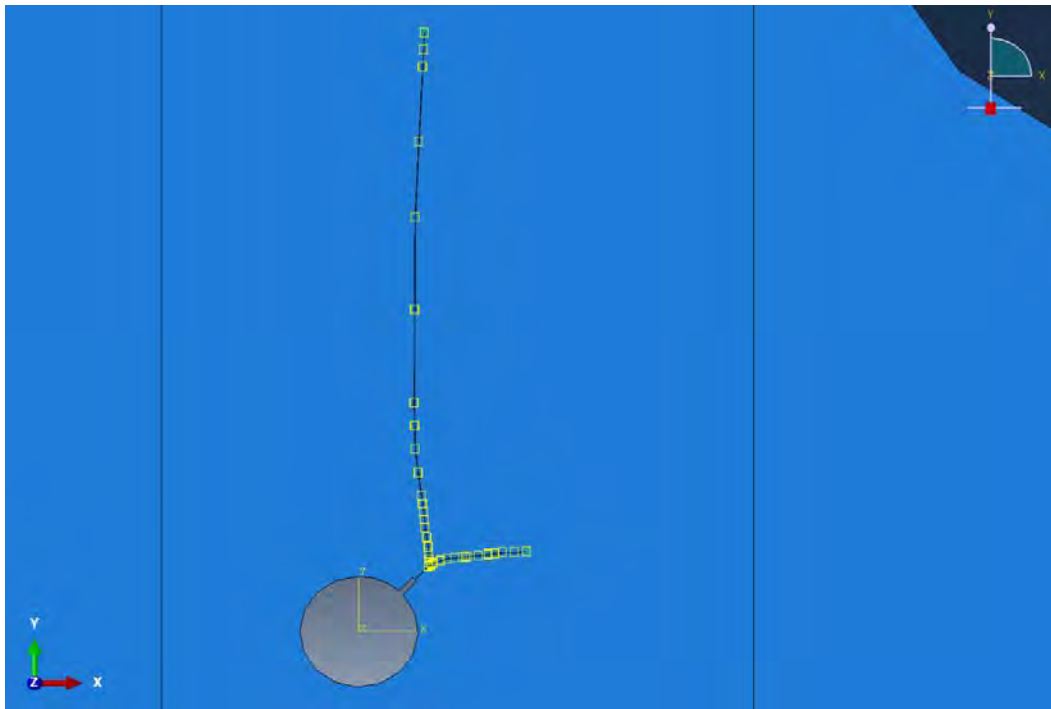


Figure A.10: Setting the Boundary Conditions to the Cracks (No Friction between the Adjacent Surfaces of a Certain Crack), Also Choosing the Masters' and the Slaves' edges.

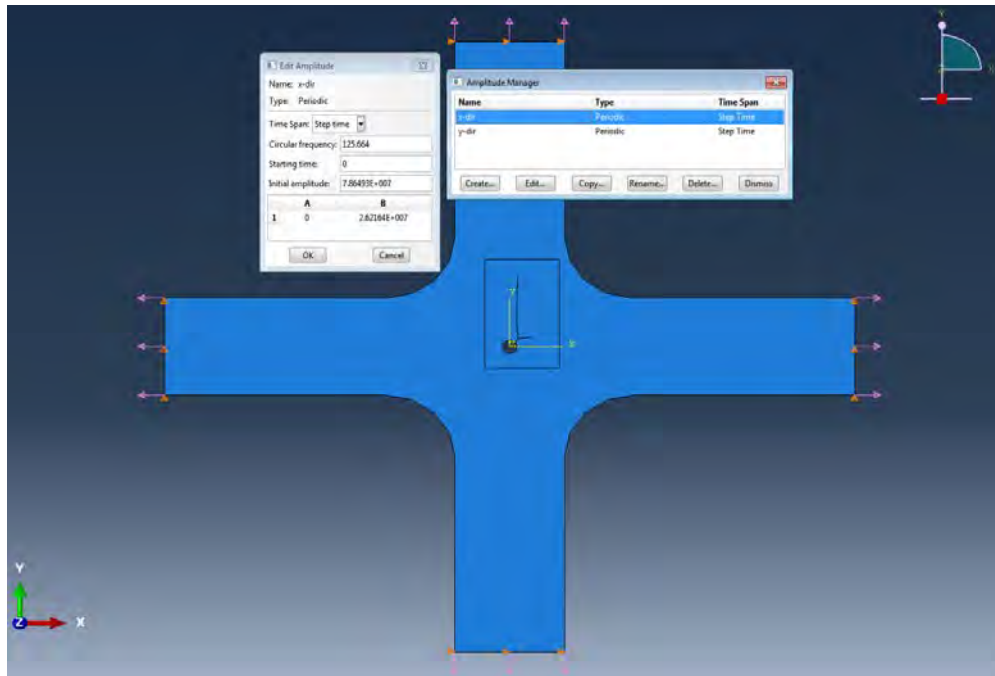


Figure A.11: Specifying the Dynamic Loads to the Horizontal End Arms of the Specimen.

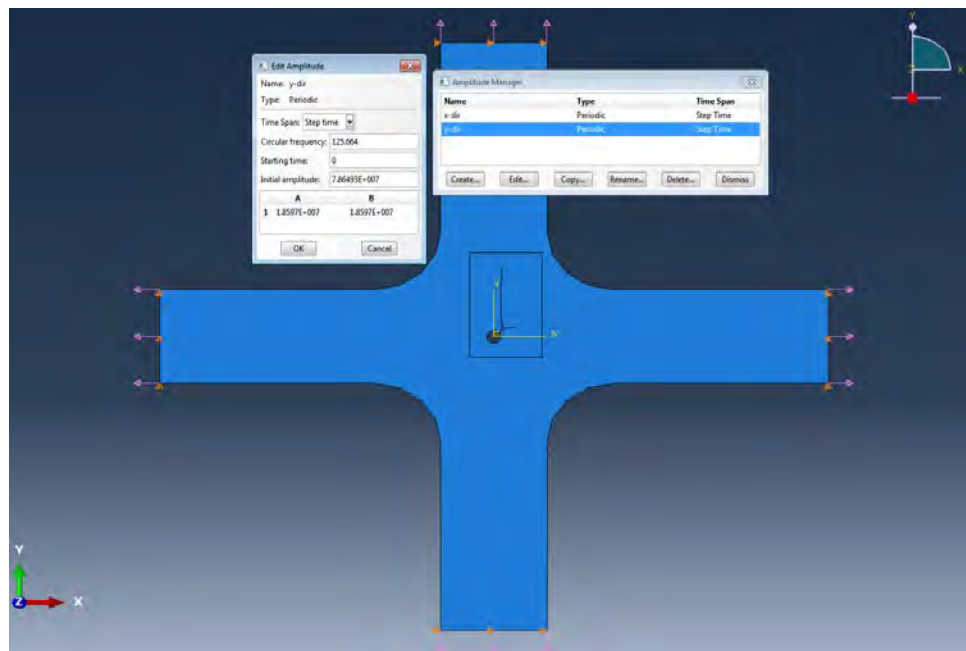


Figure A.12: Specifying the Dynamic Loads to the Vertical End Arms of the Specimen.

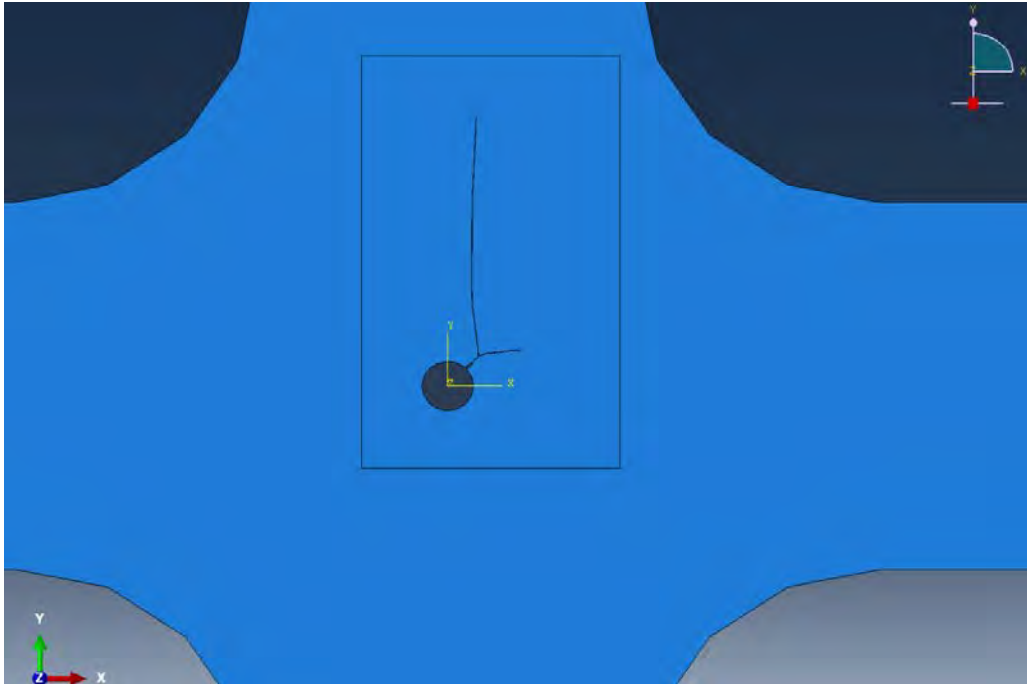


Figure A.13: Creating an Area that Need to Have Concentrated Mesh Later in Order to Get an Accurate Calculated Results.

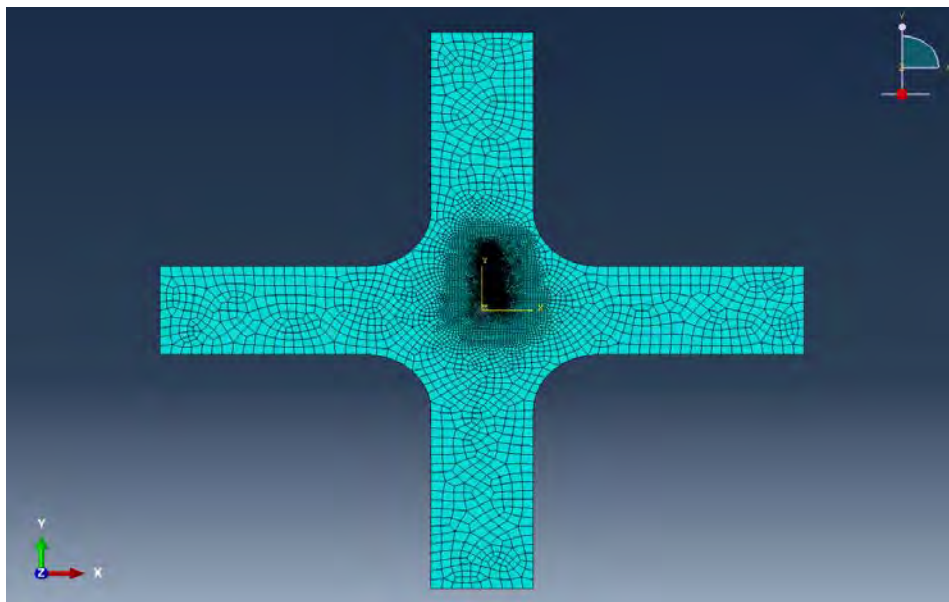


Figure A.14: Meshing the Whole Specimen including the Concentrated Area.

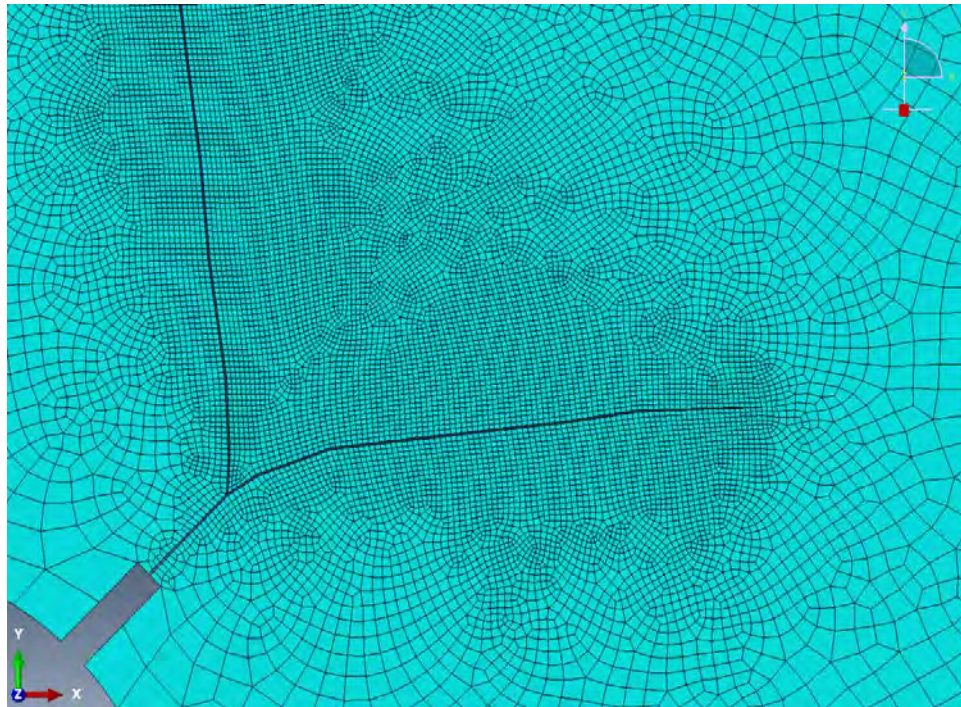


Figure A.15: A Closer Look to the the Concentrated Area Mesh.



Figure A.16: Creating a Jop to be Submitted Later.

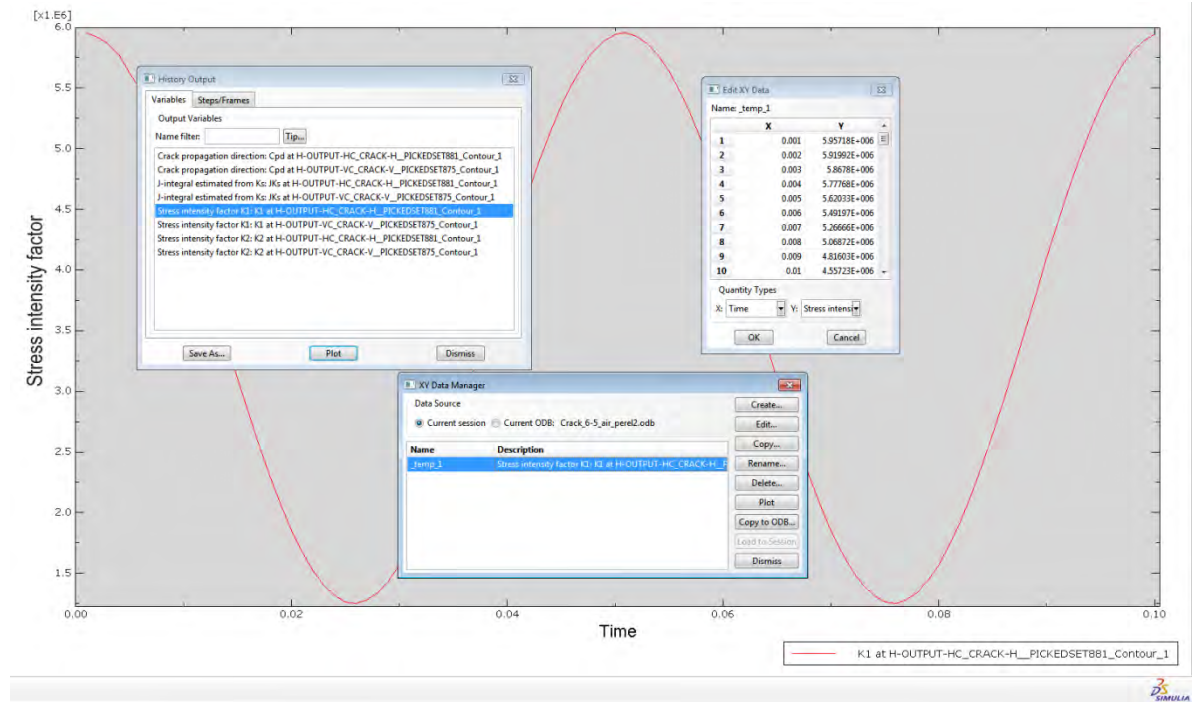


Figure A.17: One of the Results after finishing the Calculations.

Appendix B: Pictures of the Cracks at Different Biaxility ratio, Conditions and Environments.

The following pictures were taken when the X-direction loads applied first:



Figure B.1: Crack shape with 45° of phase difference at the beginning of cycles in air environment.

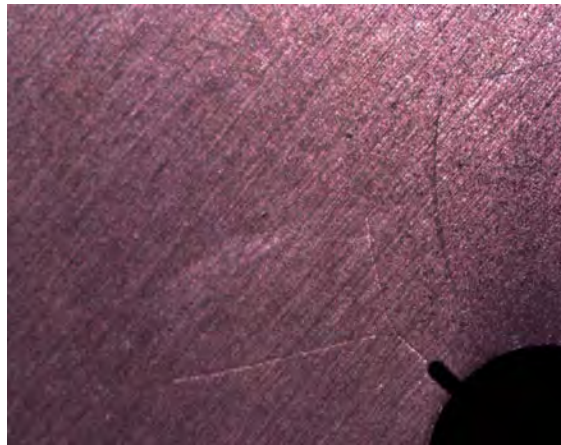


Figure B.2: Cracks shape with 45° of phase difference at the 60,000 cycles in air environment.

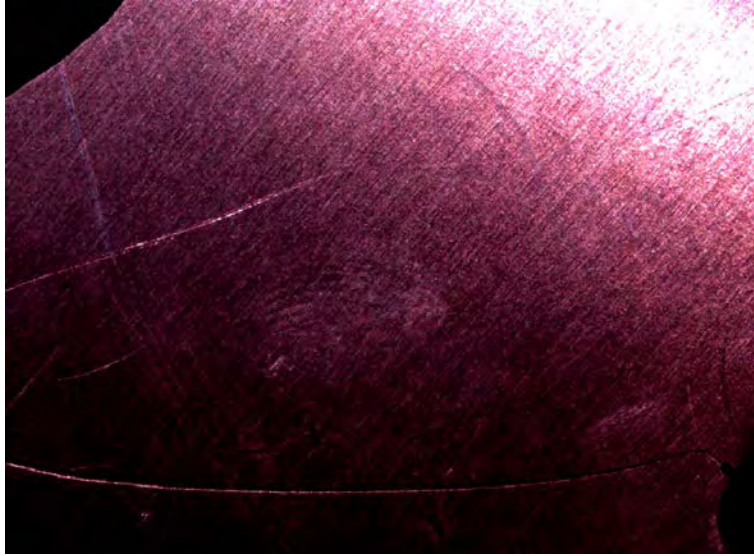


Figure B.3: Crack shape with 45° of phase difference at 1,139,198 cycles in air environment.

The following pictures were taken when the Y-direction loads applied first:



Figure B.4: Crack shape with 45° of phase difference at the beginning of cycles in air environment.



Figure B.5: Crack shape with 45° of phase difference at 52,000 cycles in air environment.

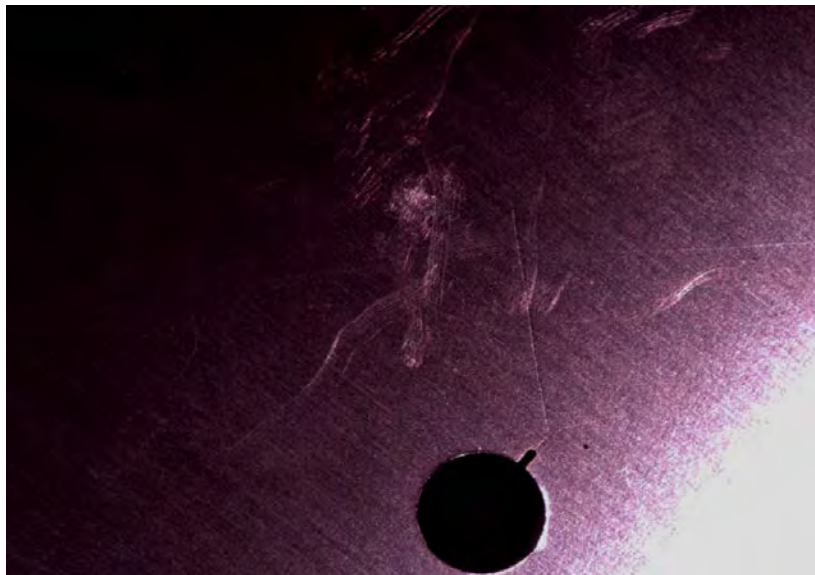


Figure B.6: Crack shape with 45° of phase difference at 95,000 cycles in air environment.

The following pictures were taken when the X-direction loads applied first:

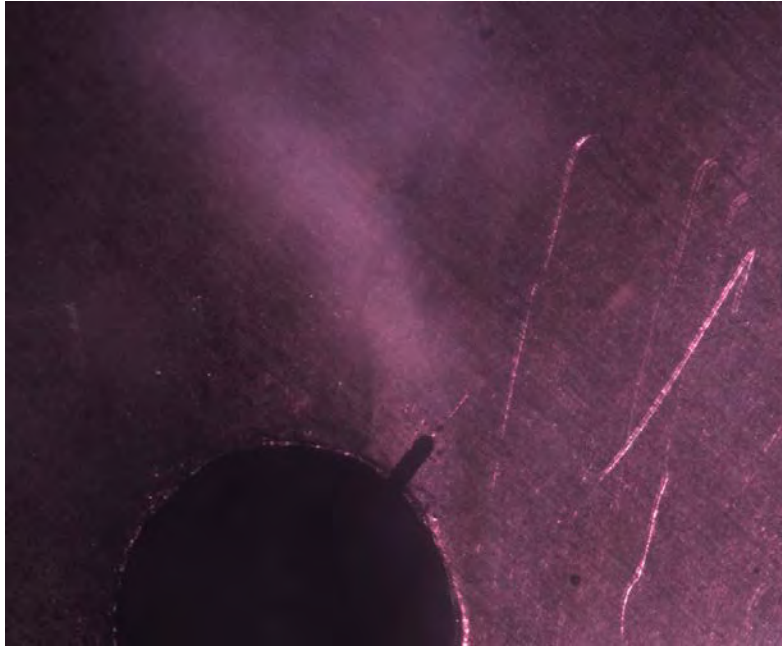


Figure B.7: Crack shape with 45° of phase difference at the beginning of cycles in saltwater environment.

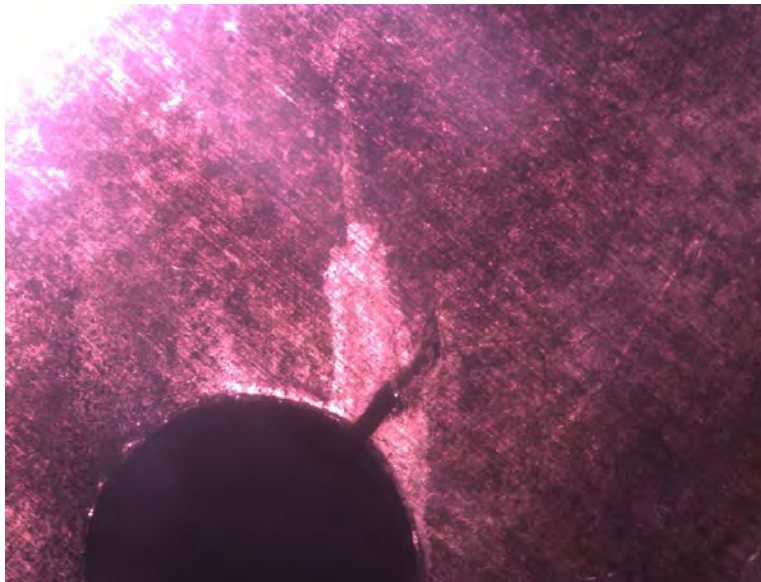


Figure B.8: Crack shape with 45° of phase difference at 135,300 cycles in saltwater environment.

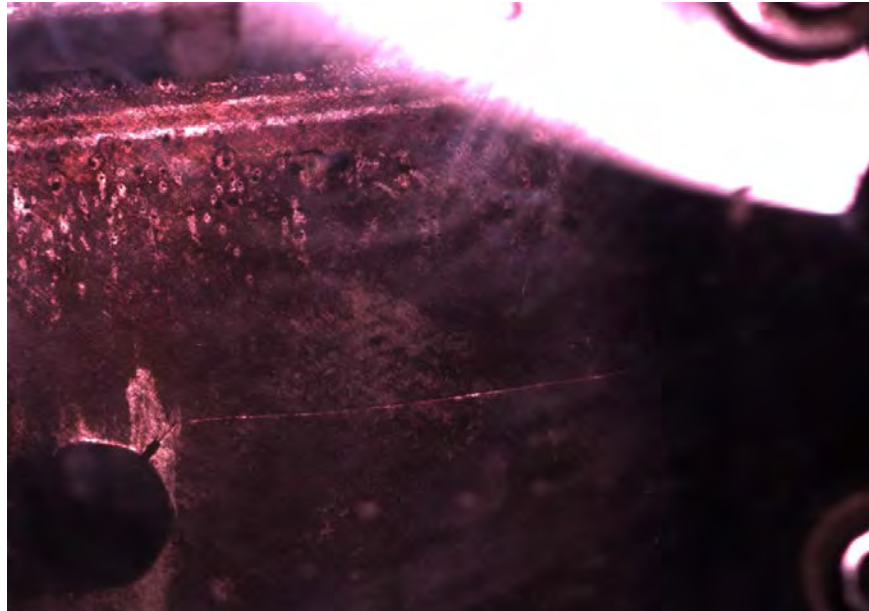


Figure B.9: Crack shape with 45° of phase difference at 305,300 cycles in saltwater environment.

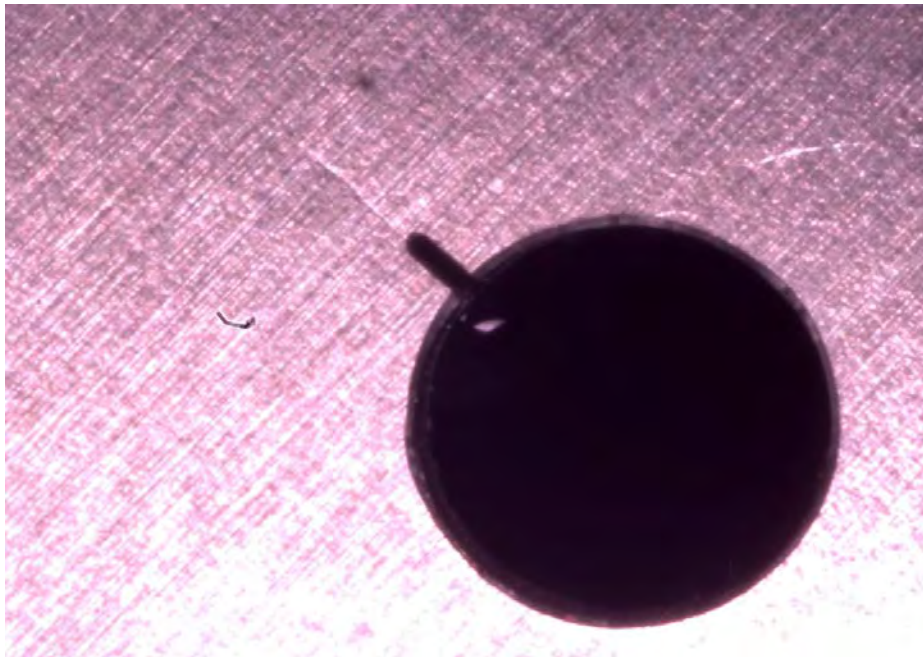


Figure B.10: Crack shape with 90° of phase difference at the beginning of cycles in air environment.

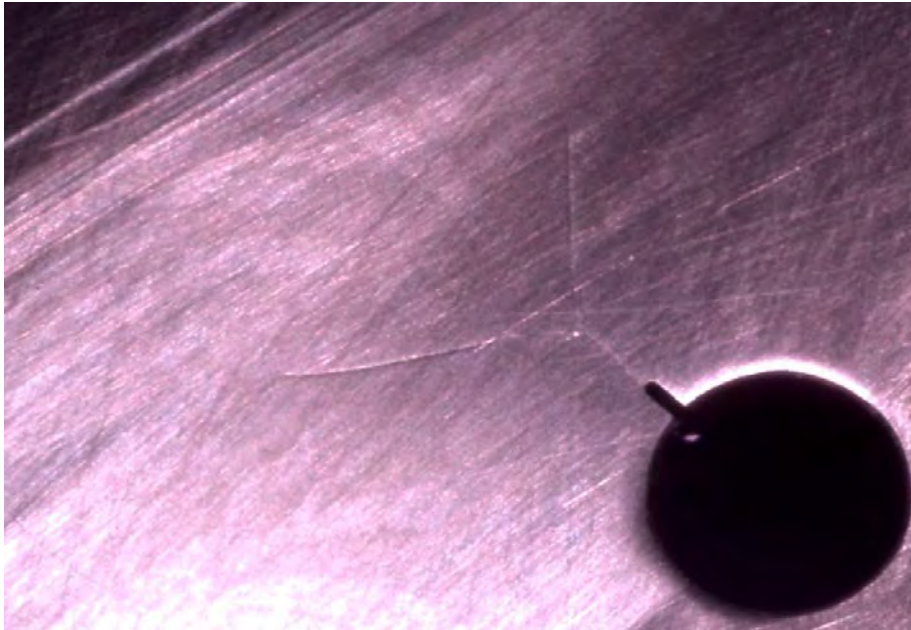


Figure B.11: Crack shape with 90° of phase difference at 170,000 cycles in air environment.

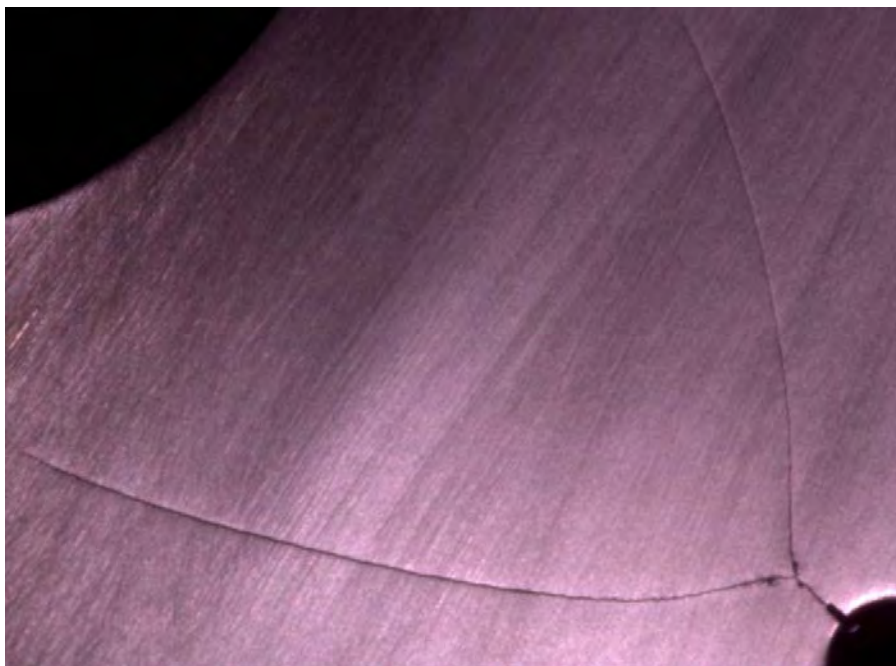


Figure B.12: Crack shape with 90° of phase difference at 270,000 cycles in air environment.

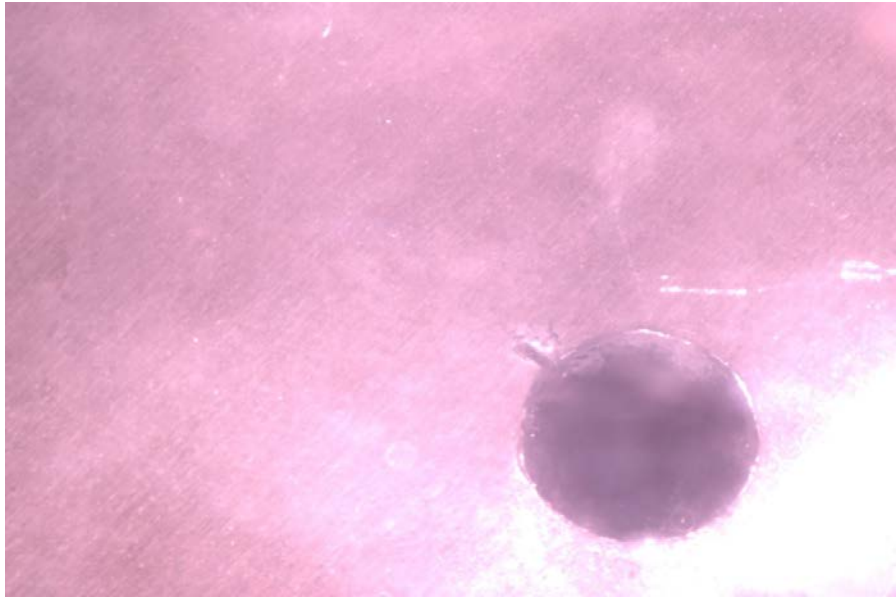


Figure B.13: Crack shape with 90° of phase difference at the beginning of cycles in saltwater environment.



Figure B.14: Crack shape with 90° of phase difference at 145,000 cycles in saltwater environment.



Figure B.15: Crack shape with 90° of phase difference at 174,500 cycles in air environment.

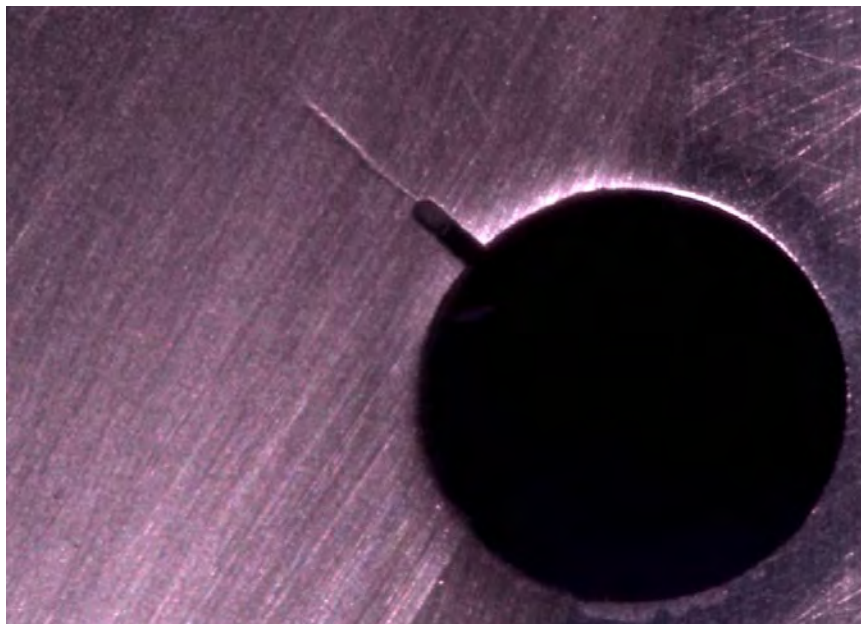


Figure B.16: Crack shape with 180° of phase difference at the beginning of cycles in air environment.

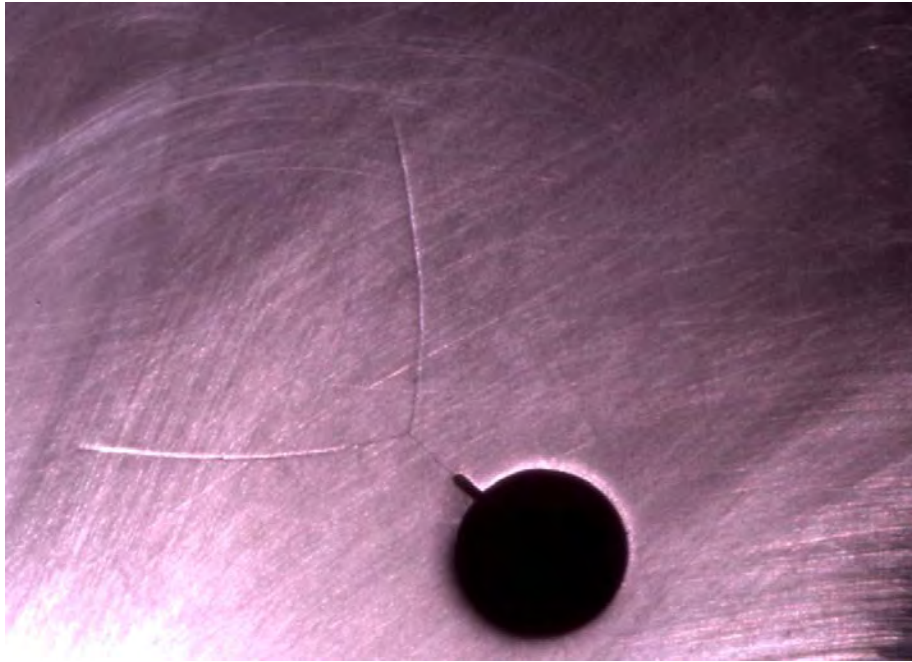


Figure B.17: Crack shape with 180° of phase difference at 80,000 cycles in air environment.

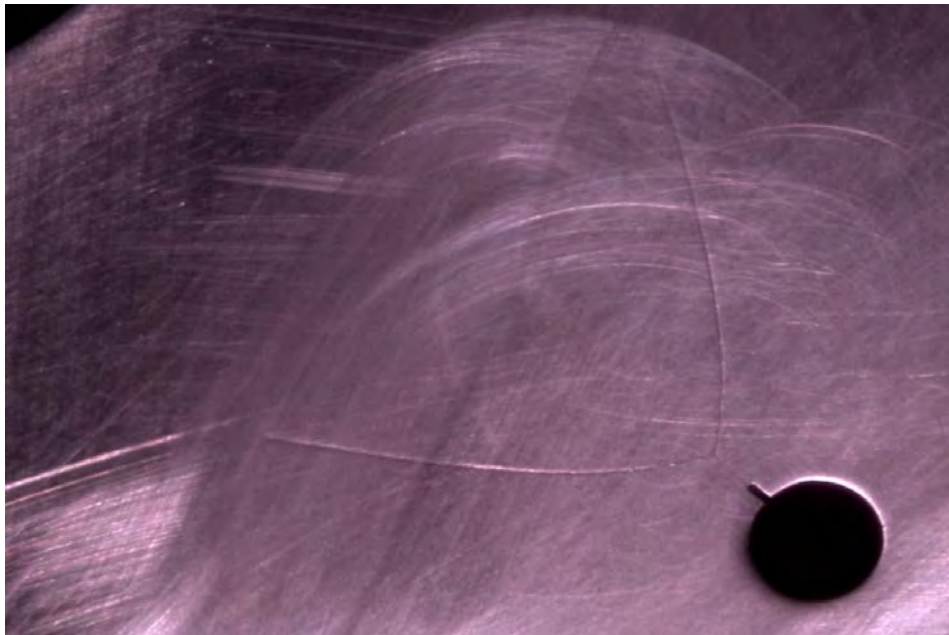


Figure B.18: Crack shape with 180° of phase difference at 110,000 cycles in air environment.

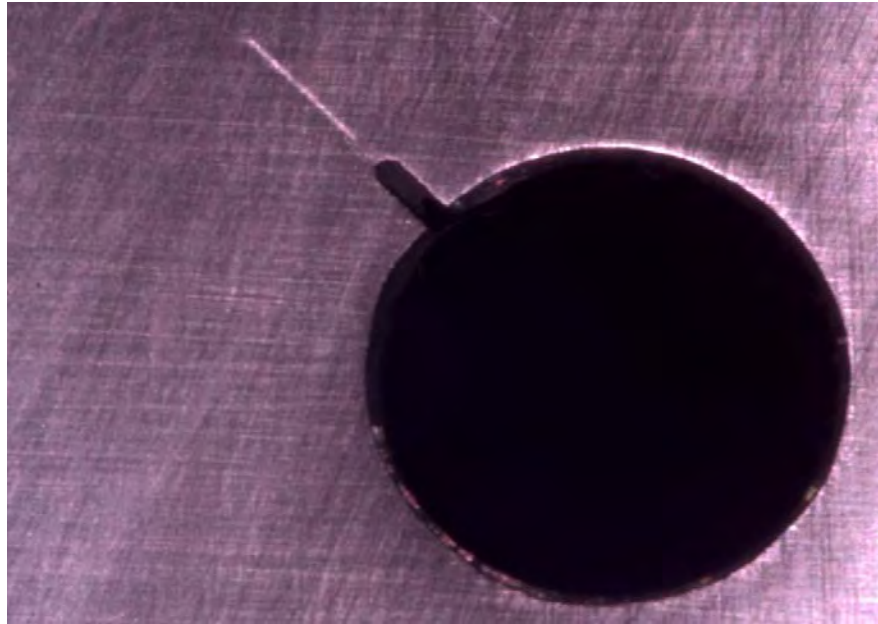


Figure B.19: Crack shape with 180° of phase difference at the beginning of cycles in saltwater environment.

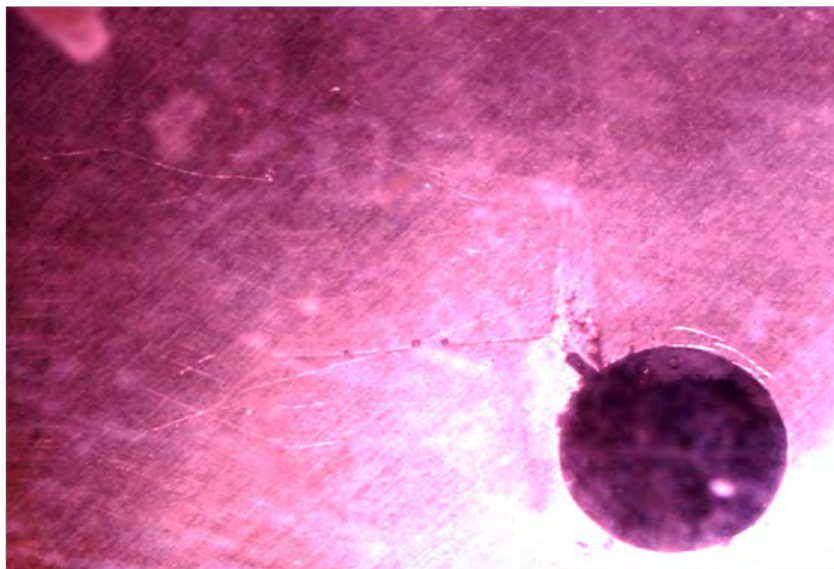


Figure B.20: Crack shape with 180° of phase difference at 10,000 cycles in saltwater environment.

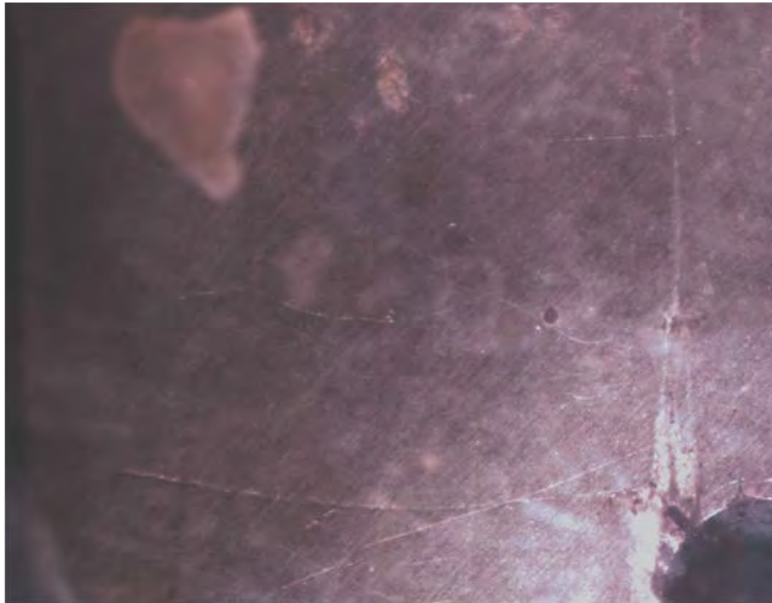


Figure B.21: Crack shape with 180° of phase difference at 26,000 cycles in saltwater environment.

Appendix C: Matlab Codes which were used to calculate the Directions of the Angles at the Bifurcations.

Code 1

```
% The Direction of the Initial Crack Propagation in Case of Biaxial
Fatigue
% test with PD=45°:
clc
clear all
close all

%Finite element Data:

t_abaq = [0.001
0.002
0.003
0.004
0.005
0.006
0.007
0.008
0.009
0.01
0.011
0.012
0.013
0.014
0.015
0.016
0.017
0.018
0.019
0.02
0.021
0.022
0.023
0.024
0.025
```



```
0.026
0.027
0.028
0.029
0.03
0.031
0.032
0.033
0.034
0.035
0.036
0.037
0.038
0.039
0.04
0.041
0.042
0.043
0.044
0.045
0.046
0.047
0.048
];

thetaa=[4.348
6.076
7.3
8.308
9.244
10.18
11.044
11.908
12.664
13.348
13.924
14.32
14.536
14.5
14.212
13.672
```

```

12.808
11.728
10.396
8.884
7.156
4.456
1.66
-3.136
-5.932
-8.056
-9.676
-11.152
-12.448
-13.492
-14.248
-14.752
-15.004
-14.968
-14.752
-14.32
-13.708
-13.024
-12.232
-11.368
-10.468
-9.532
-8.596
-7.624
-6.472
-4.96
-2.008
1.081
];

```

```

%Analytical Calculation:

```

```

t=(0: 0.001: 0.1);
time_norm = 5*t+0.009;
sigma_x = 7.912e7+2.638e7*cos(2*pi*10*t);
sigma_y = 7.912e7+2.638e7*cos(2*pi*10*t+pi/4);
numerator = sigma_y - sigma_x;

```

```

denominator = (sigma_y + sigma_x);
r = numerator./ denominator;
theta = (-2*r+14/3*r.^3)*180/pi;

%Finite Elemnt Result:

time_norm_abaq =10*(t_abaq);

%plot:

plot(time_norm, theta, '-r', time_norm_abaq, thetaa, '--black');
xlabel(' t/T ', 'FontSize',12)
ylabel(' Initial Direction of crack propagation \theta
(degrees)', 'FontSize',12)
legend('Analytical Result', 'Finite Element Result')
title('The Direction of the Initial Crack Propagation in Case of
Biaxial Fatigue test with PD=45°', 'FontSize',12, 'FontWeight', 'bold')

```

Figure C.1: Matlab Code for Calculating the Direction of the Initial Crack Propagation in Case of Biaxial Fatigue test with PD=45°.

Code 2

```
% The Direction of the Initial Crack Propagation in Case of Biaxial Fatigue  
% test with PD=90°:
```

```
clc  
clear all  
close all
```

```
%Finite elemnt Data:
```

```
t_abaq = [0.1  
0.102  
0.104  
0.106  
0.108  
0.11  
0.112  
0.114  
0.116  
0.118  
0.12  
0.122  
0.124  
0.126  
0.128  
0.13  
0.132  
0.134  
0.136  
0.138  
0.14  
0.142  
0.144  
0.146  
0.148  
0.15  
0.152  
0.154  
0.156
```

0.158
0.16
0.162
0.164
0.166
0.168
0.17
0.172
0.174
0.176
0.178
0.18
0.182
0.184
0.186
0.188
0.19
0.192
0.194
0.196
0.198
0.2];

K1_abaq=[6.51486E+006
6.40872E+006
6.28752E+006
6.15308E+006
6.00742E+006
5.8528E+006
5.69162E+006
5.52645E+006
5.35991E+006
5.1947E+006
5.03352E+006
4.87902E+006
4.73377E+006
4.6002E+006
4.48055E+006
4.37685E+006
4.29084E+006
4.22397E+006
4.17736E+006
4.15175E+006

4.14752E+006
4.1647E+006
4.2029E+006
4.2614E+006
4.33914E+006
4.43474E+006
4.54653E+006
4.67261E+006
4.81087E+006
4.95904E+006
5.11472E+006
5.27544E+006
5.43867E+006
5.6019E+006
5.76263E+006
5.91844E+006
6.06701E+006
6.20612E+006
6.33374E+006
6.44799E+006
6.54719E+006
6.62989E+006
6.69484E+006
6.74107E+006
6.76784E+006
6.7747E+006
6.76148E+006
6.72828E+006
6.6755E+006
6.60385E+006
6.51432E+006
];

K2_abaq = [1.67278E+006
1.81917E+006
1.94166E+006
2.03828E+006
2.10745E+006
2.14808E+006
2.15957E+006
2.1418E+006
2.09514E+006
2.02045E+006

1.91903E+006
1.79261E+006
1.64333E+006
1.47363E+006
1.28627E+006
1.08426E+006
870799
649228
422985
195556
-29577.1
-248977
-459300
-657339
-840068
-1.00468E+006
-1.14863E+006
-1.26969E+006
-1.36594E+006
-1.43586E+006
-1.47829E+006
-1.49253E+006
-1.47829E+006
-1.43571E+006
-1.36539E+006
-1.26836E+006
-1.14608E+006
-1.00041E+006
-833579
-648166
-447054
-233385
-10518
218027
448621
677581
901231
1.11596E+006
1.31829E+006
1.50492E+006
1.6728E+006
];

```

%Analytical Calculation:

t=(0: 0.001: 0.1);
time_norm = 10*t;
sigma_x = 7.912e7+2.638e11cos(2*pi*10*t);
sigma_y = 7.912e7-2.638e11sin(2*pi*10*t);
numerator = sigma_y - sigma_x;
denominator = sigma_y + sigma_x;
r = numerator./ denominator;
theta = (-2*r+14/3*r.^3)*180/pi;

%Finite Elemnt Result:
r_abaq = K2_abaq./K1_abaq;
theta_abaq = -((-2*r_abaq+14/3*r_abaq.^3)*180/pi);
time_norm_abaq =10*(t_abaq-0.1);

%Plot:

plot(time_norm, theta, '-r', time_norm_abaq, theta_abaq, '--black');
xlabel(' t/T ', 'FontSize',12)
ylabel(' Initial Direction of crack propagation \theta (degrees)', 'FontSize',12)
legend('Analytical Result', 'Finite Element Result', 'Experimental Result')
title('The Direction of the Initial Crack Propagation in Case of Biaxial Fatigue test with PD=90°', 'FontSize',12, 'FontWeight', 'bold')

```

Figure C.2: Matlab Code for Calculating the Direction of the Initial Crack Propagation in Case of Biaxial Fatigue test with PD=90°.

Code 3

```
% The Direction of the Initial Crack Propagation in Case of Biaxial Fatigue
% test with PD=180°:

clc
clear all
close all

%Finite elemnt Data:

t_abaq = [0.1
0.101
0.102
0.103
0.104
0.105
0.106
0.107
0.108
0.109
0.11
0.111
0.112
0.113
0.114
0.115
0.116
0.117
0.118
0.119
0.12
0.121
0.122
0.123
0.124
0.125
0.126
0.127
0.128
```

0.129
0.13
0.131
0.132
0.133
0.134
0.135
0.136
0.137
0.138
0.139
0.14
0.141
0.142
0.143
0.144
0.145
0.146
0.147
0.148
0.149
0.15
0.151
0.152
0.153
0.154
0.155
0.156
0.157
0.158
0.159
0.16
0.161
0.162
0.163
0.164
0.165
0.166
0.167
0.168
0.169
0.17
0.171

0.172
0.173
0.174
0.175
0.176
0.177
0.178
0.179
0.18
0.181
0.182
0.183
0.184
0.185
0.186
0.187
0.188
0.189
0.19
0.191
0.192
0.193
0.194
0.195
0.196
0.197
0.198
0.199
0.2];

K1_abaq=[5.89366E+006
5.89285E+006
5.89044E+006
5.88645E+006
5.88093E+006
5.87392E+006
5.8655E+006
5.85576E+006
5.84479E+006
5.83271E+006
5.81964E+006
5.8057E+006
5.79103E+006

5.77578E+006
5.76009E+006
5.7441E+006
5.72796E+006
5.71181E+006
5.69579E+006
5.68002E+006
5.66463E+006
5.64972E+006
5.6354E+006
5.62175E+006
5.60884E+006
5.59674E+006
5.58548E+006
5.57511E+006
5.56563E+006
5.55705E+006
5.54937E+006
5.54256E+006
5.5366E+006
5.53144E+006
5.52705E+006
5.52336E+006
5.52032E+006
5.51786E+006
5.51593E+006
5.51445E+006
5.51336E+006
5.51259E+006
5.51209E+006
5.5118E+006
5.51166E+006
5.51162E+006
5.51166E+006
5.51172E+006
5.51178E+006
5.51183E+006
5.51184E+006
5.51183E+006
5.51178E+006
5.51172E+006
5.51165E+006
5.51162E+006

5.51165E+006
5.51179E+006
5.51208E+006
5.51258E+006
5.51334E+006
5.51442E+006
5.51589E+006
5.51782E+006
5.52027E+006
5.5233E+006
5.52698E+006
5.53136E+006
5.53651E+006
5.54245E+006
5.54925E+006
5.55692E+006
5.56548E+006
5.57494E+006
5.5853E+006
5.59654E+006
5.60863E+006
5.62153E+006
5.63516E+006
5.64947E+006
5.66436E+006
5.67974E+006
5.6955E+006
5.71151E+006
5.72764E+006
5.74377E+006
5.75975E+006
5.77544E+006
5.79068E+006
5.80534E+006
5.81927E+006
5.83234E+006
5.84442E+006
5.85538E+006
5.86512E+006
5.87354E+006
5.88055E+006
5.88607E+006
5.89006E+006

5.89247E+006
5.89328E+006];

K2_abaq = [2.91105E+006
2.90552E+006
2.88898E+006
2.86148E+006
2.82317E+006
2.77422E+006
2.71484E+006
2.64532E+006
2.56595E+006
2.47711E+006
2.37917E+006
2.27257E+006
2.15777E+006
2.03524E+006
1.90552E+006
1.76914E+006
1.62665E+006
1.47863E+006
1.32569E+006
1.16841E+006
1.00742E+006
843334
676796
508437
338898
168820
-1153.69
-170382
-338226
-504051
-667229
-827138
-983167
-1.13472E+006
-1.2812E+006
-1.42204E+006
-1.55669E+006
-1.68461E+006
-1.8053E+006

-1.91826E+006
-2.02304E+006
-2.11921E+006
-2.20638E+006
-2.28417E+006
-2.35227E+006
-2.41039E+006
-2.45828E+006
-2.49574E+006
-2.52262E+006
-2.53879E+006
-2.54419E+006
-2.53879E+006
-2.52262E+006
-2.49574E+006
-2.45828E+006
-2.41039E+006
-2.35227E+006
-2.28417E+006
-2.20638E+006
-2.11922E+006
-2.02305E+006
-1.91827E+006
-1.8053E+006
-1.68462E+006
-1.5567E+006
-1.42205E+006
-1.2812E+006
-1.13472E+006
-983173
-827144
-667234
-504056
-338230
-170385
-1155.7
168819
338899
508440
676801
843342
1.00743E+006
1.16842E+006

```

1.3257E+006
1.47865E+006
1.62667E+006
1.76916E+006
1.90555E+006
2.03528E+006
2.1578E+006
2.27261E+006
2.37921E+006
2.47715E+006
2.566E+006
2.64536E+006
2.71489E+006
2.77426E+006
2.82322E+006
2.86153E+006
2.88903E+006
2.90558E+006
2.9111E+006];

```

%Analytical Calculation:

```

t=(0: 0.001: 0.1);
time_norm = 10*t;
sigma_x = 7.912e7+2.638e11cos(2*pi*10*t);
sigma_y = 7.912e7-2.638e11cos(2*pi*10*t);
numerator = sigma_y - sigma_x;
denominator = sigma_y + sigma_x;
r = numerator./ denominator;
theta = (-2*r+14/3*r.^3)*180/pi;

```

%Finite Elemnt Result:

```

r_abaq = K2_abaq./K1_abaq;
theta_abaq = -((-2*r_abaq+14/3*r_abaq.^3)*180/pi);
time_norm_abaq = 10*(t_abaq-0.1);

```

%Plot:

```

plot(time_norm, theta, '-r', time_norm_abaq, theta_abaq, '--black');
xlabel(' t/T ',FontSize,12)

```



```
ylabel(' Initial Direction of crack propagation \theta (degrees)','FontSize',12)
legend('Analytical Result', 'Finite Element Result','Experimental Result')
title('The Direction of the Initial Crack Propagation in Case of Biaxial Fatigue test with
PD=180°','FontSize',12,'FontWeight','bold')
```

Figure C.3: Matlab Code for Calculating the Direction of the Initial Crack Propagation in
Case of Biaxial Fatigue test with PD=180°.

Code 4

```
%Calculation of The Direction of the Horizontal Crack Propagation after splitting of
%the precrack of Biaxial Fatigue test with PD=45°:
clc
clear all
close all

%Finite elemnt Data:

t_abaq = [0.1
0.102
0.104
0.106
0.108
0.11
0.112
0.114
0.116
0.118
0.12
0.122
0.124
0.126
0.128
0.13
0.132
0.134
0.136
0.138
0.14
0.142
0.144
0.146
0.148
0.15
0.152
0.154
0.156
0.158
0.16
```

0.162
0.164
0.166
0.168

];

K1_abaq=[851011

1188827.556
1526644.111
1864460.667
2202277.222
2540093.778
2877910.333
3215726.889
3553543.444
3891360
3553543.444
3215726.889
2877910.333
2540093.778
2202277.222
1864460.667
1526644.111
1188827.556
851011
1188827.556
1526644.111
1864460.667
2202277.222
2540093.778
2877910.333
3215726.889
3553543.444
3891360
3553543.444
3215726.889
2877910.333
2540093.778
2202277.222
1864460.667
1526644.111];

```
K2_abaq = [569897
```

```
676878.4444
```

```
783859.8889
```

```
890841.3333
```

```
997822.7778
```

```
1104804.222
```

```
1211785.667
```

```
1318767.111
```

```
1425748.556
```

```
1532730
```

```
1425748.556
```

```
1318767.111
```

```
1211785.667
```

```
1104804.222
```

```
997822.7778
```

```
890841.3333
```

```
783859.8889
```

```
676878.4444
```

```
569897
```

```
676878.4444
```

```
783859.8889
```

```
890841.3333
```

```
997822.7778
```

```
1104804.222
```

```
1211785.667
```

```
1318767.111
```

```
1425748.556
```

```
1532730
```

```
1425748.556
```

```
1318767.111
```

```
1211785.667
```

```
1104804.222
```

```
997822.7778
```

```
890841.3333
```

```
783859.8889];
```

```
%Finite Elemnt Result:
```

```
r_abaq = K2_abaq./K1_abaq;
```

```
theta_abaq = -((-2*r_abaq+14/3*r_abaq.^3)*180/pi);
```

```
time_norm_abaq =15*(t_abaq-0.1);
```

```
%Plot:
```

```

plot( time_norm_abaq, theta_abaq, '--black');
xlabel('t/T','FontSize',12,'FontWeight','bold')
ylabel('Direction of Horizontal Crack Propagation \theta
(degrees)','FontSize',12,'FontWeight','bold')
axis([0 1 -5 55 ])
legend('Finite Element Result')
title('The Direction of the Horizontal Crack after splitting of the precrack in Case of
Biaxial Fatigue test with PD=45°','FontSize',12,'FontWeight','bold')

```

Figure C.4: Matlab Code for Calculating the Direction of the Horizontal Crack that split from the precrack in Case of Biaxial Fatigue test with PD=45°.

Code 5

%Calculation of The Direction of the Vertical Crack Propagation after splitting of
%the precrack of Biaxial Fatigue test with PD=45°:

```
clc
```

```
clear all
```

```
close all
```

%Finite element Data:

```
t_abaq = [0.1
```

```
0.2
```

```
0.3
```

```
0.4
```

```
0.5
```

```
0.6
```

```
0.7
```

```
];
```

```
K1_abaq=[1924120
```

```
2461890
```

```
3790230
```

```
4423940
```

```
5233410
```

```
7915440
```

```
7165870
```

```
];
```

```
K2_abaq = [300643
```

```
310658
```

```
402749
```

```
582211
```

```

179524
287775.8
740734
];
%Finite Element Calculations:

r_abaq = K2_abaq./K1_abaq;
theta_abaq = -((-2*r_abaq+14/3*r_abaq.^3)*180/pi);
time_norm_abaq = 15*(t_abaq-0.1);

%Plot:

plot( time_norm_abaq, theta_abaq, '--black');
xlabel('t/T','FontSize',12,'FontWeight','bold')
ylabel('Direction of Vertical Crack Propagation \theta
(degrees)','FontSize',12,'FontWeight','bold')
axis([0 1 -5 55 ])
legend('Finite Element Result')
title('The Direction of the Vertical Crack after splitting of the precrack in Case of Biaxial
Fatigue test with PD=45°','FontSize',12,'FontWeight','bold')

```

Figure C.5: Matlab Code for Calculating the Direction of the Vertical Crack that split from the precrack in Case of Biaxial Fatigue test with PD=45°.

Code 6

```
%Calculation of The Direction of the Crack Propagation after splitting of  
%the precrack of Biaxial Fatigue test with PD=90°:
```

```
clc  
clear all  
close all
```

```
%Finite elemnt Data:
```

```
t_abaq = [0.1  
0.101  
0.102  
0.103  
0.104  
0.105  
0.106  
0.107  
0.108  
0.109  
0.11  
0.111  
0.112  
0.113  
0.114  
0.115  
0.116  
0.117  
0.118  
0.119  
0.12  
0.121  
0.122  
0.123  
0.124  
0.125  
0.126  
0.127  
0.128
```


0.129
0.13
0.131
0.132
0.133
0.134
0.135
0.136
0.137
0.138
0.139
0.14
0.141
0.142
0.143
0.144
0.145
0.146
0.147
0.148
0.149
0.15
0.151
0.152
0.153
0.154
0.155
0.156
0.157
0.158
0.159
0.16
0.161
0.162
0.163
0.164
0.165
0.166
0.167
0.168
0.169
0.17
0.171

0.172
0.173
0.174
0.175
0.176
0.177
0.178
0.179
0.18
0.181
0.182
0.183
0.184
0.185
0.186
0.187
0.188
0.189
0.19
0.191
0.192
0.193
0.194
0.195
0.196
0.197
0.198
0.199
0.2];

K1_abaq=[3.51548E+006
3.34857E+006
3.18693E+006
3.03119E+006
2.88193E+006
2.73972E+006
2.60509E+006
2.47856E+006
2.36062E+006
2.25172E+006
2.15227E+006
2.06265E+006
1.98323E+006

1.9143E+006
1.85614E+006
1.80898E+006
1.773E+006
1.74836E+006
1.73516E+006
1.73346E+006
1.74329E+006
1.76462E+006
1.79739E+006
1.84149E+006
1.89678E+006
1.96305E+006
2.04008E+006
2.1276E+006
2.22528E+006
2.33279E+006
2.44973E+006
2.57568E+006
2.71016E+006
2.85269E+006
3.00274E+006
3.15973E+006
3.32307E+006
3.49215E+006
3.66631E+006
3.84488E+006
4.02715E+006
4.21241E+006
4.39993E+006
4.58896E+006
4.77872E+006
4.96845E+006
5.15738E+006
5.34472E+006
5.52971E+006
5.71156E+006
5.88952E+006
6.06285E+006
6.2308E+006
6.39268E+006
6.5478E+006
6.6955E+006

6.83516E+006
6.96619E+006
7.08803E+006
7.20018E+006
7.30216E+006
7.39356E+006
7.474E+006
7.54315E+006
7.60073E+006
7.64654E+006
7.68039E+006
7.70217E+006
7.71181E+006
7.70932E+006
7.69471E+006
7.66811E+006
7.62964E+006
7.5795E+006
7.51795E+006
7.44525E+006
7.36176E+006
7.26785E+006
7.16392E+006
7.05044E+006
6.92788E+006
6.79677E+006
6.65765E+006
6.51109E+006
6.3577E+006
6.19808E+006
6.03288E+006
5.86276E+006
5.68837E+006
5.51039E+006
5.32952E+006
5.14644E+006
4.96186E+006
4.77648E+006
4.591E+006
4.40612E+006
4.22254E+006
4.04095E+006
3.86203E+006

3.68645E+006
3.51488E+006];

K2_abaq = [834345

851851

867393

880939

892463

901948

909385

914767

918099

919387

918645

915891

911147

904441

895803

885267

872872

858658

842672

824961

805577

784577

762020

737969

712492

685662

657556

628256

597849

566429

534093

500946

467096

432660

397757

362513

327059

291528

256061

220800

185887
151471
117697
84714.7
52668.8
21704.3
-8036.98
-36417.2
-63302.9
-88566.5
-112087
-133750
-153449
-171087
-186576
-199836
-210800
-219409
-225617
-229386
-230691
-229519
-225869
-219749
-211180
-200194
-186837
-171163
-153239
-133142
-110960
-86792.9
-60747.6
-32942.5
-3504.11
27432.7
59725.8
93226.4
127780
163227
199404
236146
273285

```

310651
348079
385400
422452
459073
495108
530407
564826
598226
630478
661460
691059
719171
745700
770560
793673
814973
834401];

%Calculation of The Direction of the Crack Propagation after splitting of
%the precrack of Biaxial Fatigue test with PD=90°:

r_abaq = K2_abaq./K1_abaq;
theta_abaq = -((-2*r_abaq+14/3*r_abaq.^3)*180/pi);
time_norm_abaq = 10*(t_abaq-0.1);

% Plot:

plot(time_norm_abaq, theta_abaq, '-r');
xlabel('t/T','FontSize',12)
ylabel('Direction of crack propagation \theta (degrees)','FontSize',12)
axis([0 1 -5 30])
legend('Finite Element Result','FontSize',12)
title('The Direction of the Crack Propagation after splitting of Biaxial Fatigue test with
PD=90°','FontSize',12,'FontWeight','bold')

```

Figure C.6: Matlab Code for Calculating the Direction of one of the symmetric Cracks that split from the precrack in Case of Biaxial Fatigue test with PD=90°.

Code 7

```
%Calculation of The Direction of the Crack Propagation after splitting of  
%the precrack of Biaxial Fatigue test with PD=180°:
```

```
clc  
clear all  
close all
```

```
%Finite elemnt Data:
```

```
t_abaq = [0.1  
0.102  
0.104  
0.106  
0.108  
0.11  
0.112  
0.114  
0.116  
0.118  
0.12  
0.122  
0.124  
0.126  
0.128  
0.13  
0.132  
0.134  
0.136  
0.138  
0.14  
0.142  
0.144  
0.146  
0.148  
0.15  
0.152  
0.154  
0.156  
0.158  
0.16  
0.162
```



```
0.164
0.166
0.168
0.17
0.172
0.174
0.176
0.178
0.18
0.182
0.184
0.186
0.188
0.19
0.192
0.194
0.196
0.198
0.2];

theta_abaq = [-52.668
-51.948
-49.86
-46.512
-42.228
-37.332
-32.256
-27.288
-22.752
-18.612
-14.832
-11.628
-9.216
-7.308
-5.616
-3.6
0
0
0
0
0
0
1.656
2.304
2.628
2.7
```

```

2.628
2.304
1.656
0
0
0
0
0
0
0
-3.6
-5.616
-7.308
-9.216
-11.664
-14.868
-18.648
-22.752
-27.36
-32.292
-37.404
-42.3
-46.584
-49.932
-52.056
-52.776];

%Calculation of The Direction of the Crack Propagation after splitting of
%the precrack of Biaxial Fatigue test with PD=90°:

time_norm_abaq = 10*(t_abaq-0.1);

% Plot:

plot(time_norm_abaq, theta_abaq, '-r');
xlabel('t/T','FontSize',12)
ylabel('Direction of crack propagation \theta (degrees)','FontSize',12)
axis([0 1 -5 55])
legend('Finite Element Result','FontSize',12)
title('The Direction of the Crack Propagation after splitting of the precrack of Biaxial Fatigue
test with PD=180°','FontSize',12,'FontWeight','bold')

```

Figure C.7: Matlab Code for Calculating the Direction of one of the symmetric Cracks that split from the precrack in Case of Biaxial Fatigue test with PD=180.

Appendix D: Sum of Crack Growth Rates versus Sum of Strain Energy Release Rate

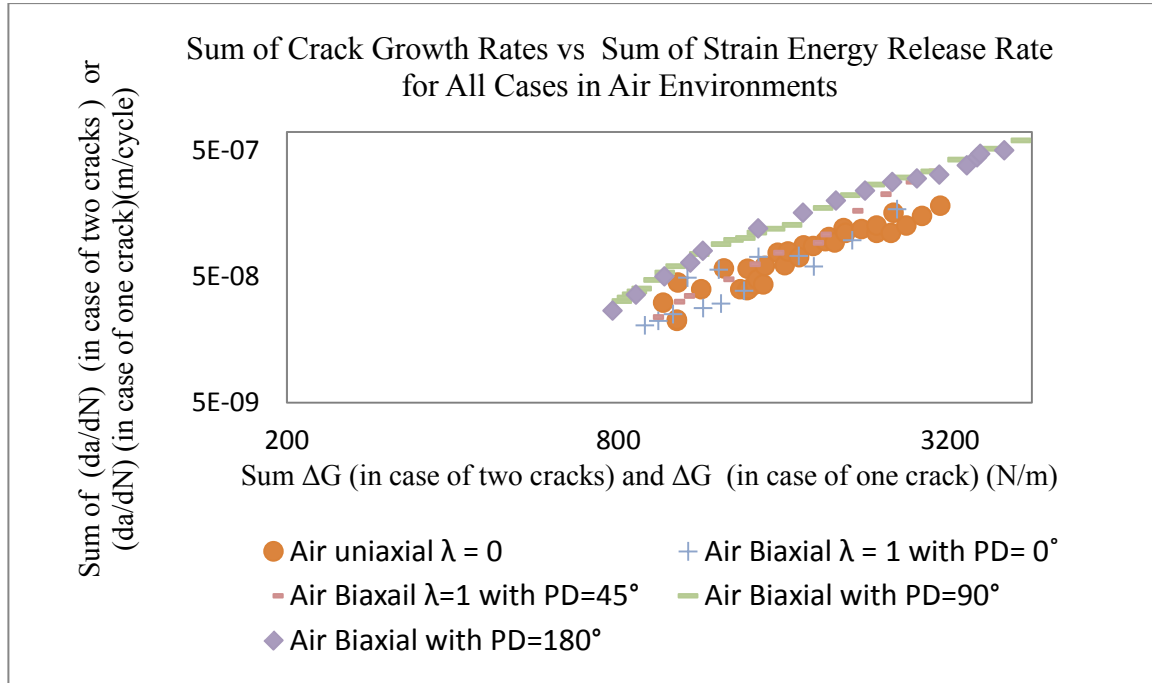


Figure D.1: Sum of crack growth rates versus sum of strain energy release rate for all cases in air environment.

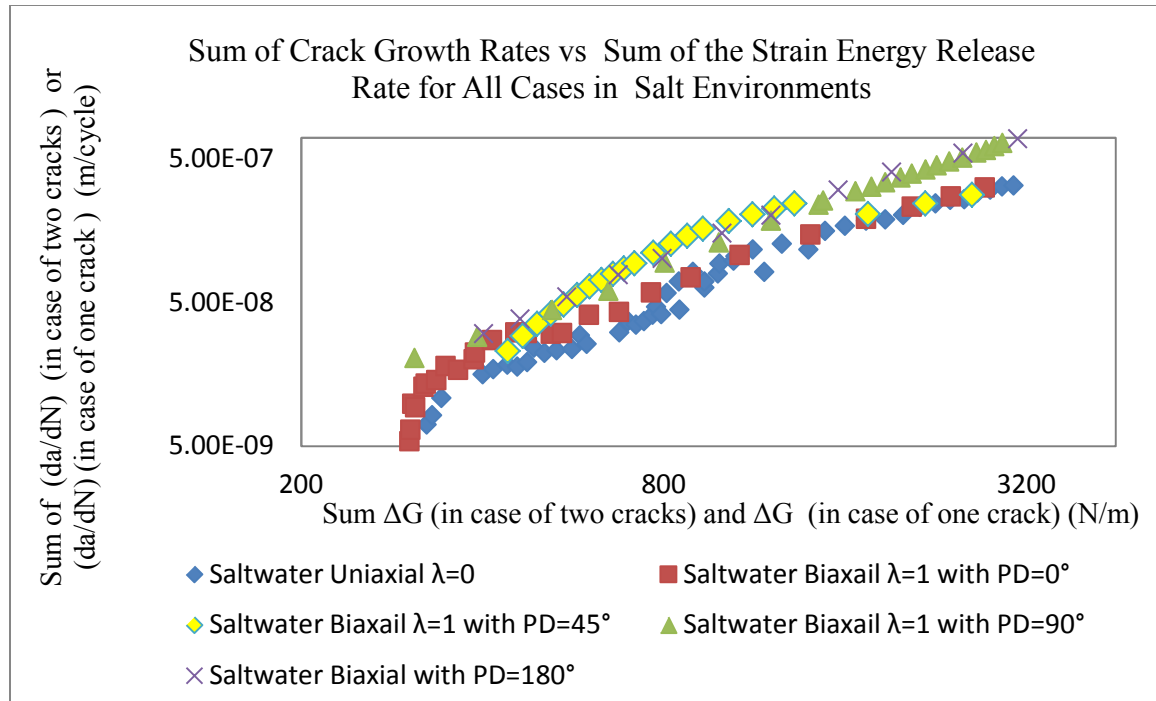


Figure D.2: Sum of crack growth rates versus sum of strain energy release rate for all cases in salt environment.

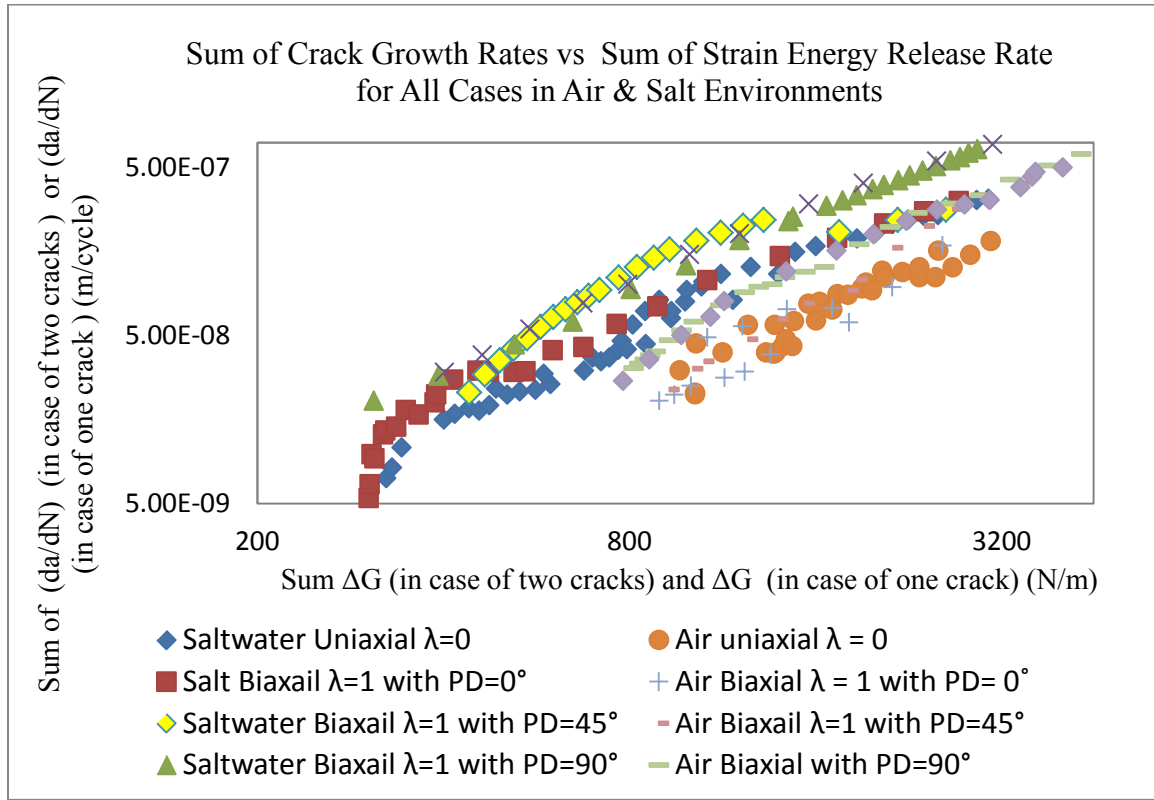


Figure D.3: Sum of crack growth rates versus sum of strain energy release rate for all cases in air and salt environments.

Bibliography

- [1] 7000 Series Aluminum Alloy, Aerospace Specification Metals (ASM),
<http://asm.matweb.com/search/SpecificMaterial.asp?bassnum=MA7075T6>.
(Accessed November 2014).
- [2] AHLUWALIA, HIRA. “Combating Plate Corrosion.” THE FABRICATOR,
2003.
- [3] Alcoa 7075 data sheet (PDF). (Accessed August 2nd, 2014).
- [4] Anderson, P.R.G., and G.G. Garrett. “Fatigue Crack Growth Rate Variations in
Biaxial Stress Fields.” International Journal of Fracture, 16:R111–116, 1980.
- [5] Anderson, T.L., Fracture Mechanics: Fundamentals and Applications, 3rd
edition, Taylor and Francis, 2005.
- [6] Berezhnitski, L.T., and R.S. Gromyak. “Evaluation of Limiting State of Matrix
in Vicinity of Sharp-Edge Rigid Inclusion.” Material Science, Volume 13,
Number 2, 1977.
- [7] Borisenko, Tarapov, Vector and Tensor Analysis with Applications, 1968.
- [8] Castro P.M.S.T., P.F.P. Matos, G.P. Moreira, and L.F.M. Silva. “An Overview
on Fatigue Analysis of Aeronautical Structural Details: Open Hole, Single Rivet
Lap-Joint, and Lap-Joint Panel.” Materials Science and Engineering: A, 468-
470:144–157, 2007.
- [9] Davis, JR. “Corrosion of Aluminum and Aluminum Alloys.” Materials Park,
OH: ASM International, 1999.

- [10] Erdogan, F., and G.C. Sih. "On The Crack Extension in Plates under Plane Loading and Transverse Shear." Transactions of ASME. Journal of Basic Engineering, Volume 85, Number 4, Pages 519-527, 1963.
- [11] FHWA. "Corrosion Costs and Preventive Strategies in the United States." 2002.
- [12] Gangloff, Richard P. "Environmental Cracking: Corrosion Fatigue." Corrosion Tests and Standards Manual ASM International, 1–20, 2004.
- [13] Genkin, Jean-Marc P. "Corrosion Fatigue Performance of Alloy 6013-T6." Massachusetts Institute of Technology, 1992.
- [14] Gerhardus, H. Koch. "Aircraft, 2.2 Billion per Year." 2006.
- [15] Hawkins, Kari, Redstone, USAG, "Army Attacks Hardware Corrosion." The Official Homepage of United States Army, 2012.
- [16] Hays, R., and G. Keller. "New Technologies and Future Challenges for the Prevention of Corrosion in US DOD Assets." U.S. Department Of Defense Corrosion Policy and Oversight Office.
- [17] Hopper, C.D., and K.J. Miller. "Fatigue Crack Propagation in Biaxial Stress Fields." The Journal of Strain Analysis for Engineering Design, 12:23–28, 1977.
- [18] Joshi S., J. Shewchuk. "Fatigue-Crack Propagation in a Biaxial-Stress Field." Exp. Mech., 1970.
- [19] Kaminski A.A., and N.S. Sailov. "Spreading Of Cracks from the Contours of Elliptical Openings in Brittle Plates under Biaxial Tensile Stresses." Soviet Applied Mechanics, volume 11, Number 2, pages 167-173, 1975.

- [20] Kopeliovich, Dmitri. “Corrosion Fatigue.” Knowledge Source on Material Engineering.
- [21] Lados, D.A., and P.C. Paris. “Parameters and Key Trends Affecting Fatigue Crack Growth: a Tribute to Professor Arthur J. Mcevily’s Contributions.” Materials Science and Engineering: A, 468-470:70-73, 2007.
- [22] Lee E.U., and R.E. Taylor. “Fatigue Behavior of Aluminum Alloys under Biaxial Loading.” Engineering Fracture Mechanics, 78:1555–1564, 2011.
- [23] Liu A.F., and D.F. Dittmer. “Effect of Multiaxial Loading on Crack Growth.” Volume 2: compilation of experimental data, Northrop Corp Hawthorne, 1978.
- [24] McEvily, A.J., and W. Illg. “The Rate of Fatigue Crack Propagation in Two Aluminum Alloys.” NASA TN 4394, 1958.
- [25] Megson, T.H.G., Aircraft Structures for Engineering Students, 5th edition, P: 371-372, 2012.
- [26] Misak H.E., V.Y. Perel, V. Sabelkin, and S. Mall. “Biaxial Tension-Tension Fatigue Crack Growth Behavior of 2024-T3 under Ambient Air and Saltwater Environments.” Air Force Institute of Technology, 2014.
- [27] Misak H.E., V.Y. Perel, V. Sabelkin, and S. Mall. “Corrosion Fatigue Crack Growth Behavior of 7075-T6 under Biaxial Tension–Tension Cyclic Loading Condition.” Air Force Institute of Technology, 2013.
- [28] Misak H.E., V.Y. Perel, V. Sabelkin, and S. Mall. “Crack Growth Behavior of 7075-T6 under Biaxial Tension–Tension Fatigue.” Int. J Fatigue, 2013.

- [29] Park, J. K., and A.J. Ardell. "Microstructures of the Commercial 7075 Al Alloy in the T651 and T7 Tempers." *Metall. Trans. A*. 14A (1983): 1957. Print.
- [30] Parrington, Ronald J. "Fractography of Metals and Plastics." *Practical Failure Analysis*, 2002.
- [31] Pennisi, Mario S. "Corrosion: Why Apply a Coating." *Coating Fabrication*, 1999.
- [32] Pocajt, Viktor. "Total Material, Fatigue Properties: Part One." November 2010.
- [33] Ravichandran, K. S., Y. Murakami, and R.O. Ritchie. "Small Fatigue Cracks: Mechanics, Mechanisms and Applications." ISBN: 0-08-043011-2, 1999.
- [34] Rob, Glossary. "Fatigue (Failure Mechanism)." December 2010.
- [35] Roberge, P.R. "Corrosion Engineering: Principles and Practice." McGraw-Hill, 2008.
- [36] Roylance, David. "Introduction to Fracture Mechanics." Department Of Materials Science and Engineering, Massachusetts Institute of Technology, Cambridge, 2001.
- [37] Scheel, E. Jeremy, III. Prev  y, S. Paul, and Douglas J. Hornbach. "The Effect of Surface Enhancement on the Corrosion Properties, Fatigue Strength, and Degradation Of Aircraft Aluminum." *Lambda Research*, 2010.
- [38] Shanyavskiy, A. "Fatigue Cracking Simulation Based on Crack Closure Effects in Al-Based Sheet Materials Subjected to Biaxial Cyclic Loads." *Engineering Fracture Mechanics*, 78:1516- 1528, 2011.

- [39] Sih, G.C., “A Special Theory of Crack Propagation.” *Mechanics of Fracture*, Volume 1, pages 21-45, 1973.
- [40] Sih, G.C., and B.C. Cha. “A Fracture Criterion for Three Dimensional Crack Problems.” *Engineering Fracture Mechanics*, Volume 6, pages 699-723, 1974.
- [41] Sunder, R. “Development Of The Marker-TWIST Load Sequence for Quantitative Fractographic Studies.” *International Journal of Fatigue*, 2010.
- [42] Sunder, R., and B.V. Ilchenko “Fatigue Crack Growth under Flight Spectrum Loading with Superposed Biaxial Loading Due to Fuselage Cabin Pressure.” *International Journal of Fatigue*, 33:1101–1110, 2011.
- [43] Tian, De-Chang, Lu Dau-Quan, and Zhu Jia-Ju. “Crack Propagation under Combined Stresses in Three Dimensional Medium.” *Eng.Fract.Mech*, Volume 16, Number 1, pages 5-17, 1982.
- [44] Tiroshu, J. “Incipient Fracture Angle, Fracture Loci and Critical Stress for Mixed Mode Loading.” *Eng.Fract.Mech*, Volume 2, Number 3, pages 607-616, 1977.
- [45] Uhlig, H.H., and R. Winston Revie. “Corrosion and Corrosion Control.” 4th edition, John Wiley and Sons Inc., 2008.
- [46] Wollmann, M. “Structural Integrity: Stress Corrosion Cracking, Corrosion Fatigue.” *Universidad Polytechnica de Madrid, Clausthal University of Technology*, May 2012.

- [47] Yuuki, R., K. Akita, and N. Kishi. "The Effect of Biaxial Stress and Changes of State on Fatigue Crack Growth Behavior." *Fatigue and Fracture of Engineering Materials and Structures*, 12:93-103, 1989.

REPORT DOCUMENTATION PAGE			Form Approved OMB No. 0704-0188		
<p>The public reporting burden for this collection of information is estimated to average 1 hour per response, including the time for reviewing instructions, searching existing data sources, gathering and maintaining the data needed, and completing and reviewing the collection of information. Send comments regarding this burden estimate or any other aspect of this collection of information, including suggestions for reducing this burden to Department of Defense, Washington Headquarters Services, Directorate for Information Operations and Reports (0704-0188), 1215 Jefferson Davis Highway, Suite 1204, Arlington, VA 22202-4302. Respondents should be aware that notwithstanding any other provision of law, no person shall be subject to any penalty for failing to comply with a collection of information if it does not display a currently valid OMB control number. PLEASE DO NOT RETURN YOUR FORM TO THE ABOVE ADDRESS.</p>					
1. REPORT DATE (DD-MM-YYYY) 18/08/2015		2. REPORT TYPE Master's Thesis		3. DATES COVERED (From — To) August 2013 – September 2015	
4. TITLE AND SUBTITLE Corrosion Fatigue Crack Growth Behavior At Notched Hole In 7075-T6 Under Biaxial And Uniaxial Fatigue With Different Phases		5a. CONTRACT NUMBER			
		5b. GRANT NUMBER			
		5c. PROGRAM ELEMENT NUMBER			
6. AUTHOR(S) Khawagi, Ali, Captain, Royal Saudi Air Force		5d. PROJECT NUMBER			
		5e. TASK NUMBER			
		5f. WORK UNIT NUMBER			
7. PERFORMING ORGANIZATION NAME(S) AND ADDRESS(ES) Air Force Institute of Technology Graduate School of Engineering and Management (AFIT/EN) 2950 Hobson Way WPAFB OH 45433-7765		8. PERFORMING ORGANIZATION REPORT NUMBER AFIT-ENY-MS-15-S-065			
9. SPONSORING / MONITORING AGENCY NAME(S) AND ADDRESS(ES) Rich Hays Technical Corrosion Collaboration Office of Secretary of Defense Washington D.C.		10. SPONSOR/MONITOR'S ACRONYM(S) TCC OSD			
		11. SPONSOR/MONITOR'S REPORT NUMBER(S)			
12. DISTRIBUTION / AVAILABILITY STATEMENT Approved For Public Release; Distribution Unlimited.					
13. SUPPLEMENTARY NOTES This work is declared a work of the U.S. Government and is not subject to copyright protection in the United States.					
14. ABSTRACT This research investigates fatigue crack propagation behavior in both air and saltwater (3.5% NaCl) environments from pre-cracked notched circular hole in a 7075-T6 cruciform specimen. With stress ratio of 0.5, biaxiality stress ratio of unity, and frequency of applied load of 10 Hz, the crack growth behavior was investigated under in-plane biaxial tension-tension fatigue with 45°, 90° and 180° phase difference conditions and then compared to previous fatigue tests with no phase difference to study the effect of changing the phase differences between the applied loads on the crack growth rate. Finite Element Analysis (FEA) was used to calculate cyclic variation of stress intensity factors (ΔK) at the crack tips. The crack growth rate was observed using optical microscopy. This study shows that in the biaxial fatigue tests with phase difference of 45°, 90° and 180°, two fatigue cracks were shaped, symmetrical in case of 90° and 180°, while it's unsymmetrical for 45° phase difference case. For each phase difference and at a given average crack growth rate, the strain energy release rate of the non-split crack is equivalent to the sum of strain energy release rates of the two split cracks. In the saltwater environment, the corrosion accelerates the crack growth rate.					
15. SUBJECT TERMS Corrosion, Fatigue, Fracture Mechanics, Crack Initiation, Crack Growth Rate, Aluminum Alloy					
16. SECURITY CLASSIFICATION OF:			17. LIMITATION OF ABSTRACT UU	18. NUMBER OF PAGES 148	19a. NAME OF RESPONSIBLE PERSON Shankar, Mall, Ph. D. (ENY)
a. REPORT U	b. ABSTRACT U	c. THIS PAGE U			19b. TELEPHONE NUMBER (Include Area Code) (937) (937) 255-6565, ext 4587; Shankar.Mall@afit.edu